Universidad
Carlos III de Madrid
www.uc3m.es

Doctoral Thesis

Synthesis, Processing and Mechanical Characterization of Ti(C,N)-based cermets through the combination of Colloidal and Powder Metallurgy techniques

Author:
Miguel de Dios Pérez

Supervisors:
Dra. Elena Gordo Odériz
Dra. Begoña Ferrari Fernández

Tutor:
Dra. Elena Gordo Odériz

Materials Sciences and Engineering Department at Universidad Carlos III

Leganés, Diciembre 2017

Universidad
Carlos III de Madrid
www.uc3m.es

Doctoral Thesis

Synthesis, Processing and Mechanical Characterization of Ti(C,N)-based cermets through the combination of Colloidal and Powder Metallurgy techniques

Autor: Miguel de Dios Pérez

Director/es: Dra. Elena Gordo Odériz
Dra. Begoña Ferrari Fernández

Firma del Tribunal Calificador:

		Firma
Presidente:	Dr. Antonio Javier Sánchez Herencia	
Vocal:	Dra. Raquel de Oro Calderón	
Secretario:	Dra. Sophia Alexandra Tsipas	

Calificación:

Leganés, 20 de Diciembre de 2017

Esta Tesis Doctoral ha sido realizada entre la Universidad Carlos III de Madrid y el Instituto de Cerámica y Vidrio, siendo financiada por el proyecto MAT-2012-38650-C02-01 “Diseño de la microestructura y la microarquitectura de materiales metal-cerámicos utilizando tecnologías coloidales y pulvimetalurgicas” (MITICO) y por una Beca FPI-2013 (BES-2013-065760) del Ministerio de Economía y Competitividad.

Esta memoria de tesis cumple los requisitos necesarios para obtener la Mención Internacional en el Título de Doctor que se describen en la normativa de enseñanzas universitarias de doctorado de la Universidad Carlos III de Madrid y que han sido establecidos en el artículo 15 del Real Decreto 99/2011 que establece la Ordenación de las Enseñanzas Universitarias Oficiales (BOE nº 35 del 28 de Enero de 2011, Págs. 13909-13926. Dicha Memoria de tesis ha sido informada por dos doctores que pertenecen a instituciones de educación superior de Estados miembros de la Unión Europea distintos de España:

Dr. Jesús González Julián
Institute of Energy and Climate
Reseachm Forschngszentrum Jülich GmbH
Germany

Dra. Raquel de Oro Calderón
Dr Materials Science and Engineering
Marie Skłodowska-Curie Intra-European Fellow
Institute of Chemical Technologies and Analytics
TU Wien, Vienna

A mis padres

A los que se marcharon y nunca debieron irse

Acknowledgments

Contents

Chapter 1

Introduction

1. Introduction

1.1 Machining

In recent few decades, although there have been some momentous advances in new forming techniques, machining is still a predominant industrial activity. In a machining system, cutting tools play a significant role for high cutting speed, namely for high productivity. With respect to a cutting tool, it has to withstand abrasion, chemical reaction, plastic deformation, and thermal shock during its application [1].

A basic knowledge of each cutting tool material and its performance is therefore important so that the correct selection for each application can be made. Considerations include the workpiece material (composition) to be machined, the component type and shape, machining conditions and the level of surface quality required for each operation. As it can be seen in Figure 1, cutting tool materials have different combinations of hardness, toughness and wear resistance, and are divided into numerous grades with specific properties. Generally, a cutting tool material that is successful in its application should be:

- Hard, to resist flank wear and deformation
- Tough, to resist bulk breakage
- Non-reactive with the workpiece material
- Chemically stable, to resist oxidation, corrosion and diffusion
- Resistant to sudden thermal changes

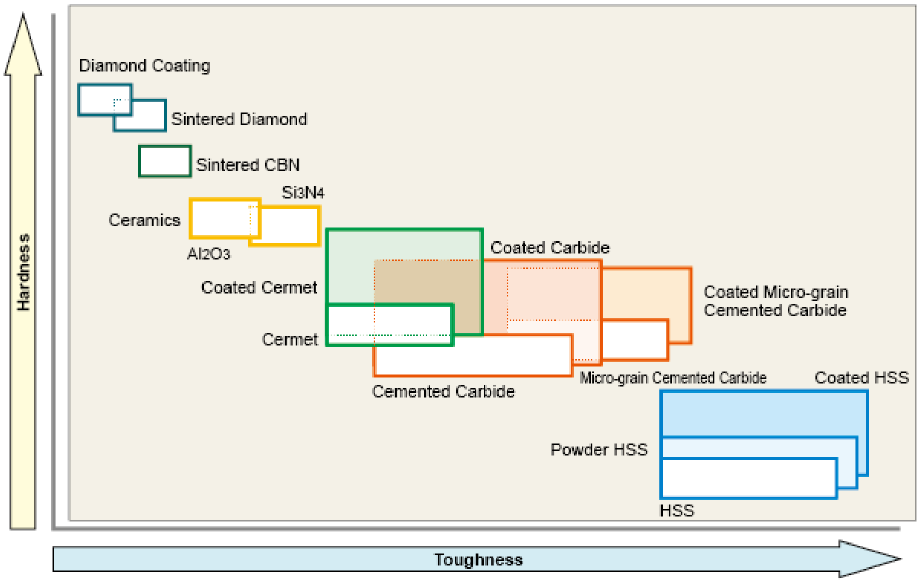

Figure 1. Hardness vs Toughness of cutting tool materials [2]

According to the material used the tools are classified into:

i. Tool steels

ii. Ceramic Materials

iii. Superhard Materials

iv. Hardmetals and Cemented Carbides

v. Cermets

1.1.1 Tool Steels

Tool steels are either carbon, alloy or high-speed steels, capable of being hardened and tempered. They may be used in certain hand tools or in mechanical fixtures for cutting, shaping, forming and blanking of materials at either ordinary or elevated temperatures. Tool steels are also used on a wide variety of other applications where resistance to wear, strength, toughness and other properties are selected for optimum performance.

According to the AISI classification, tool steels are classified into different groups depending on the alloying elements present, applications for which they are intended or depending on the indicated thermal treatment. Table 1 shows the main groups of tool steels in the AISI classification.

Table 1. AISI-SAE tool steel grades

Defining property	AISI-SAE grade	Significant characteristics
Water-Hardening	W	-
Shock Resisting	S	-
Cold-Working	O	Oil-hardening
	A	Air-hardening: medium alloy
	D	High carbon and chromium
Plastic Mold	P	-
Hot working	H	H1-H9: chromium base H20-H39: tungsten base H40-H59: molybdenum base
High Speed	T	Tungsten base
	M	Molybdenum base

Within all tool steels, **High Speed Steel (HSS)** must be highlighted. This tool steels are complex iron-based alloys of carbon, chromium, vanadium, molybdenum, or tungsten, or combinations thereof, and in some cases substantial amounts of cobalt. This highly alloyed steels are mainly used for cutting tools, since they are characterized by their capacity to retain a high level of hardness while cutting even at elevated temperatures. High speed steel has unusually high resistance to softening at temperatures up to 600˚C, called red hardness.

Historically, the first high speed steel were the tungsten base type developed by Robert Mushet in the UK and F.W. Taylor in USA toward the end of the XIX century. In 1904 the addition of vanadium was patented by the Crucible steel company, leading finally to today’s best known grade, 18/4/1 (18 wt. % W, 4 wt. % Cr and 1 wt. %V). The first record of the use of cobalt in high speed steels was in Germany in 1912. Later, around 1930, molybdenum-bearing alloys were being introduced in USA.

The AISI established a classification system for the high-speed tool steels many years ago. That system consists of a T (T-grades) for those steel that have tungsten as one of their primary alloying elements and an M (M-grades) or those steels that have molybdenum additions as one of their primary alloying elements. In addition, there is a number that follows either the M or the T which does not have any special significance other than to distinguish one from other.

Table 2. Common chemical composition of high speed steels. All percentages are in weigth (wt. %)

Type	C	W	Mo	Cr	V	Co
T-1	0.70	18	---	4	1	---
T-4	0.75	18	---	4	1	5
T-6	0.80	20	---	4	2	12
M-2	0.80	6	5	4	2	---
M-4	1.30	6	5	4	4	---
M-15	1.55	6	3	5	5	5
M-42	1.08	1.5	9.5	4	1.1	8

1.1.2 Ceramic Materials

All ceramic cutting tools have excellent wear resistance at high cutting speeds. Traditionally, the materials most widely used as cutting tool have been limited to Al_2O_3, Si_3N_4, oxide ceramics, and composites of these materials.

Experiments with **Alumina** and **Alumina-Based Composites** started already before the Second World War. Throw-away tool tips consisting basically of Al_2O_3 have been available commercially for more than 30 years, and have been used in many countries for machining steel and cast iron. Additions of different secondary agents such as TiC, (Ti,Ta)C, ZrO_2 or SiC_w (whiskers) have been used for improve some specific mechanical property in the material [3–6]. For example, Silicon Carbide whiskers (SiC_w) has been used to dramatically increase toughness and enable the use of coolant [7].

Silicon-based structural ceramics (SiC, Si_3N_4, SiAlON) exhibit attractive properties, for example high strength, stiffness, and good wear and corrosion resistance, and are considered as very appropiate materials for high temperatura applications. Silicon carbide and nitride can be obtained with different morphologies: single crystals, whiskers, powders, films, etc, the choice depends on the final application. **Silicon carbide** (SiC) ceramics have a set of unique physical-chemical properties, such as high hardness and mechanical stability at high temperatures, excellent thermal conductivity and low coefficient of thermal expansion, high resistance to corrosion and oxidation, wide bandgap, and others. This low density ceramic has a variety of applications including as an abrasive material, wide bandgap semiconductors in high-power electronics, and structural ceramics in the automotive and aerospace industries. **Silicon nitride ceramics** (Si_3N_4) represent another group of ceramic materials. Si_3N_4 ceramic material was firstly developed in the 1960s in a search for fully dense, high strength and high toughness materials. Their elongated crystals form a self-reinforced material with high toughness. A variation of this materials are the **Sialon (SiAlON).** This ceramic alloy based on the elements silicon (Si), aluminium (Al), oxygen (O) and Nitrogen (N) was developed in the early 1970s to solve the problem of silicon nitride (Si_3N_4) which was difficult to fabricate. As alloys of Si_3N_4, SiAlON exists in three basic forms. Each form is isostructural with one of the two common forms of Si_3N_4 beta (β) and alpha (α) and with silicon oxynitride. There is substitution for Si by Al with corresponding atomic replacement of N by O, to satisfy valancy requeriments. The resulting "solution" has superior properties to the original pure solvent (Si_3N_4). Sometimes, Yttria (Y_2O_3) is added in order to increase the efficiency of the sintering process [8,9]. These material combine the strength of a self-reinforced silicon nitride network with enhanced chemical stability.

While the above-described materials are still employed, in recent years, ceramics based on the **transition metal nitrides, carbides or borides** are gaining increasing technical importance due to their extremely high melting points (>2500 ˚C). Among all of them, **diborides** such as ZrB_2, TiB_2 and HfB_2 are materials which have an unique combination of mechanical and physical properties, including high melting points (>3000 ˚C), high thermal and electrical conductivities, chemical inertness against molten metals and great thermal shock resistance [10]. Because of the strong covalent bonding and low self-diffusion, these refractory diborides require high temperatures and external pressures to densify [11]. Two ways typically are used to enhance densification. The first way is that alternative processing routes, such as reactive hot pressing [12], spark plasma sintering [13], and polymer precursors [14] have been investigated to improve the purity and densification behavior of diborides. The second way is that various additives have been studied to reduce sintering temperature [11].

Although carbides have higher melting points (>3500 ˚C), borydes have been postulated as attractive candidates for high temperature thermomechanical structural applications at temperatures higher than 2000 ˚C. ZrB_2 has the lowest theoretical density among the ultra high-temperature ceramics

(UHTCs) being attractive for aerospace applications [11]. TiB_2 has also interesting physical properties due to its strength combined to its low density. This material is widely accepted for applications including microelectronics, diffusion barriers, wear and erosion resistant coating and other mechanical components [15] and HfB_2 has been considered as a valuable candidate material for high-temperature structural parts, refractory linings, cutting tools, electrodes and microelectronics [16,17].

1.1.3 Superhard materials (CBN, PDC)

The highest performing abrasive materials are classified as either superhard or ultra-hard, based on their measured hardness regardless of their chemical nature. Ceramics such as cubic Boron Nitride (cBN), in its various formats, is a truly superhard material which currently compliments diamond in abrasive markets due to its ability to very effectively precision machine ferrous-based materials (unlike diamond).

Cubic boron nitride (cBN), is the second hardest material after synthetic diamond and is synthesised from hexagonal boron nitride under conditions similar to those used to produce synthetic diamond from graphite. CBN is a material with excellent abrasive response including high hardness, strength, abrasion resistance, and thermal and chemical resistance, and an ability to maintain sharp cutting edges during use. These characteristics exceed the values of conventional abrasives, such as silicon carbide and aluminum oxide. In particular, the properties of high thermal stability and chemical resistance make it suitable for machining ferrous materials, an area where synthetic diamond abrasives are not normally employed.

Polycrystalline diamond (PCD) is a composite of diamond particles sintered together with a metallic binder. Diamond is the hardest, and therefore the most abrasion resistant, of all materials. This material has been used in a variety of industries such as oil & gas, aerospace, car manufacturing, mining and many other custom engineering applications. Due to its extreme hardness, wear resistance and thermal conductivity it is an ideal choice for extreme conditions and applications.

Every tool material must combine sufficient toughness with wear resistance (hardness). However, features with increased toughness will invariably have lower wear resistance. Up to the date, although numerous practical machining operations and several progresses have been made in various cutting tool materials, hardmetals and cermets are key tool materials in the market due to their excellent balance of hardness and toughness combining the most remarkable mechanical properties that characterize the ceramic and metallic materials respectively. Therefore, those materials will be discussed in more detail later.

1.2 Introduction to Hardmetals and cemented carbides

The term cemented carbide is widely used in the United States of America, although these materials are better known as hard metals in Europe. The invention of hardmetals dates back to the beginning of the twentieth century and is attributed to Karl Schröter who disclosed his invention in 1923 in a patent application [18]. Today this materials form the backbone of the tool manufacturing industry (Figure 2) with such diverse applications as metal cutting, mining, chipless forming, wear applications, etc. There has been a continuous expansion in the consumption of cemented carbide from an annual world total of 10 ton in 1930; to 100 ton around 1935; 1000 ton in the early 1940s; 10000 ton; in 1960s and up to nearly. In the first decade of the 21st century, the global use of hardmetals, peaked at 58 000 tons. It dropped substantially in 2009, as the recession took hold, but recovered most of the losses in 2010 as users restocked.

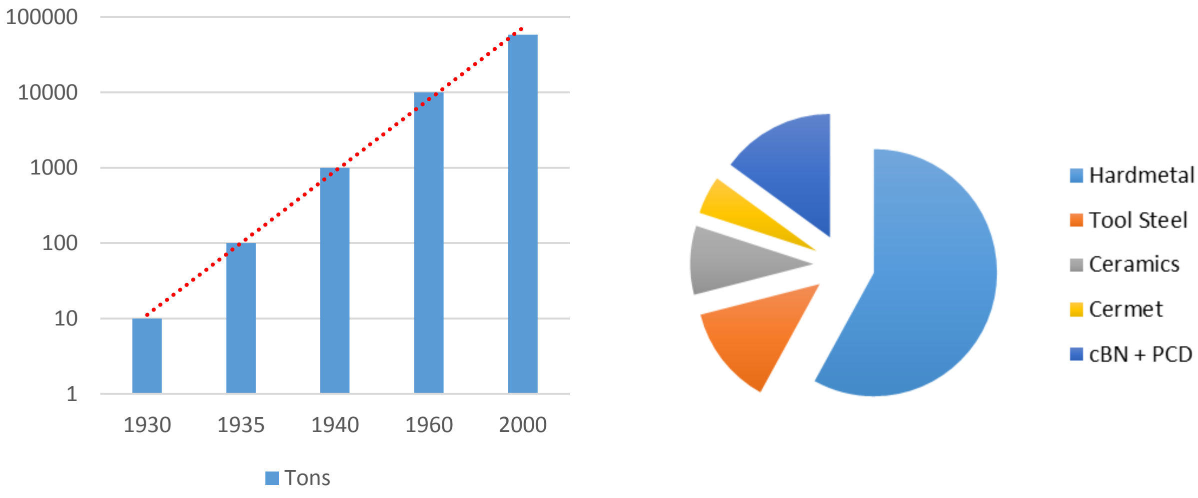

Figure 2. (a) Estimated worldwide production of hardmetals and (b) Global metal cutting market [19].

Although 90 years have passed since its invention, cemented carbide is still used today. This composite material consists of at least one hard and wear resistant phase; being mainly tungsten carbide (WC) embedded into a ductile and softer metallic binder phase from the iron group of metals (mainly cobalt, Co). More than 90% of all hardmetals utilize Co as the preferred binder metal with contents between 3% and 30% by weight. Although WC is not the hardest carbide, nor Co is the toughest metal, the combination of both brings to the composite a high hardness value that is maintained at high temperature, high wear resistance and high toughness. The reasons for the dominant role of Co are some unique properties of Co and the Co-W-C ternary system. It is well known that the solubility of WC in Co is not only high but also strongly varies depending upon the temperature. The metallic phase is an alloy Co-W-C where the W and C are dissolved in a solid solution Co. This is closely connected to the excellent wetting between WC and molten Co during liquid phase sintering (LPS), as well as to favourable properties such as high hardness, yield stress, toughness and strength [20].

However, there are also detrimental properties of this binder metal. Cobalt can exist essentially in two allotropic forms: Co (ε) (close packed hexagonal, CPH), stable at temperatures below 400°C, and Co (α) (face centered cubic, FCC), stable at higher temperatures. This allotropic transformation is not completely reversible because the FCC structure is stabilized by the dissolution of W and C in the Co, so that after sintering a mixture of Co (ε) HCP and Co (α) FCC is obtained. When the Co with FCC structure is subjected to deformation, it is transformed into Co with HCP structure. This fact is undesirable because the latter crystalline structure is more fragile and causes a decrease in the mechanical properties of the material as in fracture toughness [21]. Besides other important drawbacks of this cemented carbides are their low resistance to corrosion and oxidation as well as the fluctuating prices of Co. Last but not least, another important aspect related to health, aims at the replacement of the traditional Co binder.

1.2.1 Mechanical properties of WC-Co

Hardmetals are the material of choice in all application where wear resistance combined with toughness and strength is required at ambient and elevated temperatures. Figure 3 shows the wide range of properties of cemented carbides in use today.

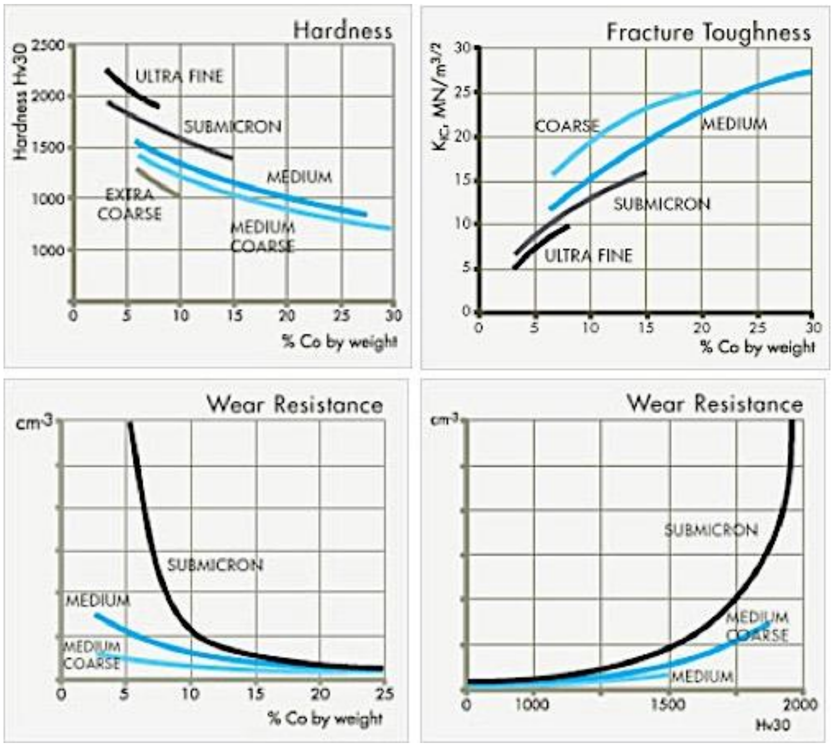

Figure 3. Hardness, fracture toughness and wear resistance of WC-Co hardmetals as function of WC grain size and binder content (Sandvik Hardmaterials)

The excellent and unique properties of the cemented carbides can be varied in a wide range by the proper choice of the grain size of the carbide (submicrometer to tens of micrometers) and the amount of binder phase (2-30 wt. %). However, although most of the attention was focused on the grain size and binder content, there are other important factors such as grain size distribution, degree of WC recrystallization during liquid phase sintering and the binder distribution especially at grain boundaries [22]. Additions of early transition metal refractory carbides (mainly groups IV-VI, as summarized in Table 3) are added with two main purposes: To act as grain growth inhibitors (GGIs) to hide the growth of the WC grain, improving the microstructure homogeneity and mechanical properties of WC-Co cemented carbides, and in order to achieve certain desired final properties. Generally, the order of overall inhibition effectiveness is VC > Cr_3C_2 > NbC > TaC > TiC. However, VC results in the embrittlement of WC-Co, Cr_3C_2 is not suitable for using in high temperature conditions, TiC has the worst inhibition effectiveness. It seems that NbC and TaC are the best grain inhibitors for coarse-grained WC-Co due to their high melting temperature and low thermal expansion [23]. In comparison to TaC, NbC is more hostile in the densification of WC-Co.

Table 3. Major compositions and structures of interstitial carbides

Group IV	Group V	Group VI
TiC	V_2C, V_3C_4, V_6C_5, V_8C_7, VC	$Cr_{23}C_6$, Cr_7C_3, Cr_3C_2
ZrC	Nb_2C, Nb_3C_2, Nb_4C, NbC	Mo_2C, Mo_3C_2, MoC
HfC	Ta_2C, Ta_3C_2, Ta_4C_3, TaC	W_2C, WC

These GGIs (summarised in Table 3) have several important characteristics in common, such as:

- Their interstitial structures lead to a combination of metallic, covalent, and ionic bonds.
- They are primarily non-stoichiometric phases, and ordering of the carbon atoms is common.
- They combine the physical properties of ceramics and the electronic properties of metals, i.e. high hardness and strength with high thermal and electrical conductivities.
- They have the highest melting points of any group of materials.
- They have high thermal and chemical stability.

During the last years, with the intention to improve the mechanical properties of cemented carbides, many investigations have been carried out analyzing the influence of the main parameters mentioned above.

The effect of the ceramic particle size was studied by **Chang** et al. [24] to evaluate it is influence on the sintered behavior and final mechanical properties. It is reasonable to suggest that the smaller size of WC powders is able to produce a large surface area, which leads to a better wetting and LPS behavior resulting in dense materials with better mechanical response. With the reduction of the ceramic particle size, the hardness was enhanced from 1300 to 1500 HV and the transverse rupture strength, called TRS, was increased from 1450 to 1550 MPa. Besides, the K_{IC} value for nano-WC dramatically increased up to 12.7 MPa·m$^{1/2}$. The smaller the particle size, the more grain boundaries there will be. That means, there will be more obstacles to hind the slipping by dislocation.

The effect of the composition and content of the binder phase was studied by numerous researchers. **Chang** et al. [25] studied two different tungsten carbide binders (Co and Ni-Fe). Compared with Co, Ni-Fe binder has lower melting point (1444°C compared to 1495°C of the Co). Thus, for the same sintering cycle, the WC-Ni-Fe hardmetal reached higher densities and hence better mechanical properties, increasing their hardness from 850 to 900 HV, the TRS from 2475 to 2525 MPa and reaching K_{IC} values of 15.1 MPa·m$^{1/2}$. **Su** et al. [26] fabricated different WC-6(Co-Ni) cemented carbides. Although the addition of Ni is supposed to facilitate the solution-precipitation of WC particles and promote the growth of WC grains, there is a threshold in which the growth of WC grains can be inhibited. This value is established in a 20 wt. % of Ni/(Ni+Co). For this value, the average WC grain size decreases from 1.67 to 1.48 μ, while the hardness and strength increases from 1450 HV and 2200 MPa to 1475 HV and 2275 MPa, respectively. Coarse grained WC-10((1-x)Co-xNi) cemented carbides with different Ni contents were fabricated by **Zhang** et al. [27]. The results showed that the hardness and transverse rupture strength of WC-8Co-2Ni was 1100 HV and 2800 MPa, respectively. And finally, **Tarragó** et al. [28] studied the influence of binder chemical nature and content (pure Co and 76Co-24Ni), as well as carbide grain size on hardness, flexural strength and fracture toughness. Experimental results showed that hardness decreases and fracture toughness increases as the binder chemical nature is shifted from cobalt to cobalt/nickel. The main reason behind this finding is the higher stacking fault energy of Ni that results in lower hardening rates, thus CoNi binder alloys exhibit lower strength but higher ductility than cobalt [29]. On the other hand, flexural strength did not show any relevant influence on binder chemical nature.

On the other hand, the addition of different secondary carbides was studied. Addition of TaC was researched by **Mahmoodan** et al. [30] who demonstrated that nano grained WC-10Co with a 0.6 wt. % TaC addition improves the hardness and fracture toughness from 1500 HV30 and 11.8 MPa·m$^{1/2}$ (for TaC free sample) to 1600 HV30 and 13.7 MPa·m$^{1/2}$, respectively as well as **Su** et al. [23] found that the best comprehensive mechanical properties was obtained in coarsed grained (6 μm) WC-9Co with a 0.4 wt. % TaC addition reaching HV 1125, TRS of 2500 MPa and fracture toughness of 19.3 MPa·m$^{1/2}$.

Lin et al. [31] doped with 1 wt. % of AlN tungsten carbide hard metals. The existence of this carbide refined the tungsten carbide grains as well as reinforced the obtained hardmetals. Cermets with 1.0 wt. % addition exhibited higher hardness 1750 HV and transverse rupture 3125 MPa, compared with 1600 HV and 2500 MPa of the pure WC-10Co hard metal. **Qiu** et al. [32] found the effects of (Ti, Ta, Nb, W)(C,N) on the microstructure, mechanical properties of WC-Co cemented carbides. It was found that with the addition of (Ti, Ta, Nb, W)(C,N) powders, transverse rupture strength and fracture toughness decreased monotonously. However, the hardness rose sharply at first, reaching a peak at 15 wt. %, then slightly decreased, and finally increased again.

Finally, the effect of the Cr_3C_2 addition was studied by **Fabijanic** et al [33] who researched the effect of the addition of Cr_3C_2 in WC-Co hardmetals. This addition reduced the carbide grain growth during sintering, enhancing the microstructural characteristics of the material and thus the mechanical properties and **Siwak** et al. [34] found the best combination of mechanical properties, hardness of 2100 HV and fracture toughness of 8.3 MPa·m$^{1/2}$ in a hard metal with composition WC-5Co-2Cr_3C_2.

Table 4 highlights some of properties of selected tungsten carbide based hard metals developed in recent years.

Table 4. Review of mechanical properties of different WC-Co

Effect	Composition (wt. %)	WC size (µm)	Hardness (HV)	TRS (MPa)	K_{IC} (MPa·m$^{1/2}$)	Ref.	Year
Particle size	WC-13.5Co	1 µm	≈ 1300	≈ 1450	≈ 12.1	[24]	2014
	WC-13.5(CoNiFe)	200 nm	≈ 1500	≈ 1550	≈ 12.7	[24]	2014
Binder	WC-15Co	Micro	≈ 850	≈ 2475	≈ 10.2	[25]	2014
	WC-15(NiFe)	Micro	≈ 900	≈ 2525	≈ 15.1	[25]	2014
	WC-6Co	1.5 µm	≈ 1450	≈ 2200	---	[26]	2015
	WC-4.8Co-1.2Ni	1.5 µm	≈ 1475	≈ 2275	---	[26]	2015
	WC-8Co-2Ni	12.5 µm	≈ 1100	≈ 2800	---	[27]	2016
Secondary carbide	WC-10Co + 0.6 TaC	0.5 µm	≈ 1600	---	≈ 13.7	[30]	2009
	WC-9Co + 0.4 TaC	6 µm	≈ 1125	≈ 2500	≈ 19.3	[23]	2015
	WC-10Co + 1.0 AlN	0.2 µm	≈ 1750	≈ 3125	---	[31]	2017
	WC-9Co + 0.26 VC + 0.45 Cr_3C_2 WC-9Co + 0.27 VC	0.15 µm	≈ 1900	---	≈ 9.4	[33]	2016
	WC-5Co + 2 Cr_3C_2	0.2 µm	≈ 2100	---	≈ 8.3	[34]	2016

1.2.2 Replacement of WC-Co

The history of hardmetals is filled with attempts to substitute Co as the binding metal. Different perspectives condition future developments in the field of hard materials. These investigations are motivated not only by **economic factors** due to the temporarily high and strongly fluctuating prices of Co and W metal powders (Figure 4) but also due to **strategic and energetic drivers**. There are also serious technical reasons why researchers are trying to improve hardmetals properties by using alternative binders that are responsible for develop hardmetals with superior properties. One route has been to replace WC at least partly through the addition of carbides, nitrides or carbonitrides of titanium, tantalum, and molybdenum due to the strategic character of W which is included in the list of critical raw materials (CRMs).

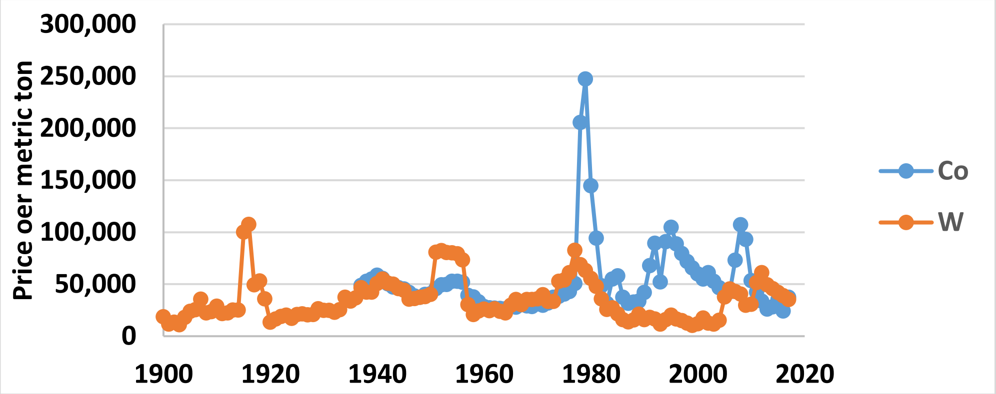

Figure 4. Price per metric ton of Co (blue) and W (Orange)

Besides those demands, concerning economic and technological fields, another very important consideration comes from the **health perspective**, which has increased the research activities to replace or substitute Co totally or partly as binder. The chronic inhalation of hard metal particles can produce an interstitial lung disease. The inhalation effects of both particles (WC-Co) are more severe than those induced by Co metal particles alone, while WC particles could be considered as innocuous [35]. In Europe, **R**egistration, **E**valuation, **A**uthorization and **R**estriction of **C**hemical substances, **REACH**, so far has classified cobalt as very toxic for the human health. Also, the **U.S. N**ational **T**oxicology **P**rogram, **NTP** [36], states that the tungsten carbide-cobalt hard metal dust has been shown to be more toxic in combination than both pure cobalt and tungsten carbide by themselves in vitro studies.

By the reasons pointed out before and the increasing demand of materials with optimized properties, one of the main topics of the actual research in the field of hard metals concerns the development of new composites having comparable or superior properties with partial or total substitution of the traditional cobalt binder by other more economic and less toxic materials. The global hard metal R&D community continues to focus their activities on investigating the microstructure and properties of cemented carbides produced with alternative Fe- and Ni-based binder systems [37]. Previous works by Gille [38] and Schubert [39] shown that cemented carbides with certain Fe-Ni-Co and Fe-Ni binder compositions were of interest to the hard metal industry, in particular for applications where improved fatigue strength and toughness were required. According to these conclusions, in this work we propose to work with a unique composition of binder, which will be 85/15 wt. % Fe/Ni.

1.3 Introduction to cermets

Compared to the conventional WC-based hardmetals, cermets can provide improved surface finishing with excellent chip and tolerance control, offer geometric accuracy in workpieces, increase the feeding speed as well as remain fixed in critical dimensions. What is more, cermets are much competitive in both the price and the performance compared with the hardmetals, especially in high-speed cutting and finishing operations [40].

The name “cermets” was introduced in the years after the Second World War and has been coined from the syllables “cer” from ceramics and “met” from metal. Originally this new expression was supposed to describe materials, which combine the favorable materials properties of ceramics (hardness and wear resistance) with those of metals (toughness especially).

Although in industry application there are two kinds of cermets, namely TiC and Ti(C,N)-based cermets, the latter have gained considerable attention as a potential replacement for WC-Co. These cermets have much higher high-temperature hardness, higher transverse rupture toughness, better resistance to oxidation, and much higher thermal conductivity. Moreover, due to the much finer grains of the hard phase obtained, thanks to the inhibitor grain growth effect of TiN [41], the resistance to high-temperature creep deformation is enhanced compared to TiC-based cermets. Also during machining operations, the formation of oxidation layers, scaling, crescent depression and built-up edges it is more impeded due to the higher enthalpy in formation of Ti(C,N), as compared with TiC-based cermets. According to the comparison established in Table 5, as well as considering all the above-mentioned facts, Ti(C,N)-based cermet cutting tools have become the predominant cutting tool material in industry, replacing TiC-based cermets in many applications.

Table 5. Comparison of high-temperature properties between a TiC-based cermet and a Ti(C,N)-based cermet [42]

Cermet	Microhardness (1000˚C, kgf/mm^2)	TRS (900˚C, MPa)	Weight gain (1000˚C, mg/cm^2·h)	Thermal conductivity (1000˚C W/m·K)
TiC-based	500	1050	11.8	24.7
Ti(C,N)-based	600	1360	1.6	42.3

1.3.1 Microstructure of Ti(C,N)-based cermets

The crystal structure of Ti(C,N) had been issued for debate until recently. According to Levi et al. [43] the previous accepted structural model for Ti(C,N), which had a completely random occupation of all sites by Ti, C, and N was found to be incorrect. Based on phase diagrams of the TiN-TiC system, full solubility of TiC in TiN is expected. Thus, Ti(C,N) formation can be described by a substitutional mechanism, where C atoms replace N atoms, resulting in a Ti-ordered C-N-disordered FCC NaCl type structure in which Ti occupies the 4a (0 0 0) Wyckoff sites, and C and N atoms randomly occupy the 4b (½ ½ ½) sites, as it is described in Figure 5.

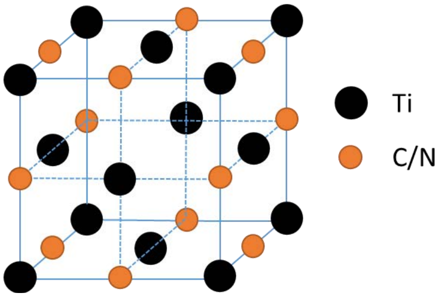

Figure 5. Atomic arrangement of the NaCl type FCC crystals for Ti(C,N)

Thus, the properties of $Ti(C_xN_{1-x})$ vary with x, which means that they are dependent on the properties of both TiC and TiN. Table 6 lists the specific properties of TiC and TiN, from which one can judge approximately the properties of Ti(C,N).

Table 6. The properties of TiC and TiN

	TiC	**TiN**
Molecular weight (g/mol)	59,9	61,9
Unit cell parameter (Å)	4,32	4,24
Density (g/cm3)	4,91	5,39
Bond-dissociation energy (KJ/mol)	423	476
Hardness (Vickers, GPa)	28-35	18-21
Modulus of elasticity (GPa)	414-510	250
Melt point (°C)	3067	2950
Thermal conductivity (W/m·K)	17-24	29
Coefficient of thermal expansion (10^{-6}/°C)	7,4	9,3
Electrical resistivity (μΩ·cm)	68	20
Magnetic susceptibility (emu/mol)	-7.5	38

However the mechanical properties of these composites are largely influenced by different parameters, such as the composition of the binder phase, the addition of secondary carbides, the size of the starting powders as well as the processing route.

1.3.2 History of Ti(C,N)-based cermets

The first generation of cermets appeared in 1931 [44] shortly after the famous Schröter patent covering the WC-Co hardmetals had been filled.

Up to late sixties the nitrides and carbonitrides of the transition metals was considered to be unsuitable and even detrimental ingredients both in conventional hardmetals and TiC-based cermets. Thus they were only of scientific concern until in the late 1960s, Richard Kieffer et al. [45] demonstrated that titanium nitride and titanium carbonitride could be used as proper hard materials for the production of novel hardmetals. However, a prerequisite was necessary to improve the lacking of wettability of their hard phase by the liquid binder metal during sintering. Their work showed that the wettability could be enhanced by the addition of Mo and/or Mo_2C. In Kieffer's research, it was found that mechanical properties at room temperature and high temperature coupled with enhanced resistance to erosion and oxidation could markedly improve adding TiN into TiC-Mo-Ni cermet.

After this systematic work, the research and industrial interest on it started to boom up. However, in spite of the promising properties with respect to the cutting properties of these cermets, they did not find a respective acceptance in Europe and the USA. Conversely, in Japan research and development of cermet grades was started at the beginning of the seventies and has been continued on an increasing scale ever since.

This development may have been triggered by two main factors.

- Interest to develop tungsten-free cutting materials due to the scarcity and cost of raw starting powder. As a consequence of the oil crisis in 1975, particularly tungsten powders increased considerably in cost and their availability was limited, whereas titanium was and is available in almost inexhaustible quantities due to its occurrence as an abundant element of the Earth's crust.

- Development of electronically steered great metal cutting machines and the automation of cutting processes, which have caused a substitution of tougher WC based hardmetals by the more wear-resistant cermets. This also caused an increase in cutting velocity and a decrease in strain by vibration. The development of the clamping technology substituting the soldering technology also furthered the use of cermets.

Since the 1990s to date, the researches and applications of Ti(C,N)-based cermets in Asia and Europe has made great strides and dozens of patents in America and Europe were published. The marked developments of Ti(C,N)-based cermets are listed in Table 7. As it can be seen, most of the efforts have been centered around the modification of the composition of the ceramic phase with the aim of obtaining improved materials.

Table 7. The advance of Ti(C,N)-based cermets [42]

Hard phase	Binder phase	Year
Ti(C,N)	Ni(Co,Fe)	1931
Ti(C,N)	Ni-Mo	1970
(Ti,Mo)(C,N)	Ni-Mo	1974
(Ti,Mo,W)(C,N)	Ni-Mo-Al	1980-1983
(Ti,Ta,Nd,V,Mo,W)(C,N)	(Ni,Co)-Ti_2AlN	1988
(Ti,Ta,Nd,V,W)(C,N)	Ni-Co	1988
(Ti,Ta,Nd,V,Mo,W,etc)(C,N)	Ni-Cr	1991
TiC-TiN-WC	Ni-Mo	1994 -1997
Ti(C,N)-WC-(Ti,W)C	Ni-Co-Mo	1999
TiC-TiN-WC	Ni	2000
Ti(C,N)-WC	Co	2001
Ti(C,N)-Al_2O_3	Ni-Mo	2004
(Ti,W)(C,N)	Ni	2005
Ti(C,N)-WC-TiN	Mo-Ni	2006
Ti(C,N)-WC	Co-Ni	2008
Ti(C,N)	Ni	2009
Ti(C,N)-WC	Ni-Co	2010
(Ti,Mo,W,V)(C,N)	Ni-Co	2011

These tools can be applied to a wide variety of applications. For example, for high-speed finishing and semi-finishing of carbon steels and stainless steels [46]. They can also be utilized in machining and finish milling of alloy steels and cast irons as well as the normal carbon steels [47]. Owing to the excellent high-temperature properties and low density, Ti(C,N)-based cermets have been also applied as refractory parts of jet engines, turbine engines, civil gasoline engines and diesel engines [48,49]. Furthermore, in the field of oil and mining industries, Ti(C,N)-based cermets are used as not only drills and excavating tools, but also oil pipeline nozzles and throttles for their better practicality

[50]. Additionally, on account of their excellent wear resistance, this kind of materials has been successfully used as gauges, hot working models like wire drawing dies, hot rolls and bearings, and even Si_3N_4 ceramics could not throw them into the shade when as bearing materials [48,50,51]. More encouragingly, surgical tools have even been made of Ti(C,N)-based cermets [52]. Other than the above-mentioned facts, Ti(C,N) could even be used as coating materials [53], functionally gradient materials [54], composites [55], and so forth.

1.3.3 Mechanical properties of Ti(C,N)-based cermets

Effect of secondary carbide addition

In most Ti(C,N)-based cermets, the binder phase is mainly composed of Ni [56–61], Co [62,63] or a combination of both [64,65]. However, one of the main trends in the industry of cermets is the substitution of the conventional binders of Ni and Co for metals or alloys with less toxicity and lower cost without losing the characteristic properties of cermets. There are several studies that propose the use of Fe as a metal matrix for cermets [66–69], as it is non-toxic and cheaper than the other routes as well as strengthened by heat treatment [70]. However, despite the considerable amount of research carried out, the application of such cermet systems is limited, mainly due to two major issues: The poor wetting behavior between the metallic phase and the ceramic particles during the liquid phase sintering (LPS) [69] and the low toughness values resulting from the coarsening of the carbides. To overcome such limitations, the addition of alloying elements and compounds such as WC, Mo_2C, TaC, NiB, VC, Ta, C, Cr or Mo has been proposed [71–75], aiming to improve the wetting behavior between both phases during the liquid phase sintering as well as to hinder the ceramic particle growth. **Xiong** et al. [71] described the effect of WC, Mo_2C and TaC additions on the microstructure and mechanical properties of ultrafine Ti(C,N) cermets (0.13 μm). The addition of Mo_2C and WC improve the hardness and the strength, whereas TaC additions have a positive effect on the high temperature properties. However, an excessive addition was found to be detrimental for the mechanical properties of cermets. **Guo** et al. [70] reported the influence of the addition of Mo_2C as secondary carbide to the composition of Ti(C,N)-Fe cermets processed according to conventional powder metallurgy techniques. Although the Mo_2C slightly affects the grain size due to the nature of the Fe binder, these cermets showed enhanced mechanical properties, including hardness (~15 GPa) and transverse rupture strength (TRS) (~1560 MPa). **Naidoo** et al. [60] found that the addition of Ta to Ti(C,N) cermets can result in grain refinement and thus improving hardness (from ~16 GPa to ~18GPa) and fracture toughness (from 5.5 to 6.9 MPa·$m^{1/2}$). **Yang** et al. [61] demonstrated that the transverse rupture strength of Mo-free Ti(C,N)-WC-Cr_3C_2-C-Ni-xCr cermets had a peak value of ~2200 MPa with an addition of 7.6 wt. % of Cr, and that the Vickers hardness was improved from ~9 to ~11 GPa with the Cr content. **Acharya** et al. [76] reported improved mechanical properties of TiC-Ni cermets by the addition of 10 wt. % of NiB, reaching hardness values of ~27 GPa and fracture toughness of ~9 MPa·$m^{1/2}$. They ascribed such improvement to the fine and dense microstructure developed as a consequence of the low melting point of the boride phase (1018 ºC). In a recent work, **Chen** et al. [69] studied the effect of the carbon addition on the microstructure and mechanical properties (hardness and TRS) of Ti(C,N) based cermets. It was found that the addition of extra carbon powders can enhance the rearrangement of Ti(C,N) particles during liquid phase sintering and thus increase their mechanical properties, which is associated with the higher relative densities. A summary of the mechanical properties (i.e. hardness, fracture toughness and bending strength) of the different cermets mentioned above with optimized secondary carbides addition is given in Table 8.

Table 8. Mechanical properties of cermets with different secondary carbides of optimal amount addition

System	Secondary Carbide	Optimal amount [wt. %]	HV [GPa]	KIC [MPa·$m^{1/2}$]	Bending strength* [MPa]	Ref.	Year
Ti(C,N)-Ni	**WC**	25	14.2	8.8	---	[56]	2002
Ti(C,N)-NiCo		15	17.5	---	1500	[71]	2007
Ti(C,N)-Fe	**Mo_2C**	15	14.7	---	1560	[70]	2009
Ti(C,N)-NiCo		10	17.7	---	1300	[71]	2007
Ti(C,N)-Ni	**Ta**	38	17.8	6.9	---	[60]	2014
Ti(C,N)-NiCo	**TaC**	7.0	16.9	---	1580	[71]	2007
Ti(C,N)-Ni	**Cr**	7.6	10.5	---	---	[61]	2015
TiC-Ni	**NiB**	10	27.1	9.0	---	[76]	2016
Ti(C,N)-Fe	**C**	1.0	9.9	---	2480	[69]	2017

* Bending strength may have been measured by different methods; the mean value is reported for comparative purposes.

However, as a result of these additions the microstructures are usually complex showing a typical core-rim structure. Normally, the composition of the core in Ti(C,N)-based cermets, namely the hard phase, is believed to be undissolved Ti(C,N). And the rim is composed by a sort complicated (Ti, W, …)(C,N) solid solutions with a similar crystalline structure than the core, where Ti has been substituted by heavy atoms such as W, Mo, V, Ta, Nb, etc. depending on the secondary carbide added to the cermet [73,77,78].

In general, the rim of Ti(C,N)-based cermets is grown on the basis of the core by an oriented attachment mechanism, which means that the structure of the core-rim interface would not change but the constituents varied due to the heavy solved elements during sintering [79]. This rim frequently consists of two parts, the inner and the outer part [80], mainly due to the higher solubility of TiC in the liquid metal compared to the TiN, which results in the formation of nitrogen-rich Ti(C,N) nuclei around which the dissolved TiC will precipitate epitaxially in the course of a dissolution-reprecipitation process [41].

Moreover, the inner part was a solid solution originated from the diffusion of W, Mo and other atoms since during the sintering binder also dissolves part of the hard phases. Dissolved atoms are transported by bulk diffusion and re-precipitated onto undissolved hard grains (cores) with a composition ("inner rim"). The inner rim surrounded all core particles unevenly, while the outer rim has a similar feature where the concentration of W, Mo or other heavy elements decreases depending on their solubility on the liquid binder. Grain growth occurs by small core dissolution and outer rim growth.

As we can see in the previous bibliographic review, there is a belief that the present surrounding phase could enhance the mechanical properties of the cermets. The surrounding phase would inhibit the approaching of Ti(C,N) particles with each other, improving the wetting behavior, hindering the growth and conglomeration of Ti(C,N) grains. However, the rim phase was actually a brittle phase, and when the thickness of the rim was larger than 0.5 μm, the strength could decrease sharply [77].

Effect of the processing route

As explained before in WC-Co, other investigations, according to Hall-Patch formula (not shown), have focused on the effect of the reduction of the Ti(C,N) initial particle size on the microstructure and mechanical properties of Ti(C,N)-WC-Ni cermets, where the small sizes were achieved either by using ultrafine powders or through mechanical milling. It is well known that grain refining enhance the mechanical properties of metal-ceramic composites. **Jeon** et al. [56] reported improved hardness as well as fracture toughness in the ultrafine system, as compared to conventional coarse Ti(C,N)-based cermets. **Joardar** et al. [57] studied the effect of nanocrystalline Ni binder on the mechanical properties of ultrafine Ti(C,N) cermets. Cermets with nanocrystalline Ni showed a considerably improved microstructure over cermets with commercial coarse grade Ni. Exhibiting also higher Vickers hardness values (~16GPa), along with a fracture toughness value of ~9 MPa·m$^{1/2}$. Finally, **Park** et al. [58] prepared ultrafine cermets from (Ti,W)C-Ni and (Ti,W)(C,N)-Ni nanocrystalline powders obtained by carbothermal reduction after high-energy milling. Full density cermets obtained from these powders showed significantly improved fracture resistance, ranging between 11 and 14 MPa·m$^{1/2}$.

In addition to the above, the processing route may also have a significant influence on the mechanical properties of these materials [81]. The most common processing route for cermets is the conventional powder metallurgy route, which imply the milling of powders for long times (up to 36 h in attritor ball mill, 2 to 7 days in a ball mill) using organic liquid media (ethanol, isopropanol, or others) and a binder or lubricant such as polyethylene glycol (PEG), paraffin wax or others [82]; after milling the powders are dried, and could be granulated for a better pressing behavior. Uniaxial pressing or cold isostatic pressing followed by sintering at high temperature and usually in vacuum were used to shape powders. In such route, the powder preparation step is critical, as it should provide the appropriate size and dispersion of phases as well as incorporate pressing additives. UF cermets have been also processed through spark plasma sintering (SPS) [62], hot pressing (HP) [63,65], self-propagating high-temperature synthesis (SHS) [83–86], mechanical induced self-sustaining reaction (MSR) [62,63,74], hot isostatic pressing (HIP), a combination of sintering and HIP, under vacuum, nitrogen or argon atmosphere [87] or novel and challenging techniques like additive manufacturing [88].

Direct fabrication of bulk hard materials can be realized by combustion synthesis combined with simultaneous densification under a mechanical pressure using hot pressing, SPS or extrusion [83]. A variation of this approach was reported in 2015 by **Liu** et al. [84] to obtain dense $TiC_{1-x}N_x$-Ni_3Ti cermets with a Ni_3Ti intermetallic matrix. The as-prepared cermets showed a homogeneous microstructure and a Vickers hardness of ~12GPa. **Córdoba** et al. [62] proposed a combination of MSR and SPS techniques to obtain highly dense $Ti_xTa_{1-x}C_{0.5}N_{0.5}$-based cermets. Samples exhibiting smaller ceramic particles showed an optimal combination of microhardness and fracture toughness. In this regard, **Chicardi** et al. synthesized a homogeneous Ti-based carbonitride solid solution by a MSR [74] and one year later, for manufacturing cermets based on Ti, Ti-Ta and Ti-Nb carbonitrides using Co as binder phase and Mo_2C as sintering additive obtaining smaller ceramic grains after sintered and reaching Vickers hardness values up to 15.8 GPa with K_{IC} of 3 – 4 MPa·m$^{1/2}$ and flexural strengths of 300 – 400 MPa [63].

Table 9 shows a summary of the mechanical properties obtained in different cermets processed through various techniques. The data reveal a relatively wide range of reported hardness, fracture toughness and bending strength values depending on the material and processing route employed. This has been associated with the different microstructure of the materials. In fact, it is very challenging to get uniform and homogeneous microstructures, as well as to avoid the grain growth and hard phase cluster formation by the aforementioned techniques.

Table 9. Properties of cermets via different processing routes

Route	System	Ti(C,N) Size [μm]	HV [GPa]	K_{IC} [MPa·m$^{1/2}$]	Bending strength [MPa]	Ref.	Year
PM	Ti(C,N)-WC-Ni	UF < 1 3-5	[13.6-14.5] [7-7.5]	[7.3-8.8] ---	--- ---	[56]	2002
PM	Ti(C,N)-WC-nano Ni Ti(C,N)-WC-Ni	0.7	[12.5-16.1] [13.6-14.5]	[8.4-9.1] [7.3-8.8]	--- ---	[57]	2003
PM	(Ti,W)(C,N)-Ni	UF ~ 0.4 3-4	[11.2-12.2] [8.8-9.0]	[12.0-12.6] [7.0-7.2]	--- ---	[58]	2005
PM	Ti(C,N)-Fe	7.5	[5.6-7.0]	---	---	[68]	2006
PM	Ti(C,N)-Mo_2C-Ni	2.3-3.6	[12.1-14.9]	[10.3-14.2]	---	[59]	2009
SPS	(Ti,Ta)(C,N)-Co	---	[14.0-17.4]	[3.2-5.6]	---	[62]	2013
PM	Ti(C,N)-WC- Mo_2C-NiCo	0.5	~ 11.1	~ 9.4	~ 1850	[64]	2015
HP	A. Ti(C,N)-(WC-Mo_2C)-NiCo B. Ti(C,N)-(WC-TiC)-NiCoMo	0.5	~ 17.1 ~ 13.7	~ 6.0 ~ 9.0	~ 1125 ~ 1125	[65]	2015
PM			~ 11.8 ~ 11.8	~ 11.0 ~ 11.0	~ 1375 ~ 1250		
HP	(Ti,Mt)(C,N)-Mo_2C-Co Mt=Ta,Nb		[9.6-15.8]	[3.1-4.6]	[230-485]	[63]	2016
PM	Ti(C,N)-Mo_2C-Cr_3C_2-Fe	5.13	[3.1-7.7]	---	[1000-2055]	[69]	2017

PM: Uniaxial pressing + Pressureless Sintering (PLS); UF: Ultrafine

In this thesis, colloidal and powder metallurgical techniques have been combined in order to produce cermets with different composition (i.e. metal content and composition and carbon addition) through different forming methods such as Slip Casting (SC), Slip Casting + Cold Isostatic Pressing (SC-CIP) and Spray-dry + Pressing of the spherical granules generated (SDP).

1.4 Colloidal processing

The great advances in the fundamentals of colloid chemistry knowledge has allowed to demonstrate that colloidal processing[1] is a simple, low energetic and costly efficient procedure, which implies the formation of high solid content and stable slurries in aqueous media, to produce complex shaped ceramics and metal-ceramic composites with better microstructural uniformity and higher reliability than the conventional dry processing routes. However in the case of both non-oxide ceramics and metal particles, aqueous suspensions could be an important drawback due to the elevated reactivity of these materials with the suspension media.

From an electrochemical point of view, water is one of the more complex liquid media to work with. It has a very high polar moment which requires tight control of the colloidal and chemical stability of the slurries [89–91] to prevent particle oxidation, while maintaining the interparticle repulsion networks and thus the slurry dispersion and stability. However, in addition to the superficial stability of the particles within the dispersion, slurry flow conditions are another factor of vital importance for the colloidal shaping. The rheological behavior of the high solid content slurries must provide a homogeneous mixture of phases, as well as avoid risks of segregation that may arise during the processing of the bulk pieces.

The advantages offered by the colloidal route have been demonstrated in the processing of Ni and Ni composites [92,93] and Fe based cermets [54] providing controlled microstructures through a very intimate mixture of ceramic and metal phases, using particles in the micrometric range and avoiding energetic mechanical milling.

---

[1] A colloidal dispersion is a multiphase system in which one phase (or more) is dispersed in a medium. The term “colloid” is used to describe particles that possess at least one dimension within the nanometer (10^{-9} m) to micrometer (10^{-6} m) range.

1.4.1 Dispersion and stabilization of suspensions

In colloidal suspensions, there are particles immersed in a surrounding medium. The total interaction between particles is the result of particle–medium interactions and further particle–particle developed networks [94].

Colloidal stability is governed by the total interparticle potential energy, V_{total}, which can be expressed as:

$$V_{total} = V_{vdW} + V_{elect} + V_{steric} + V_{structural} \qquad (1)$$

Where V_{vdW} is the attractive potential energy due to long-range van der Waals interactions between particles, V_{elect} the repulsive potential energy resulting from electrostatic interactions between like-charged particles surfaces, V_{steric} the repulsive potential energy resulting from steric interactions between particle surfaces coated with adsorbed polymeric species, and $V_{structural}$ the potential energy resulting from the presence of non-adsorbed species in solution that may either increase or decrease suspension stability.

The first two terms of Eq. (1) constitute the well-known DLVO theory developed by Derjaguin and Landau [95] and Verwey and Overbeek [96]. This theory predicts the stability of colloidal particles suspended in polar liquids being the cornerstone of modern colloid science.

1.4.1.1 Attractive forces between particles

One of the most important features of a colloidal dispersion is the strong tendency of particles to aggregate due to their large specific surface. Encounters between particles dispersed in liquid media occur frequently and the stability of dispersion is determined by the interaction among the particles during these encounters. The principal cause of aggregation is the existence of long-range forces resulting from **van der Waals (vdW)** interactions. These forces are ubiquitous and always attractive between particles and they exhibit a power-law distance dependence whose strength depends on the dielectric properties of the interacting colloidal particles and intervening liquid medium. Van der Waals forces arise from three different phenomena [97]:

(i) **Keesom interaction**: the interaction between a permanent dipole with other permanent dipole.

(ii) **Debye interaction:** the interaction between a permanent dipole with a polarizable atom that produces an induced dipole.

(iii) **London dispersion interaction**: when no permanent dipoles are present, instantaneous dipoles are formed due to fluctuations in the distribution of electronic charge.

To counteract them and promote stability, equally long-range repulsive forces are required. This can be achieved by different ways which can be generalized in two general mechanisms: the electrostatic mechanism, resulting from the interactions between charged particles in a medium, and the polymeric mechanism, where stabilization arises from the effect of polymers in the medium.

1.4.1.2 Repulsive forces between particles

Electrostatic mechanisms

The stability of aqueous colloidal systems can be controlled by generating like-charges of sufficient magnitude on the surfaces of suspended ceramic particles. The resulting repulsive V_{elect} exhibits an exponential distance dependence whose strength depends on the surface potential induced on the interacting colloidal particles and the dielectric properties of the intervening medium (Figure 6a).

Most substances develop an electric surface charge when brought into a polar liquid. Typical charging mechanisms are ionization, ion adsorption and ion dissolution. This surface charge influences the distribution of nearby ions. Ions of opposite charge (counterions) are attracted towards the surface and ions of like charge (co-ions) are repelled away from the surface. This leads to the formation of an electric double layer made up of the charged surface and a neutralizing excess of counterions over co-ions distributed in a diffuse manner in the polar medium.

The Stern model, showed in Figure 6b, considers that the double layer is divided into two parts separated by a plane (the Stern layer) located at about a hydrated ion radius from the surface, and also considered the possibility of specific ion adsorption. Specifically adsorbed ions are attached to the surface by electrostatic and/or van der Waals forces strongly enough to overcome thermal agitation. The centers of specifically adsorbed ions are located in the Stern layer, i.e. between the surface and the Stern plane. Ions with centers located beyond the Stern plane form the diffuse part of the double layer.

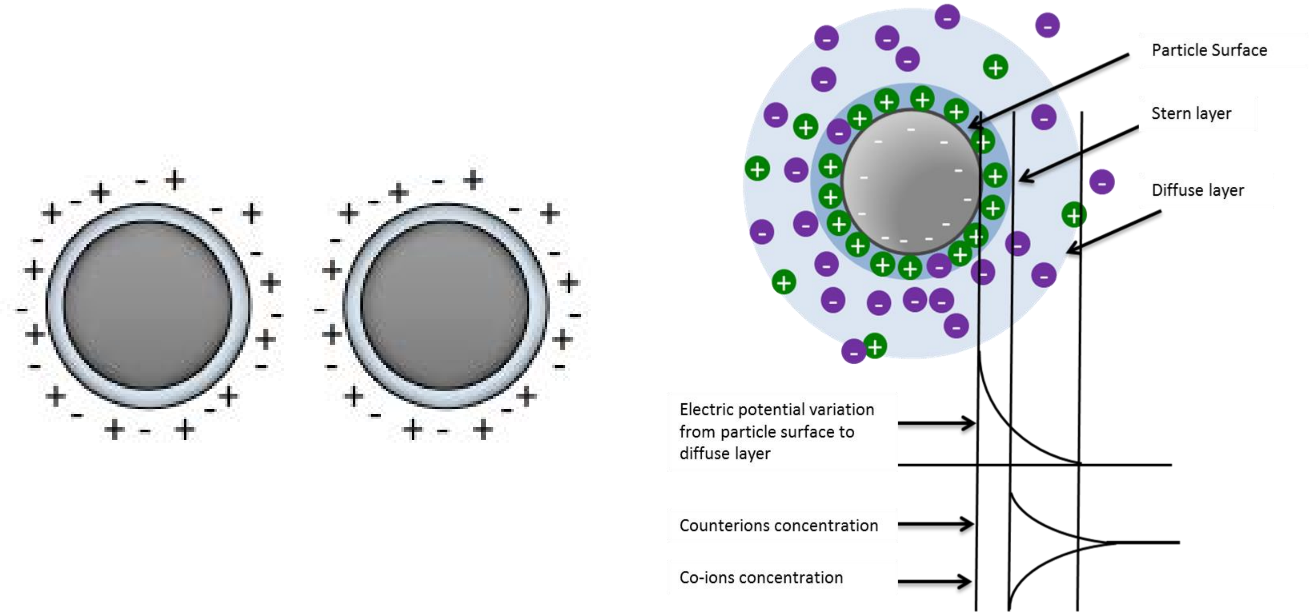

Figure 6. (a) Electrostatic stabilization and (b) Diagram showing the ionic concentration and potential difference as a function of distance from the charged surface of a particle suspended in a dispersion medium. [98–100]

Polymeric mechanisms

Addition of suitable polymeric dispersants is commonly used to create colloidal stable suspensions. These polymeric additives can induce a physical interparticle repulsion that prevents coagulation. Upon the close approach of two particles covered with adsorbed polymer layers, the interpenetration of the polymer layers give rise to a repulsive force, the so-called steric stabilization. Polymeric stabilization may be achieved by three different mechanisms.

Steric mechanisms

Steric forces provide an alternative route of controlling colloidal stability that can be used in aqueous and non-aqueous systems. In this approach, adsorbed organic molecules are utilized to induce steric repulsion. To be effective, the adsorbed layers must be of sufficient thickness and density to overcome the van der Waals attraction between particles and to prevent bridging flocculation. Such species should be strongly anchored to avoid desorption during particle collision. The conformation of adsorbed layers can vary dramatically, depending on solvent quality, molecular architecture, number of anchoring groups, active surface site density, and colloid and organic concentrations in solution. As an example, schematic illustrations of such layers adsorbed are shown in Figure 7.

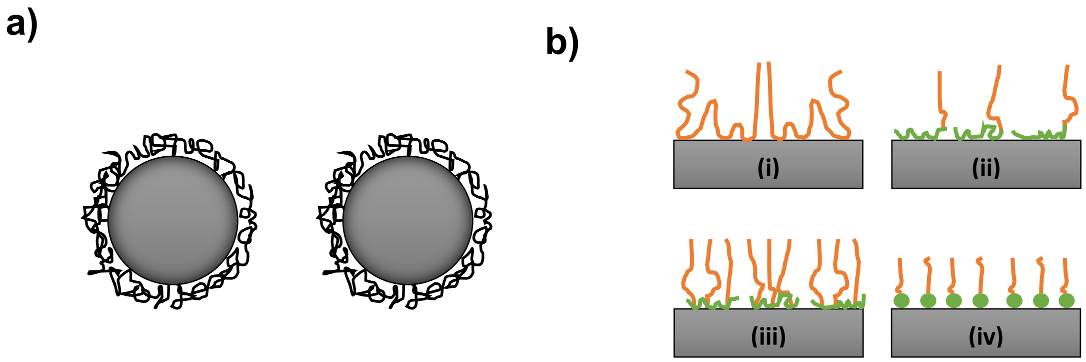

Figure 7. a) Steric stabilization and b) Schematic illustrations of adlayer conformation on an ideal surface as a function of varying molecular architecture: (i) homopolymer, consisting of tails, loops, and train configuration; (ii) diblock copolymer, consisting of short anchor block and extended chain block; (iii) comblike copolymer, consisting of extended segments attached to anchored backbone; and (iv) functional, short-chain dispersant, consisting of anchoring head group and extended tail. [101]

Electrosteric mechanisms

Polyelectrolyte species are widely used additives that can impart electrostatic and steric stabilization to a given colloidal dispersion. Such systems are often referred to as electrosterically stabilized. Polyelectrolytes contain at least one type of ionizable group (e.g., carboxylic or sulfonic acid groups), with molecular architectures that range from homopolymers to block copolymers with one or more ionizable segments. Polyelectrolyte adsorption is strongly influenced by the chemical and physical properties of the solid surfaces and solvent medium. For example, adsorption is strongly favored when polyelectrolyte species and the colloid surfaces of interest carry opposite charges.

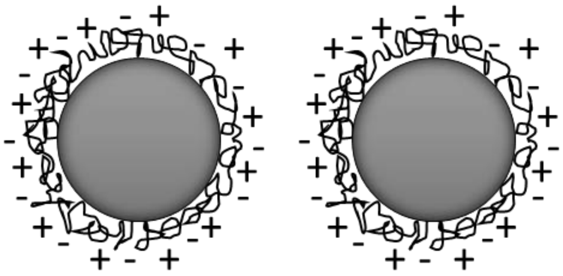

Figure 8. Electrosteric stabilization

Depletion mechanisms

Depletion forces occur between large colloidal particles suspended in a solution of non-adsorbing, smaller species (e.g., polymers, polyelectrolytes, or fine colloidal particles) as it can be seen in Figure 9. Such species, known as depletants, may promote flocculation or stabilization of primary colloidal particles. Depletion denotes the existence of a negative depletant concentration gradient near primary particle surfaces.

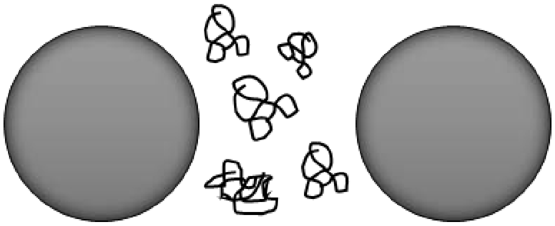

Figure 9. Depletion stabilization

The predominance of repulsive forces (particle-solvent interaction) in colloidal systems determines the potential energy balance of particle interaction. By controlling these interaction forces, it is possible to prepare dispersed and stable suspensions that allow obtaining materials with high green densities. The figure 10 shows a scheme which describes particle interaction as a function of distance as the consequence of the addition of the exponential decay of the repulsive term and the more steeply decaying one-over-distance relationship of the attractive term. This outline further illustrates the three singular features: coagulated, stable and flocculated systems.

(i) A primary minimum where particle surfaces enter into contact leading to coagulation, where particles can be hardly redispersed.

(ii) A maximum that creates effective activation energy for aggregation. The larger the barrier, the longer the system will remain stable.

(iii) A secondary minimum, where particles do not touch each other thus leading to flocculated particles that can be easily redispersed.

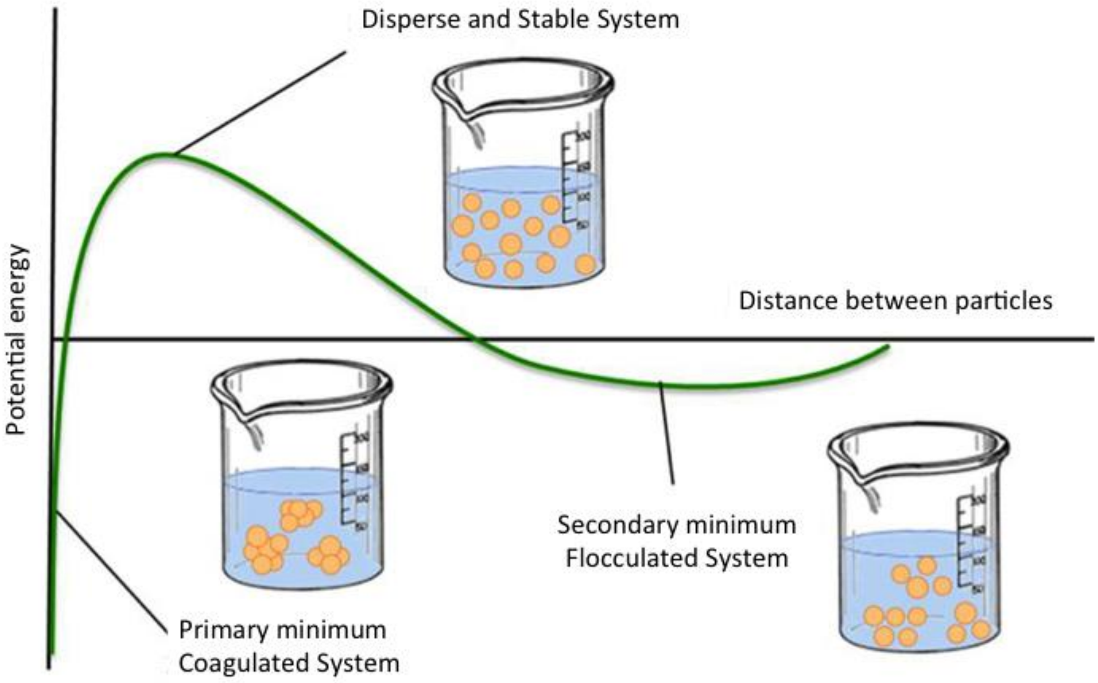

Figure 10. Potential energy curve.

1.4.2 Zeta Potential

A point of special interest in the double layer model (DVLO) is the potential where the diffuse layer and the Stern layer are joined. This point, called Zeta potential, is defined as the value of the electric potential existing in the plane of shear between the two layers.

This potential is a priori an indirect measure of the surface charge of the particles by reference to the nature of the solvent and is determined from measures of electrokinetic mobility by the Helmholtz-Smoluchowski (Eq. (2)):

$$\zeta = \frac{\eta\mu_e}{\epsilon\varepsilon_O\varepsilon_e}f(a) \qquad (2)$$

The zeta potential represents an effective way of controlling the behavior of the colloid or particle in a liquid media. This parameter indicates changes in surface potential and repulsion forces.

There are two characteristic points that define the surface state of the particle in the solvent, and are the isoelectric point and the zero load point [102]. The isoelectric point (IEP) is the pH value for which the value of the zeta potential is zero, and it is identified with the secondary minimum (Figure 11). The IEP value depends on the nature of the particle surface and the conditions of the medium and can be modified by the adsorption of stabilizing or dispersing additives (polyelectrolytes and/or organic molecules).

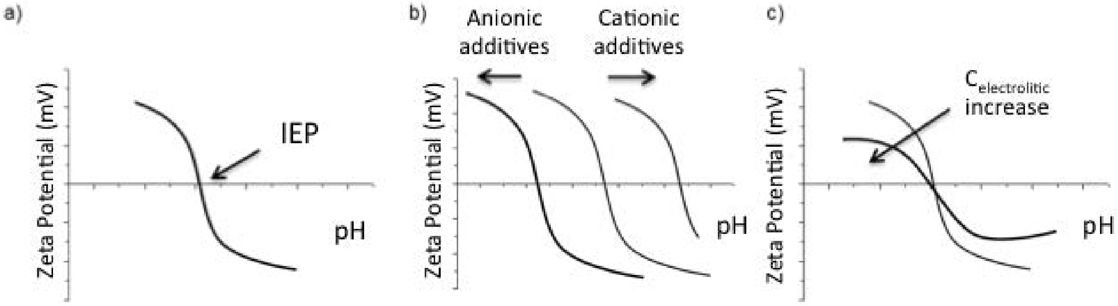

Figure 11 Variation of the zeta potential as a function of a) pH, b) adsorption of additives and c) ionic concentration of the medium

On the contrary, when the positive charges are equal to the negative ones at the surface, we find the zero load point, which is identified with the primary minimum (Figure 10), and therefore with the maximum instability of the system.

However, suspensions stabilized by purely electrostatic mechanisms can easily be destabilized by some change in the ionic concentration of the medium and therefore the use of dispersing or stabilizing additives is very common to ensure additional physical or steric stabilization. Moreover ceramic processes make use of concentrated suspensions, in which particle interactions are very frequent leading to overlapping among double layers. Then, DLVO theory has important restrictions and zeta potential measurements provide limited information.

1.4.3 Rheology of concentrated suspensions

For the characterization of concentrated suspensions, the best tool is the rheology. Rheological measurements monitor changes in flow behavior in response to an applied stress (or strain). Considering that flow behavior of concentrated suspensions is determined by particle-particle interactions. This technique is very sensitive to any variations in the stability conditions (i.e. deflocculant type and concentration, pH, presence of other electrolytes and additives, etc.), mixing conditions, particle size distribution and shape, solids loading, etc. Moreover, knowledge and adjusting of rheological behavior is essential in processing operations that involve slurries or pastes, including beneficiation, shape forming, and coating / deposition. Suspension, structure, and, hence stability can be inferred from the observed behavior.

The apparent viscosity (η) is related to the applied shear stress (τ) and shear rate ($\dot{\gamma}$) by the following expression (Eq. (3)):

$$\tau = \eta \cdot \dot{\gamma} \qquad (3)$$

Various types of flow behavior can be observed under steady shear depending on suspension composition and stability.

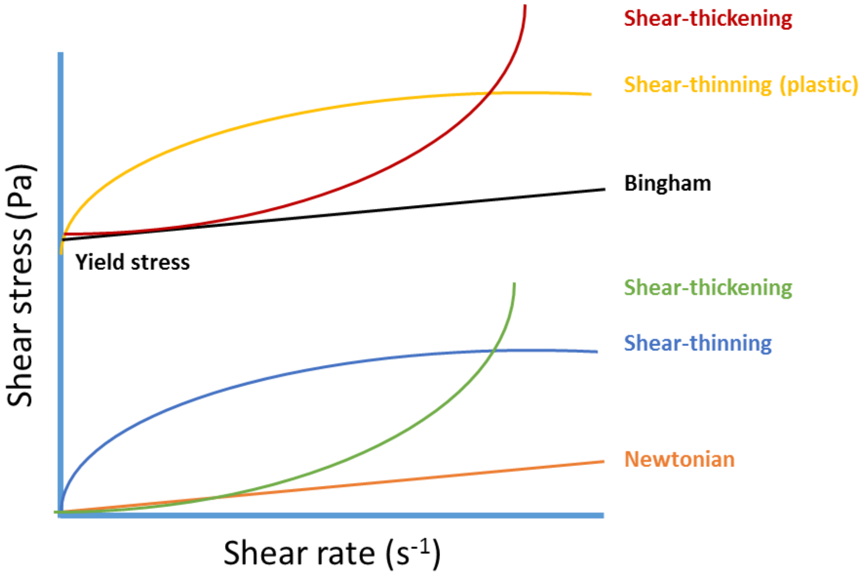

Figure 12. Classification of rheological behavior under steady-shear conditions, plotted as shear stress versus shear rate

By definition Newtonian behavior is the simplest flow response where the viscosity is independent of shear rate and does not depend on the shear history. Most simple liquids such as water, acetone or oils are Newtonian. Liquids showing any variation from this behavior are referred to as non-Newtonian. Figure 12 illustrates plots of shear stress versus shear rate (the so called flow curves). Most common colloidal suspensions are shear thinning (also referred to as pseudo-plasticity) because the viscosity decreases as the shear rate increases. This response can be accompanied by a yield stress whose magnitude depends on the strength of the particle network. If the flow curve is linear above τ_y, the system is referred to as a Bingham plastic. Finally, shear thickening occurs when viscosity increases with shear rate.

The rheological properties of concentrated colloidal suspensions are often time dependent. Thixotropic systems exhibit an apparent viscosity that decreases with time under shear, but recovers to its original viscosity when flow ceases. The opposite behavior is referred to as rheopexy.

There are different mathematical models or equations that describe each of the above behaviors. Table 10 shows the characteristics of each of them adjusted to a specific model.

Table 10. Mathematical models describing rheological behavior.

Flow		**Model**	**Equation**
Linear	Newtonian	Newton	$\tau = \eta \cdot \dot{\gamma}$
	Bingham plastic	Bingham	$\tau = \tau_0 + \eta_B \cdot \dot{\gamma}$
Non-linear	Plastic	Casson	$\tau = \left[\tau_0 + (\eta_P \cdot \dot{\gamma})^{1/2}\right]^2$
	Plastic with yield point	Herschel-Bulkey	$\tau = \tau_0 + K \cdot \gamma^n$
	Dilatant	Ostwald de Waele	$\tau = K \cdot \gamma^n$
	Pseudo-plastic	Cross	$\tau = \dot{\gamma}\left[\eta_\infty + \left[\frac{\eta_0 - \eta_\infty}{\left(1 + \left(\frac{\dot{\gamma}}{\dot{\gamma}_b}\right)^n\right)}\right]\right]$

The model proposed by Cross is one of the most used because it allows studying differences in the flux behavior between within the low and high shear regions. This model includes extrapolated values of Zero Shear Viscosity (η_0) and Infinity Shear Viscosity (η_∞). The term η_0 informs about the stability of the suspension against phenomena of phase segregation and sedimentation of heavy particles. The higher this value, the lower the mobility of the particles, and therefore the more stable the suspension is at rest. On the other hand, the parameter η_∞ gives information on the effectiveness of the suspension homogenization and dispersion processes. The lower value of η_∞ the greater the homogenization capacity of the suspensions in high shear processes.

In addition to these terms, the Cross model depends on $\dot{\gamma}_b$ which is the consistency index and parameter n which indicates the degree of pseudoplasticity of the suspension (0 for Newtonian fluids and 1 for pseudoplastics).

Another of the most used models is the one of Casson, by means of which the τ_0 can be obtained, that is defined like the yield point of the slurry, and indicates the minimum effort that has to be surpassed to begins to flow and the η_p that is the limiting viscosity.

1.4.4 Estimation of the Maximum packing density: The Krieger Doherty Model

The viscosity of a suspension is strongly dependent on the solids loading, with the viscosity approaching infinity at a maximum volume fraction, Φ_m. The latter relates to the particle concentration at which the average separation distance between the particles tends to zero and the particles pack together, thus making flow impossible. Most emerging forming routes require concentrated colloidal systems, with volume fraction (Φ) approaching 0.6. The maximum value of packing attainable is 0.62, assuming an inorganic system of hard-spheres in which all particles are equal and packed in an octahedral coordination. Although this is readily achieved in model hard-sphere systems, suspensions often consist of irregularly shaped particles with adsorbed and/or non-adsorbed processing aids that serve to effectively increase the solid loading. So in real experimental systems, the maximum volume fraction is strongly dependent on the particle size distribution and the particle shape and synergistic effects among them. For example, a broad particle size distribution displays a higher value of Φ_m because of the small particles can fit into the voids between the large ones. Moreover, when the particles in suspension are non-spherical, the rotation of the particles due to Brownian motion results in an excluded volume, which is higher than the volume-fraction of the particles. As the degree of anisotropy increases, the effects become more dramatic.

The experimental points were fitted to a modified Krieger–Dougherty (Eq. (4)), where η, the intrinsic viscosity (Pa·s), evolves with Φ, the volumetric fraction of particles in the suspension, following an exponential law:

$$\eta_r = \left(1 - \frac{\phi}{\phi_m}\right)^{-n} \qquad (4)$$

where Φ_m is the maximum packing fraction, which gives an idea of the maximum permissible solids content in a suspension without any aggregation or agglomeration phenomena. To simplify this model, the exponent is usually replaced by a parameter called “n” which depends on the shape of the particle.

1.4.5 Shaping and Granulation processes

Shaping is the process by which the final piece is obtained from the colloidal suspensions. One of the main objectives of colloidal processing is to minimize the population of defects produced during manufacture in order to obtain a part with the best performance and in a reproducible way. During the forming process from suspensions, compaction of the suspension particles occurs either by the removal of the liquid, or by the condensation (chemical or physical) of the dispersed phase. There are different methods of forming colloidal suspensions, but all of them start from the same premise: a stable and homogeneous suspension is required. At this point, everything concerning the stability and rheology of concentrated suspensions described throughout this chapter is taken into account, but the final requirements of the suspension will depend on the shaping technique employed.

The different forming methods can be classified according to the need to use molds or not. *Casting techniques* are based on the shape of the final piece by means of a mold that guides the final shape. It is the most traditional methodology and therefore the most widespread for suspension forming. This set of techniques requires an additional step of demolding the final part. There are a variety of techniques, which can be classified in turn depending on whether the solvent is removed during forming. Physical coagulation, chemically gelled casting, dipping and injection molding are examples of casting without solvent removal whereas slip casting, pressure casting, centrifugal casting and electrophoretic deposition are examples where solvent removal is required. On the other hand, *freeform casting* consist in a bunch of techniques which allows obtaining solids with complex structures, without the need to use casts. In the last years a great number of methodologies and variants have been developed depending on the requirements of the final material, but all of them are based on the habitually additive manufacture layer by layer. Depending on the method of deposition and compaction of the final material we can distinguish several general methods such as tape casting, stereo lithography, 3D printing, robocasting or inkjet printing.

Slip casting is a potter's term for a technique which, on the one hand, permits the precision manufacture of ceramics and, on the other, tends itself to mass production. This technique was invented in Europe in the 18th century and became an important industrial process in 19th. In Slip casting, pieces are formed by pouring slip, a concentrated suspension of ceramic particles in water, into absorbent molds. The porous structure of the mold made of Plaster of Paris provides a suction pressure ranging from 0.1 to 0.2 MPa and draws out moisture through the mold interface, pulling the slip material into the desired shape [103].

In addition to all these shaping techniques discussed above, among the industrial methods of powder manufacturing, the probably most versatile powder processing method is the granulation through spray-drying. Spray drying is the process by which a water or organic based suspension (slurry) is transformed into a dry powder by spraying the fluid feed material into a hot drying medium. This process is a widely used method of producing granulated feed material for compaction processes. Indeed, spray drying enables the fabrication of composite powder by aggregation of any kind of small particles using an appropriate organic binder. Atomizing and drying lead to a large variety of powder shapes; from uniform solid spheres which are regarded as ideal granules for most spraying systems to elongated, pancake, donut shaped, needlelike or hollow granules. Previous studies paid a great attention to the effects of feed characteristics and dryer operational conditions on the size distribution of the atomized droplets. But, very few authors have discussed on the importance of the slurry formulation on the characteristics of the ceramic granules and on the drying process while noticing that it is a non-negligible factor.

1.5 Design of nanostructured Ti(C,N)-based cermets

The extraordinary effects of the reduction of particle size of metals (precious and non-precious) and ceramic semiconductors have been widely reported in different fields of the nanotechnology, such as energy storage, optoelectronics, photocatalysis or optical bioimaging. In Hard Metals, a wide number of research studies report the influence of the reduction of the ceramic particle size in the final structure and mechanical properties of those materials [24,56–58]. Most recently, the reduction of both the content and the size of the (metal) binder phase have also received special attention since it implies relevant physico-chemical changes during its manufacture (see Table 8). For example, the use of nano-metals could allow, among others, reducing the temperature of sintering, similarly to other processing strategies already validated, such as the addition of carbon or alloying elements [72–74,104,105].

In fact, the manufacture of metal-ceramic materials, especially with ultra-high temperature ceramics (UHTCs), such as carbides, nitrides, borides and oxides of early transition metals, presents mainly two drawbacks. First, the low wettability of some metals and ceramics, such as the Ti(C,N)-Fe-based composites, is the objective of this study. But also, the high melting point and strong covalent bonding of these ceramics which difficult their uniform densification, only achieved at temperatures above 1800˚C once the grain boundary diffusion mechanisms are activated. Consequently, the metal melting, and its wettability and reactivity with the ceramic reinforcement, are crucial to achieve bonding between both phases during the processing of metal-matrix composites (MMC). The description of the sequence of all phenomena which take place during sintering is still challenging due to the extraordinary amount of parameters that should be controlled. In this sense, the formulation of Ti(C,N)-Ni composites, in which wettability and reactivity among phases are extensively demonstrated [106], could contribute to better understand the mechanism of sintering of Ti(C,N) based cermets.

In colloidal processing, in addition to the microstructural homogeneity and other advantages offered by the mixture of powders via aqueous suspensions (for their later granulation [107,108]), wet routes allow processing of nanometric and sub-micronic particles, and also the in situ synthesis of nanoparticles (NPs) from precursors dissolved in the suspension [109].

In this research work, we propose the in situ synthesis of nickel NPs on Ti(C,N) microparticles stabilized in aqueous media, as a strategy for processing improvement of based Ti(C,N) cermets. For that, this section is aimed to summarize the state of the art of two alternative “bottom-up” approaches for nickel NPs syntheses. Both routes are based on the chemical reduction or precipitation of Ni precursors in the Ti(C,N) suspensions, in order to produce core-shell composites as feedstock for further granulation and shaping processes. Selected syntheses are: (i) the electroless Ni plating and (ii) the reduction/precipitation of Ni based species with the aid of ultrasound (sonocrystallization).

1.5.1 Electroless Ni plating of micrometric particles.

The advances in new synthesis techniques lead to the processing of a wide variety of core-shell particles which cover a large range of applications [110]. According to the materials nature, core-shell structures can be classified into four main groups: (a) inorganic/inorganic, (b) inorganic/organic, (c) organic/inorganic and (d) organic/organic. Among inorganic/inorganic core-shell structures, in composites with a ceramic core and a metal shell, metal NPs can endow the ceramic particles with particular electrical, magnetic and chemical properties and simultaneously optimize the surface compatibility.

In general, core-shell nanostructures can be prepared in many ways, for example by chemical vapor-liquid reaction [111], atomic layer deposition (ALD) [112,113], spray drying [114], sonocrystallization [115], hydrothermal route [116], seed-mediated growth precipitation [117], ball milling [118], electroless plating, and so forth. Among these methodologies, electroless plating, invented in 1946 by Brenner and Riddell, allowed uniform deposits of coating materials over all surfaces, regardless of size, shape and electrical conductivity.

This process consists in an autocatalytic reduction of metal ions from an aqueous solution onto the surface of particles used as substrate without the application of external current. Usually, the electroless plating process consists of three main steps: the first one consist in a surface modification of the particles substrates with Sn^{2+} ions (in a process called Sensitization), the second one is a redox reaction in which the Sn^{2+} ions get oxidized to Sn^{4+} and at the same time Pd^{2+} ions get reduced into metallic Pd^0 which adheres to the surfaces (during the activation step). The third consists in the reduction of the desired metal particle on the Pd seeds pre-deposited on the core particles.

As it was reported in literature, electroless plating process allows to coat particles surfaces with different metals such as gold (Au) [119,120], copper (Cu) [121], cobalt (Co) [122], but mainly with Ni. Besides, it is also possible to coat a wide range of materials surfaces, natural such as cotton fabric [123] and beech wood fibers [124], glass microspheres [125], polymers such as polystyrene (PS), polypropylene (PP) and polyethylene (LDPE and HDPE) [126,127], polyimide (PI) and poly(ethylene terephthalate) (PET) [128], metals as iron [129–131], tungsten [132], steel alloys [133], oxidic ceramics SiO_2 [134], Al_2O_3 [134–137], CeO2 [137], ZrO_2 [138] and non-oxidic ceramics such as BN [137], SiC [139–144], basalt fibers [145], carbon nanotubes [146,147], graphite [148], Si_3N_4 [149].

Electroless coatings are widely used in the mechanical, chemical and electronic industries because of their unique corrosion and wear resistance, hardness, lubricity, uniformity of deposit regardless of geometries, and solderability properties. Among other applications, coating the ceramic particles with a metallic layer always promotes wetting between the reinforcement phases and the metallic matrix for metal matrix composite (MMC) materials. The metallic surface layer on the ceramics contributes to interface bonding between the composite constituents. In Ti(C,N) based cermets, it has been demonstrated that Ni plays and important role as binder, since its presence widely improves mechanical properties.

The basic requirement for an electroless bath includes metal ions/their concentration, reducing and complexing agents, bath stabilizers and buffers. The additives regularly used, and their role, are:

- *Reducing agents.* Many reducing agents acting simply as electron donors have been commercialized including sodium hypophosphite, amino boranes, sodium borohydride, and hydrazine.
- *Complexing agent.* Complexing agents are added to prevent the decomposition of solutions and to control the reaction so that it occurs only on the catalytic surface. Complexing agents are organic acids or their salts, added to control the amount of free electron available for reaction. Complexing agents also buffer the solution and retard the precipitation of metallic nickel. Ammonia, hydroxides, or carbonates may also have to be added periodically to neutralize hydrogen. The complexing agent used in the plating solution can also have an effect on the quality of the deposit, especially on its phosphorus/boron content, internal stress and porosity.
- *Accelerators.* They are often added to the plating solution in small amounts to increase the speed of the deposition and can cause the plating rate to become economically high. Accelerator main function is to lose the bond between hydrogen and phosphorus atoms in

the hypophosphite molecule, allowing phosphorus to be more easily removed and absorbed onto the catalytic surface.

- *Inhibitor and by-products.* The addition of inhibitors, also called stabilizers, can have harmful as well as beneficial effects on the plating bath and its deposit. In small amounts, some inhibitors increase the rate of deposition and the brightness of the deposit.

Based on the above, this work is aimed to develop an alternative hybrid semiconductor-metal core-shell structure. The deposition of Ni onto Ti(C,N) particles surfaces by using a $NiSO_4 \cdot 7H_2O$ precursor via the electroless Ni (EN) plating method was investigated using N-dimethyl amine borane (DMAB) as reducing agent. This infrequent commercial amino borane, useful for plating non-catalytic surfaces such as ceramics, is an effective reducing agent over a wider range of pH compared to the habitual reducing agents, such as borohydrides [150], while leaving a low amount of impurities, something of vital importance in furute applications. Sodium citrate (CIT) was used as complexing agent and lactic acid (LA) was used as a chemical buffer in the electroless plating bath. The process of Ni deposition and pre-treatments of Ti(C,N) particles are reported in detail.

It is important to note that this technique has also limitations. For example, the low particle concentration in suspension with which this procedure can be carried out (<< 1% solid content) limits its final application as a technique for the production of bulk powder.

1.5.2 Synthesis of Ni-based NPs assited by ultradounds

The chemical activation of the surface of the Ti(C,N) particles achieved during the application of the regular protocol for electroless plating, could be replaced by a sonic activation.

There are a large number of manuscripts in the literature describing the homogeneous precipitation of Ni-based NPs (Ni and $Ni(OH)_2$). They describe how the application of ultrasound (US) in a precursor bath disperses nuclei and disturbs the crystallographic order and the lattice staking of $Ni(OH)_2$ nanostructures, and also how ligands (such as citrate (CIT) or polyvinylpyrrolidone (PVP)) and reducing agents (such as hydrazine) favors the final formation of $Ni(OH)_2$ and Ni nanoparticles in a homogeneous synthesis [151–153]. Moreover, the use of US activation for nanostructures production hasn't apparently limits related to the amount of synthesized nanoparticles or the solids content of the resulting suspensions. Only the S parameter, which is the equivalent of the amount of power in watts per cm^2 that a mol of precursor experiences and then quantify the effectiveness of sonication, should be optimized.

Up to our knowledge, this kind of syntheses has never been applied using ceramic particles as seeds to step up the Ni-based species nucleation. However, US could be applied in high solid content aqueous suspensions, so it could be an alternative in the heterogeneous synthesis of metallic nanoparticles in Ti(C,N) suspensions in order to shape or granulate Ni/Ti(C,N) materials.

The most significant results described in the literature, recording the control parameters of the homogenous syntheses of $Ni(OH)_2$ and Ni NPs in aqueous media, are summarized as follow:

Nickel hydroxide synthesis: α-$Ni(OH)_2$ and β-$Ni(OH)_2$

$Ni(OH)_2$ crystallizes in two different polymorphs, α-$Ni(OH)_2$ and β-$Ni(OH)_2$. Both are laminar hydroxides with beta phase being the stable phase which crystallizes in a hexagonal crystallographic structure isostructural with brucite, where each Ni atom is coordinated to six hydroxyl groups creating an octahedron. On the other hand, α-$Ni(OH)_2$ is a metastable phase due to a lack of hydroxyl groups within it is structure. This metastable phase has not a well-defined crystallographic structure [151].

The conditions of the synthesis of $Ni(OH)_2$ powders can be established according to the analysis of the diagram of predominant species as a function of pH and log [Ni^{2+}] (Figure 13), and the general scheme for the synthesis can be depicted as follows:

$$Ni^2 + X\,NH_3 \rightarrow [Ni(NH_3)_x^{2+}] \qquad (5)$$

$$[Ni(NH_3)_x^{2+}] + 2OH^- \overset{)))^*}{\leftrightarrow} Ni(OH)_2 + X\,NH_3 \uparrow \qquad (6)$$

***))) = Ultrasound**

The most common methods for obtaining α-$Ni(OH)_2$ and β-$Ni(OH)_2$ involve either chemical precipitation from nickel salts [154,155] or hydrothermal synthesis [156,157]. For example, **Meyer** et al. [155] studied the synthesis of $Ni(OH)_2$ powder with different sizes and morphologies depending on the precipitation agent used and the molar ratio base-metal and **Liang** et al. [156] reported the influence of pH and reaction time during hydrothermal synthesis on those parameters in order to achieve homogeneous products. In recent years, also sonochemical synthesis routes have been reported for the synthesis of metal hydroxides [158–162] as well as for the synthesis of $Ni(OH)_2$ [151,152,158,159]. **Jeevanandam** et at. [158] prepared α-$Ni(OH)_2$ by a urea method assisted by ultrasound as well as **Vidotti** et al. [159] describes the behavior of nanosized nickel and cobalt hydroxide, synthesized by a sonochemical method, deposited onto transparent conductor electrodes (ITO) by using the electrostatic deposition layer-by-layer technique.

More recently, in 2015, **Cabañas-Polo** et al. [151] researched about the instantaneous precipitation of α-$Ni(OH)_2$ nanopowders by the addition of a nickel salt to an ammonia solution. The influence of the US on both, the microstructure and the crystalline structure was discussed and the differences were referred to a parameter called "S parameter" which quantifies the amount of power in watts per cm^2 that a mol of $[Ni(NH_3)_6^{2+}]$ experiences. The results evidences that α-$Ni(OH)_2$ grows confined in disordered nano-domains which aggregate, forming 2D nanoplatelets which arrange into 3D flower-like nanostructures. Crystallographic confinement and disorder are the cause of the formation of NiO or Ni nanoparticles, lower than 30 nm in size, after the calcination of α-$Ni(OH)_2$ powders in air of N_2/H_2 atmosphere.

In 2011 **Cabañas-Polo** et al. [152] studied the influence of gas flow, temperature and cationic, anionic and neutral surfactants in the synthesis of β-$Ni(OH)_2$ particles from aqueous ammonia complexes in terms of shape, size and agglomeration of the particles. The results of this research conclude the possibility to obtain flower-like $Ni(OH)_2$ particles with sizes ranging in between 0.7 and 1.0 μm in contrast with the 6-8 μm particles obtained in the absence of ultrasound. In this study, the concentration of reactants was adjusted to promote the formation of a very stable Ni ammonium complex (Eq. (5) and Figure 13). The decrease in ammonia concentration, induced by the effects of ultrasound in the reaction media, displaces the equilibrium and promotes the precipitation of the stable β-$Ni(OH)_2$ (Eq. (6) and Figure 13). In this synthesis, the decrease on ammonia concentration is based on a degassing process where the bubbles generated during cavitation, and that present high specific surface area, grow at expense of dissolved gasses within the liquid, in this case ammonia, up to a maximum volume. At this point, bubbles explode releasing the gas, and thus the $Ni(OH)_2$ precipitates.

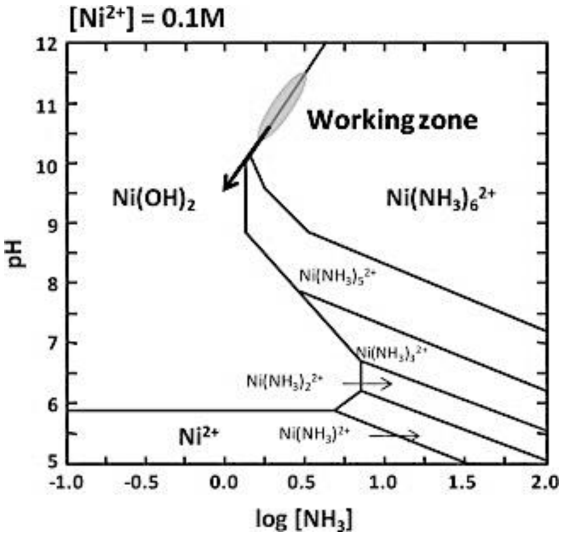

Figure 13. pH vs log [NH_3] predominance area diagram for a fixed [Ni^{2+}]=0.1 mol/L

Under the same frame of study, ligands such as polyacrylic acid (PAA), PVP, polyvinilic acid (PVC), glycerine or CIT, were used to modify the nanostructure morphology, and directly synthesize $Ni(OH)_2$ nanoparticles [153], and results show that the use of CIT as synthesis modifier leads to the precipitation of a metastable α-$Ni(OH)_2$ with a low crystallinity and irregular particle geometry in the nanometric range. The formulation of this last synthesis has been the starting point of the study of the heterogeneous synthesis of $Ni(OH)_2$ in Ti(C,N) suspensions.

Ni NPs synthesis

The metallic Ni precipitation in an alkaline bath is a common method to obtain Ni NPs by homogeneous synthesis. Among other reducing agents, hydrazine is one of the most regularly used. Hydrazine has a standard reduction potential of −1.16 V (Eq. (7)) in an alkaline solution, while Ni has a standard reduction potential of −0.25 V, and consequently it can be easily reduced by hydrazine (Eq. (8)). Therefore, the chemical reduction process of the Ni^{2+} ions can be simply shown in the Eq. (9), were the solution pH noticeably influences the synthesis of the Ni NPs.

$$N_2H_4 + 4OH^- = N_2 + 4H_2O + 4e^-; \quad E_0 = -1.16\ V \quad (7)$$

$$2Ni^{2+} + 4e^- = 2Ni; \quad E_0 = -0.25\ V \quad (8)$$

$$2Ni^{2+}\ N_2H_4 + 4OH^- \leftrightarrow 2Ni + N_2 + 4H_2O \quad (9)$$

Many formulations of the precursor solution and protocols have been described in the literature for the homogeneous synthesis of Ni NPs. Table 11 summarizes main synthesis conditions, such as solvent, Ni precursor, reducing agent, activation procedure as well as the resulting size and morphology of Ni particles. In 2003, **Wu** et al. [163] described the synthesis of Ni NPs 9.2 nm in diameter. They used hydrazine for the reduction of nickel chloride in ethylene glycol at 60°C, and suggest the role of the own solvent to prevent particle agglomeration. One year later, **Kim** et al. [164], reported a similar synthesis route using alcohols as solvents and carboximetilcellulose (Na-CMC) as processing additive, proving the effect of the variation of the reaction temperature, the length of solvent chain, and Ni^{2+} concentration [165]. They demonstrate that NPs size increases from approximately 150 nm up to 1µm, with the temperature, the number of carbons of the solvents and the precursor concentration, being the Ni content the more drastic parameter. Contrarily, the addition of Na-CMC prevented agglomeration, and contributed to the synthesis of NPs. Finally, results in those works evidenced a lack of crystallinity of the produced Ni due to the fast reduction process when using hydrazine. **Chen** et al. [166] studied the effects of reaction temperature and flow rate of a nickel sulfate solution in a flow reactor, obtaining Ni NPs of 100 nm with a narrow size distribution, while **Park** et al. [167] suggested a two-steps synthesis process in deionized (DI) water, that includes the formation of nickel hydroxide and its further reduction by a ligand exchange reaction between a nickel hydrazine complex and the base, NaOH. The standard deviation of the size of NPs decreased with the concentration of nickel hydrazine complex while the mean particle size increased.

More recently, **Couto** et al. [168] reported the synthesis of Ni NPs ranging 3.4-7.7 nm in diameter, using poly N-vinilpyrrolidone (PVP) as protective agent, sodium borohydride as reducing agent, nickel chloride as precursor and a mixture of ethylene glycol, acetone and ethanol as solvent. The presence of PVP was considered essential to prevent the aggregation and addressed the NPs growing. **Wang** et al. [169] using the same solvent and CTAB as size modifier and nickel sulfate as precursor, were able to synthesized Ni spheres of 30 nm in diameter. They identified the effect of the use of water as solvent and the surfactant addition on the morphology of the products. Finally, they describe the synthesis of flowerlike powders for high concentrations of Ni^{2+}, shaped by the aggregation of spherical NPs, but also platelet-shaped particles (80 to 120 nm in diameter), due to the polarity of water molecules. Special conditions of synthesis, as the application of inert gas and ultrasounds during the reduction reaction, were tested by **Wu** et al. [170] and **Tientong** et al. [171], respectively, obtaining pure Ni at room temperature without any organic additive, using as solvents an alcoholic mixture and water respectively. Those authors demonstrate that to get well-dispersed Ni powder without particle agglomeration, a proper Ni^{2+} concentration is needed, and a pH value over 9.5 in the precursor bath.

Table 11. Summary of main parameters of the syntheses and the characteristics of Ni NPs

Nickel Precursor	Synthesis solvent	Reductor	Additive	Process and Time	T (°C)	Particle Size	Ref	Year
Nickel Chloride	Ethylene Glycol	Hydrazine	-	Heating and stirring for 60min	60°C	9.2 nm	[163]	2003
Nickel Chloride	Ethanol 1-propanol 1-butanol	Hydrazine	Na-CMC	Heating and stirring for 45 min	40°C - 80°C	160 - 650 nm	[164]	2004
Nickel Chloride	1-propanol	Hydrazine	Na-CMC	Heating and stirring for 45 min	60°C	500 nm to 1.9 μm	[165]	2004
Nickel Sulfate	Ethanol	Hydrazine	-	Heating and stirring	53°C - 73°C	100 - 700 nm	[166]	2006
Nickel Chloride	DI water	Hydrazine	-	Heating and stirring for 60-120 min	60°C	150 - 380 nm	[167]	2006
Nickel Chloride	Ethylene Glycol Acetone Ethanol	Sodium Borohydride	PVP	Heating and stirring for 120 min	140°C	3.4 - 3.8 nm	[168]	2007
Nickel Sulfate	Ethylene glycol Acetone Ethanol	Hydrazine	CTAB	Heating and stirring for 50 min Heating and resting for 60 min	75°C	30 - 400 nm	[169]	2008
Nickel Chloride	Alcohol Acetone	Hydrazine	-	Heating and stirring for 120 min	Room	50 nm	[170]	2010
Nickel Chloride	DI water	Hydrazine	PVP	Sonication for 30 min	60°C	7 - 14 nm	[171]	2014

In our work, the chemical reduction for the syntheis of Ni NPS in Ti(C,N) supension was modified in two main aspects with respect to the results collected in the literature. On the one hand, the synthesis were carried out in aqueous solution, avoiding the use of any other kind of solvent as ethanol, methanol, resulting an environmentally friendly route, and on the other hand, nickel nitrate was used as Ni precursor instead of the more common use of chlorides and acetates, harmful precursors to the metal matrix.

Chapter 2

Motivation and Objectives

Although 90 years have passed since its invention, cemented carbide is still used today. This composite material consists of at least one hard and wear resistant phase; being mainly tungsten carbide (WC) embedded into a ductile and softer metallic binder phase from the iron group of metals (mainly cobalt, Co). Although WC is not the hardest carbide nor Co is the toughest metal, the combination of both brings to the composite material a high hardness value that is maintained at high temperature as well as high wear resistance and toughness. The reasons for the dominant role of Co are some unique properties of this binder phase as well as it is ternary system with tungsten and carbon. It is well known that the solubility of WC in Co is not only high but also strongly varies depending upon the temperature. The metallic phase is an alloy Co-W-C where the W and C are dissolved in a solid solution of Co. This two aspects are closely connected to the excellent wetting between WC and molten Co during liquid phase sintering (LPS) and their consequent mechanical properties such as high hardness, yield stress, toughness and strength.

However, different perspectives condition future developments in the field of hard materials. These investigations are motivated not only by economical factors due to the temporarily high and strongly fluctuating prices of Co and W metal powders but also due to technological and strategic aspects such as the low resistance to corrosion and oxidation of the WC-Co composite materials, the undesirable allotropic transformation of Co that causes a worsening of the mechanical properties and the strategic character of these raw materials. In addition to all the aspects discussed above, another consideration comes from the health perspective, which has increased the research activities to replace or substitute WC-Co totally or partly. In Europe, Registration, Evaluation, Authorization and Restriction of Chemical substances (REACH), so far has classified cobalt as very toxic for the human health. Also, the U.S. National Toxicology Program, NTP, states that the tungsten carbide-cobalt hard metal dust has been shown to be more toxic in combination than both pure cobalt and tungsten carbide by themselves in vitro studies. By the reasons pointed out before and the increasing demand of materials with optimized properties, one of the main topics of the actual research in the field of hard metals concerns the development of new metal-ceramic composites having comparable or superior properties than the commercial ones using more sustainable compositions and processing methods.

In this sense, Titanium Carbonitride based cermets have drawn great attention in an attempt to replace the traditional WC-Co hardmetals in specific applications. Notwithstanding their relatively lower bending strength as compared to hardmetals, Ti(C,N)-based cermets have an excellent and unique combination of physical properties such as high melting point, hardness at high temperature, wear and oxidation resistance and thermal conductivity. All these characteristics make cermets well adapted to the requirements for high performance wear parts and semi-finishing or finishing cutting tools. This fact offers the opportunity to use relatively cheap and abundant raw materials, thereby reducing the dependence on critical raw materials such as W or Co.

In most Ti(C,N)-based cermets, the binder phase is mainly composed of Ni, Co or a combination of both. However, there is an interest to find alternative binder compositions to replace them totally or partially, due to its classification as critical raw materials and the health risks. As it has been explained at the introduction, there are several studies that propose the use of Fe as a metal matrix for cermets, as it is non-toxic and cheaper than the other routes as well as strengthened by heat treatment. However, despite the considerable amount of research carried out, the application of such cermet system is limited, mainly due to two major issues: the poor wettability on Ti(C,N) particles during the liquid phase sintering (LPS) and the low toughness values resulting from the coarsening of the carbides. To overcome such limitations, the addition of alloying elements and compounds such as WC, VC, Mo_2C, TaC, Cr, Mo, Ni has been proposed aiming to improve the wetting behavior between both phases during the liquid phase sintering as well as hinder the ceramic particle growth. However, as a result of these additions a typical core-rim microstructure can be formed and a careful selection of the amount of carbides should be done to avoid the harmful effects of brittle phases formed at the rim. In this work instead of adding secondary carbides, the addition of Ni does improve notably the wetting and solubility behavior of Fe on the Ti(C,N) particles.

Although the most common route used for the preparation of cermets is still the traditional mechanical milling, cermets have been also processed through spark plasma sintering (SPS), hot pressing (HP), self-propagating high-temperature synthesis (SHS), mechanical induced self-sustaining reaction (MSR), hot isostatic pressing (HIP) or a combination of sintering and HIP, under vacuum, nitrogen or argon atmosphere. In an attempt to obtain a well-controlled microstructure and a better dispersion of phases with lower energy consumption than the rest of the conventional techniques, colloidal processing emerges as an alternative for the processing of cermets. The advantages offered by the colloidal route have provided controlled microstructures through a very intimate mixture of the ceramic and metal phases, using particles in the micrometric range and avoiding mechanical milling.

The colloidal processing implies the formation of slurries in aqueous media, which is a drawback in the case of both-non-oxide ceramic and metal particles, due to the elevated reactivity of these materials with the suspension media. From an electrochemical point of view, water is one of the more complex liquid media to work with. It has a very high polar moment which requires tight control of the colloidal and chemical stability of the slurries to prevent the particle oxidation, while maintaining the interparticle repulsion networks and thus the slurry stability. However, in addition to the superficial stability of the particles within the dispersion, their flow conditions are another factor of vital importance for the colloidal shaping. The rheological behavior of the high solid content slurries must provide a homogeneous mixture of phases, as well as avoid risks of segregation that may arise during the processing of the bulk pieces.

Among the wide range of forming methods to obtain bulk specimens with low defect population, high density and well-controlled microstructure, colloidal and powder metallurgical techniques has emerged as an attractive and affordable approach to be successfully implemented for the fabrication of cermets. But also, the reduction in both, content and size of the binder phase, can be also achieved by bottom-up approaches, mainly profiting from the chemical routes such as electroless processes. In this sense, the present work is aimed to develop an alternative route to the processing of Ti(C,N)-based cermets. Different activations have been studied to synthesize Ni NPs onto the surface of micrometric Ti(C,N) particles, producing core-shell composited to explore all the aspects that this one-pot procedure can offer to the synthesis of metal-ceramic materials.

The main objective of this thesis is the processing by combining colloidal and powder metallurgy techniques in aqueous medium of Ti(C,N) based cermets and their mechanical characterization.

To achieve this objective a number of sub-goals have been contemplated.

1.- Establish the metal binder composition.

- Thermodynamic study of the Ti(C,N)-FeNi system to identify possible metal binder candidate compositions.
- Evaluate wetting and infiltration properties in the systems studied

2.- Processing and sintering of Ti(C,N)-FeNi materials

The objective in processing the determined compositions is to improve the mechanical properties of the final material. A combination of colloidal and Powder Metallurgy techniques was proposed to process Ti(C,N)-based cermets.

-Determine the behavior of the liquid phase during sintering

-Identify the temperature range in which the main thermal events (redox, melting, diffusion..) take place depending on the atmosphere used.

- Study the sintering conditions suitable for processing and evaluate the behavior of the materials according to the sintering conditions.

3.- Evaluation of the mechanical properties

- Characterize the mechanical properties of the materials depending on the processing route, the metal matrix fraction and the carbon content. It is intended to known the improvement that each of the variables can offer in the final properties.
- Identify the failure mechanism through the fractographic analysis of the samples.

The main goal is to understand the requirements for sintering this type of metal-ceramic materials, which would help to obtain robust and reliable products likely to be eventually introduced in the market.

4.- Study of the synthesis of nickel and nickel hydroxide nanoparticles from compatible complexes in aqueous medium.

To this end, a broad study has been carried out on the balance of nickel and nickel hydroxide in aqueous medium that allows determining the optimum experimental conditions to carry out the syntheses.

The effects of the use of different activation techniques on the syntheses will be studied. The ultrasound activation will be proposed as an alternative route to the traditional chemical activation.

5.- One-pot procedure to obtain Ti(C,N)-Ni bulk materials

With the aim of being able to process metal-ceramic materials from the deposition of metallic nano phases, it is proposed to investigate a bottom-up approach to develop a one-pot procedure that allows synthesizing these nanoparticles in the suspension medium of the ceramic particles.

Subsequently, after the optimization of these syntheses, different processing techniques will be evaluated to obtain bulk pieces.

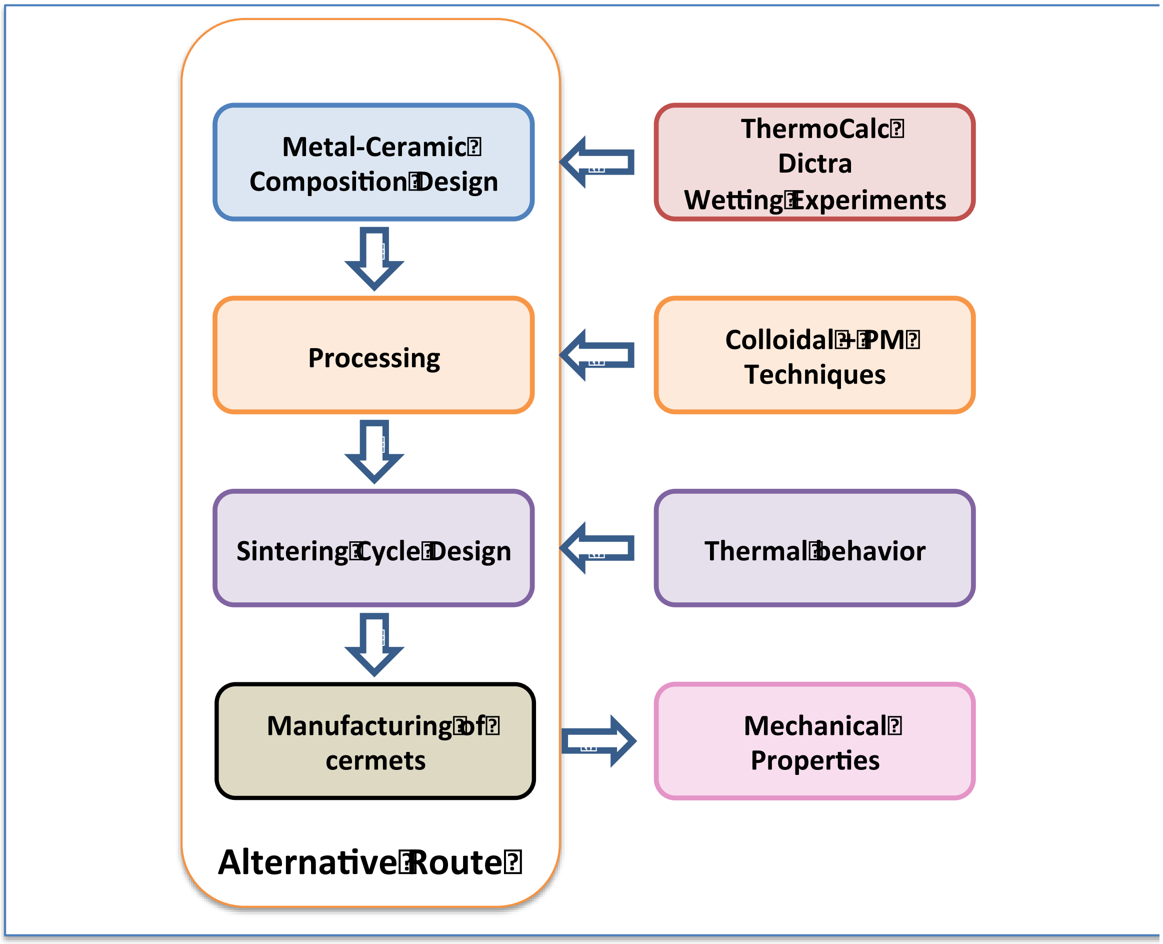

Chapter 3

Summary of Results and Discussion

Results' chapters will summarise and compare the main scientific finds which are carefully described in detail in the appended papers (Table 0). It will also include other relevant results obtained as a part of the experimental work developed to complete and support this whole research work conclusions.

Table 0. Appended Papers

Paper 1	P. Alvaredo, **M. Dios**, B. Ferrari, E. Gordo, Interface study for the design of alternative matrixes in cermets, in: EURO PM2015. Proceeding EURO PM2015, 2015.
Paper 2	**M. Dios**, Z. Gonzalez, P. Alvaredo, R. Bermejo, E. Gordo, B. Ferrari, Novel colloidal approach for the microstructural improvement in Ti(C,N)/FeNi cermets, J. Alloys Compd. 724 (2017) 327–338. doi:10.1016/j.jallcom.2017.07.034.
Paper 3	**M. Dios**, Z. Gonzalez, B. Ferrari, I. Kraleva, R. Bermejo, P. Alvaredo, et al., Influence of the colloidal processing route on the mechanical properties of Ti(C,N)-based cermets, in: 19th Plansee Semin., Reutte, 2017.
Paper 4	**M. Dios**, I. Kraleva, Z. González, P. Alvaredo, B. Ferrari, E. Gordo, R. Bermejo, Mechanical characterization of Ti(C,N)-based cermets fabricated through different colloidal processing routes, J. Alloys Compd. (2017). doi:10.1016/j.jallcom.2017.10.274.
Paper 5	H. Besharatloo, J.J. Roa, **M. Dios**, A. Mateo, B. Ferrari, E. Gordo, et al., Micromechanics of Ti(C,N)-FeNi Composites: Statistical Analysis and Flow Stress Determination for the FeNi Binder, in: Eur. Proceeding Eur., Milan, 2017.
Paper 6	H. Besharatloo, J.J. Roa, **M. Dios**, A. Mateo, B. Ferrari, E. Gordo, et al., Micromechanical Properties of a Ti(C,N)-FeNiC Composite: Statistical Method, in: GEF2017. XXXIV Encuentro Del Grup. Español Fract., Santander, 2017.
Paper 7	**M. Dios**, E.M. Susca, U. Wiesner, E. Gordo, Z. Gonzalez, B. Ferrari, Tailored Ti(C,N)-Ni core-shell nanostructures in aqueous suspension by ELD, Mater. Lett. (n.d.). doi:in Press.
Paper 8	**M. Dios**, Z. Gonzalez, E. Gordo, B. Ferrari, Semiconductor-metal core-shell nanostructures by colloidal heterocoagulation in aqueous medium, 2016. doi:10.1016/j.matlet.2016.05.179.
Paper 9	**M. Dios**, Z. Gonzalez, E. Gordo, B. Ferrari, Chemical precipitation of nickel nanoparticles on Ti(C,N) suspensions focused on cermet processing, Int. J. Refract. Met. Hard Mater. 63 (2017) 2–8. doi:10.1016/j.ijrmhm.2016.08.009.
Paper 10	**M. Dios**, Z. González, E. Gordo, B. Ferrari, Core-shell Ti(C,N)-Ni Structures Fabricated by Chemical Precipitation of Ni-based Nanoparticles on Ti(C,N) Suspensions, EURO PM 2015. Proceeding EURO PM 2015.
Paper 11	**M. Dios**, Z. Gonzalez, C. Romero, E. Gordo, B. Ferrari, Ti(C,N)-Fe/Ni/FeNi Core-Shell Structures for Cermets Processing, in: World PM2016. Proceeding World PM2016, Hamburg, 2016.

The chapter is divided in four sections that will give insights about different topics that have to be considered when new metal-ceramic materials are designed:

1.- Establishing the binder composition as a function of its solubility and wettability on Ti(C,N)
  → Paper 1
2.- Novel colloidal approach for the microstructural improvement in Ti(C,N)-FeNi cermets
  → Papers 2 and 3
3.- Evaluation of the mechanical properties
  → Papers 2 to 6
4.- Alternative approach for the synthesis of metal-ceramic materials
  → Papers 7 to 11

1.- Establishing the binder composition as a function of its solubility and wettability on Ti(C,N)

The aim of this work is to obtain a better knowledge of several ceramic-metal systems through a combination of experimental tests and simulation tools. For this purpose high temperature wetting experiments are performed to observe the evolution of contact angle with time, and to analyses the solubility behavior between metal and ceramic phases; and thermodynamic simulation by ThermoCalc® will allow the understanding of the main interaction mechanisms. These analyses will help us to explain the sintering behavior of the cermets, and to establish a systematic way for searching new compositions.

A thermodynamic study to calculate the phase equilibrium diagram for Ti(C,N)-based cermets with different matrix compositions (Fe, Ni and Fe-15Ni) were performed using the ThermoCalc® software [172]. Calculations are based on the free Gibbs energy minimization code and mass conversion rule, in combination with TCFE7 and TTNI7 databases (Scientific Group Thermodata Europe). To study the wetting behavior of metals on ceramic substrates wetting experiments at 1500 °C and 1550 °C for Ni and Fe respectively, were performed. These experiments were conducted in a tube furnace under Ar atmosphere. The furnace is provided with a camera to record the metal melting and the formation of the liquid metal drop as well as its evolution with time. So, the evolution of the contact angle between the two phases with respect to the residence time and temperature was monitored by the sessile drop method, taking as $t = 0$ the moment at which the melting of the metal sample is started. For these tests, the metallic samples were prepared by a conventional powder metallurgy route (uniaxial pressing and vacuum sintering at 1450 °C for 1 hour) to obtain homogeneous metals and alloys to place onto the ceramic substrates. After wetting experiments, a cross section is made in the system formed by the metal and the ceramic substrate sample to study the interface between the two phases by observation in the Scanning Electron Microscope (SEM).

The pseudobinary phase diagram of Ti(C,N) with respect of Fe and Ni content is shown in Figure 1 and provides the starting point for the design of new binder compositions. As it can be seen, the colored region determine the solubility of Ti(C,N) on liquid Fe and Ni respectively and its dependence with the temperature and composition.

In the Ti(C,N)-Ni pseudobinary phase diagram the increase on the Ti(C,N) solubility on liquid Ni provokes the emergence of a region in which Ni, Ti(C,N) and liquid phase coexist. Moreover, the dissolution of Ti(C,N) results in a decrease of the solidus temperature of Ni. On the other hand, the Ti(C,N)-Fe pseudobinary system shows a narrow region in which Fe, Ti(C,N) and liquid phase coexist and the solidus temperature of Fe remains constant with the presence of Ti(C,N). These diagrams can confirm the differences of Ti(C,N) dissolution in both liquid metals which will be the responsible of their different wetting behavior.

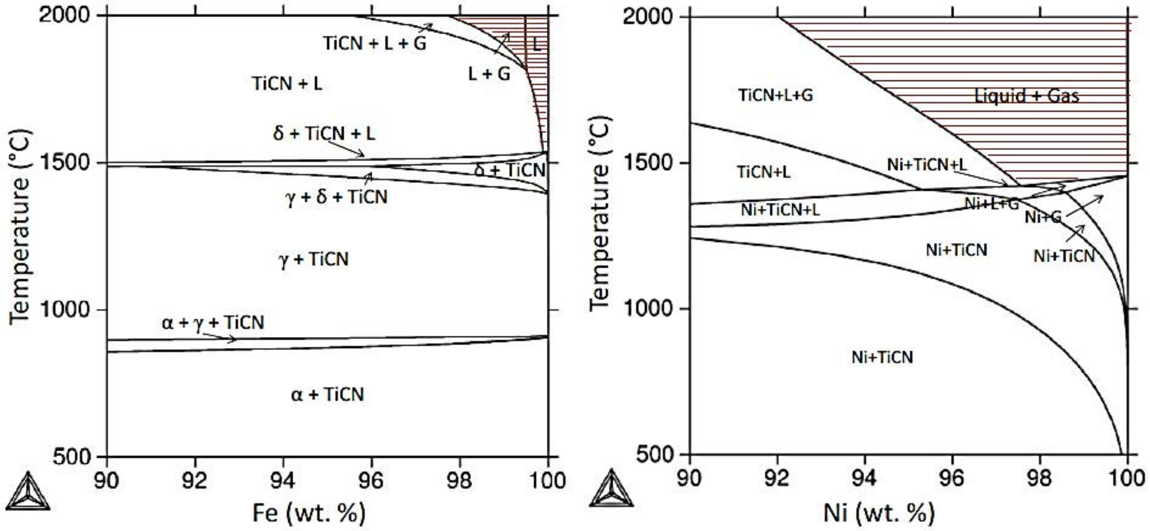

Figure 1. Binary phase diagram of (a) Ti(C,N)-Fe and (b) Ti(C,N)-Ni

In the design of alternative metal binder compositions that generate liquid phases during sintering, not only the *liquidus* and *solidus* temperatures are important, but also the ability of the melted metal to wet the surface of the Ti(C,N) particles. The purpose of these wetting experiments is to simulate conditions similar to those present during sintering, which allows studying the wetting behavior of the metal liquid phase over a ceramic substrate of the same nature as the ceramic particles of the cermet, which were sintered by SPS at 1900 ˚C and a pressure of 70 MPa with heating/cooling rates of 100 ˚C to achieve a relative density of 99.5 %.

Figure 2 shows the evolution of the contact angle of the metallic binders, Fe, Ni and Fe-15Ni, under Ar atmosphere. Fe was selected as the reference system and in agreement with the preliminary studies found, under these conditions is not able to wet the Ti(C,N)-substrate. The contact angle displays a completely different evolution than those of the compositions containing Ni. From the beginning of the melting in the case of Fe sample, the contact angle is higher than 90 ˚ and it remains constant until 550 s of residence time when it decreases sharply down to 60 ˚. Contrarily the contact angle of the liquid Ni and Fe-15Ni over the Ti(C,N) substrate is lower than 90 ˚ (79 ˚ and 71 ˚ respectively) highlighting the better wettability of these metallic phases on Ti(C,N) substrates. In fact, after complete melting, in the case of Ni, there is a slight evolution of the contact angle from 20 ˚ to 10 ˚. In the case of the Fe-15Ni alloy, the contact angle is stabilized in 24 ˚, and no further evolution is detected after the melting process, thus corroborating that the presence of Ni improves the wetting ability of Fe.

Besides, in order to study in deep the nature of the wetting process, the cross section of the samples collected after the wetting experiments were studied. Although it can be assumed that all systems have a dissolutive character (see Figure 1), the dissolution of Ti(C,N) is clearly more pronounced in presence of Ni, corroborating the theoretical information obtained through the previous pseudobinary phase diagrams depicted in Figure 1. The liquid-substrate interface of the Ti(C,N)-Fe system does not show any feature indicating the Ti(C,N) dissolution, behaving as an inert system. However, in the case of samples having Ni in their composition, the infiltration of the binder among the ceramic structure evidences its dissolution leading to the development of a wide interface. The Ni and Fe-15Ni metal binders dissolve the Ti(C,N) substrate and surround the ceramic grains along a thickness higher than 100 μm, while this effect is limited to 10 μm in the case of Fe.

Once the composition is fixed, based on the thermodynamic and wettability studies carried out, and taking into account the literature found in this regard, it is necessary to understand how the C content may affect the selected system for several reasons. Firstly, because there is a preferential dissolution of the carbide contained in the Ti(C,N) with the metallic matrix and therefore it becomes part of the matrix, and secondly to be able to know the effect that an carbon controlled addition would have in the metal matrix from the point of view of liquid phase formation. For that purpose, the pseudobinary phase diagram of the Fe-15Ni binder was plotted using ThermoCalc® considering variations in C content (Figure 3). As it can be observed at the diagram, the addition of C favors the decrease both the solidus and liquidus temperature of FeNi phase.

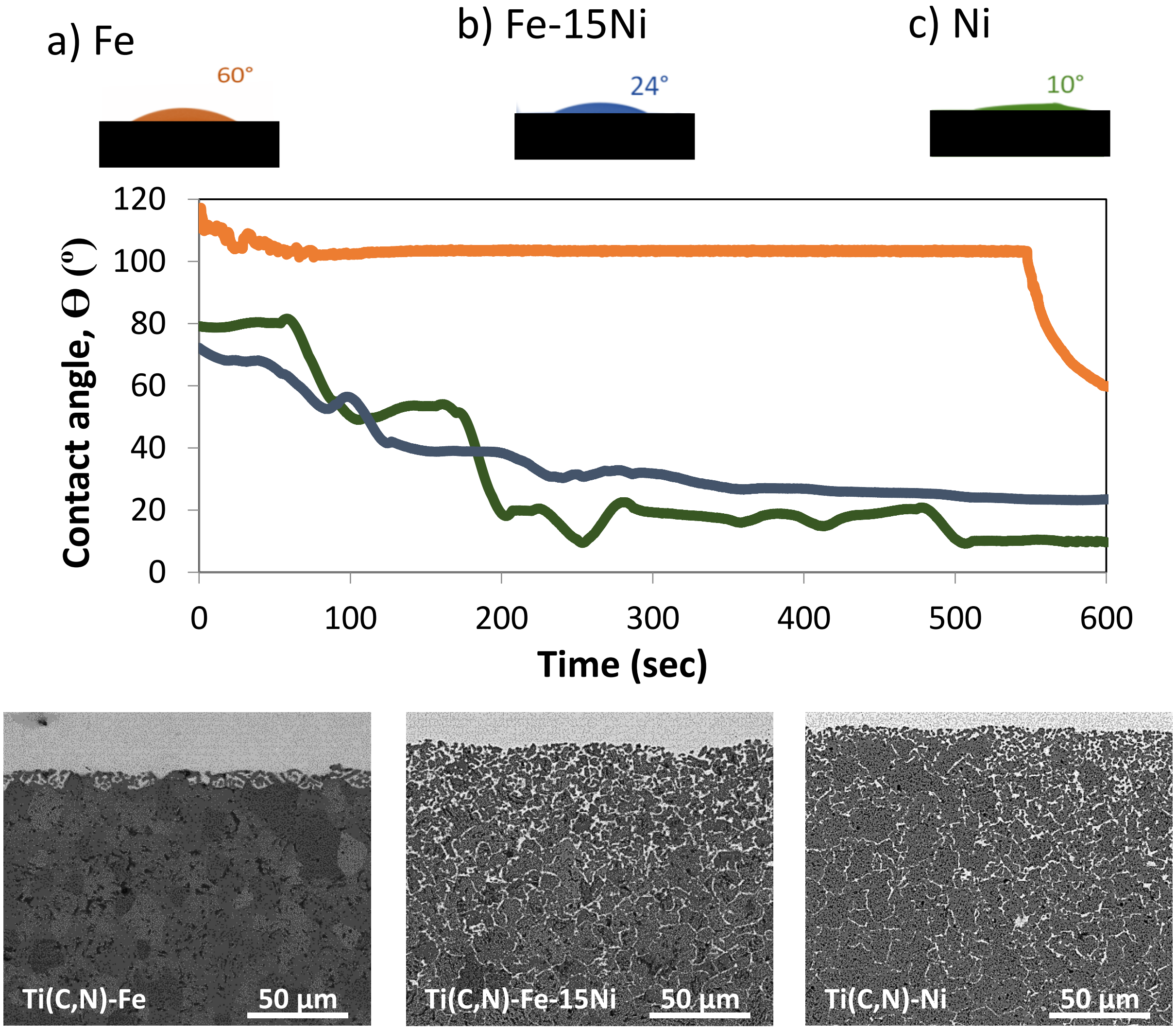

Figure 2. Contact angle, evolution of contact angle with respect to the time and SEM interface between (a) Fe, (b) Ni and (c) Ni on Ti(C,N) substrates

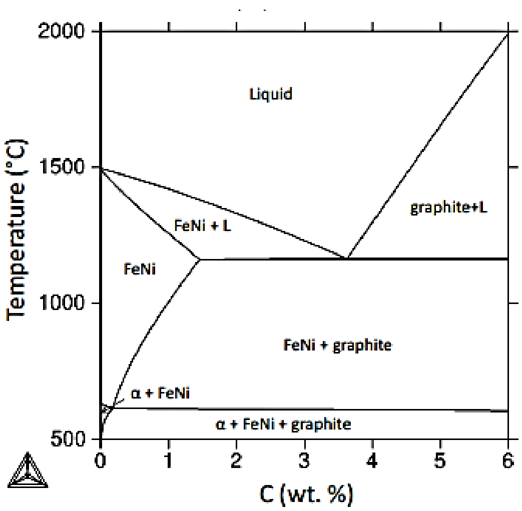

Figure 3. Phase diagram of (Fe-15Ni)-C

The studies performed with the different binder compositions allowed to confirm that the melting process is taking place in the range of temperatures predicted by ThermoCalc®. Besides, wetting experiments depicted the feature of the interaction front between the ceramic reinforcement and the liquid phases that will be formed during sintering.

Summarizing, this research work presents the preliminary results of a detailed and systematic study addressed to understand the liquid phase sintering (LPS) mechanism in Ti(C,N)-based cermets with different binders (Fe, Ni and Fe-15Ni). The aim of this work was to validate a binder formulation based on the ceramic reinforcement wettability, in order to achieve the structure consolidation and densification as well as to tailor the metal/ceramic bonding.

Based on this study, according to previous works and according to the literature, four compositions were selected to be processed, as reported in Table 1. The selected metal matrix composition (85/15 wt. % Fe/Ni) was chosen for offering the optimal hardness/toughness combination [39].

Table 1. Formulation of the suspensions

Composition	Ceramic reinforcement Ti(C,N) vol. %	Metal matrix Fe/Ni vol. %	Composition of metal matrix wt. %		
			Fe	Ni	Carbon*
15FeNi	85	15	85	15	-
15FeNiC	85	15	85	15	+ 0.5
20FeNi	80	20	85	15	-
20FeNiC	80	20	85	15	+ 0.5

* A 0.5 wt. % C was added with respect to the matrix weight [104].
The final composition obtained for this metal matrix was [85.1 wt. % Fe - 13.2 wt. % Ni - 1.7 wt. % C]

The details of experimental procedure, the complete results and discussion is published in: [Paper 1]

2.- Novel colloidal approach for the microstructural improvement in Ti(C,N)-FeNi cermets

Together with the proper selection of the composition and the interaction between phases, the processing method is a key factor that determines the microstructure and properties of bulk pieces. The next section discusses about the synergistic effect of combining colloidal and powder metallurgy techniques for tailoring the microstructure and thus properties of Ti(C,N)-based cermets (see Figure 4).

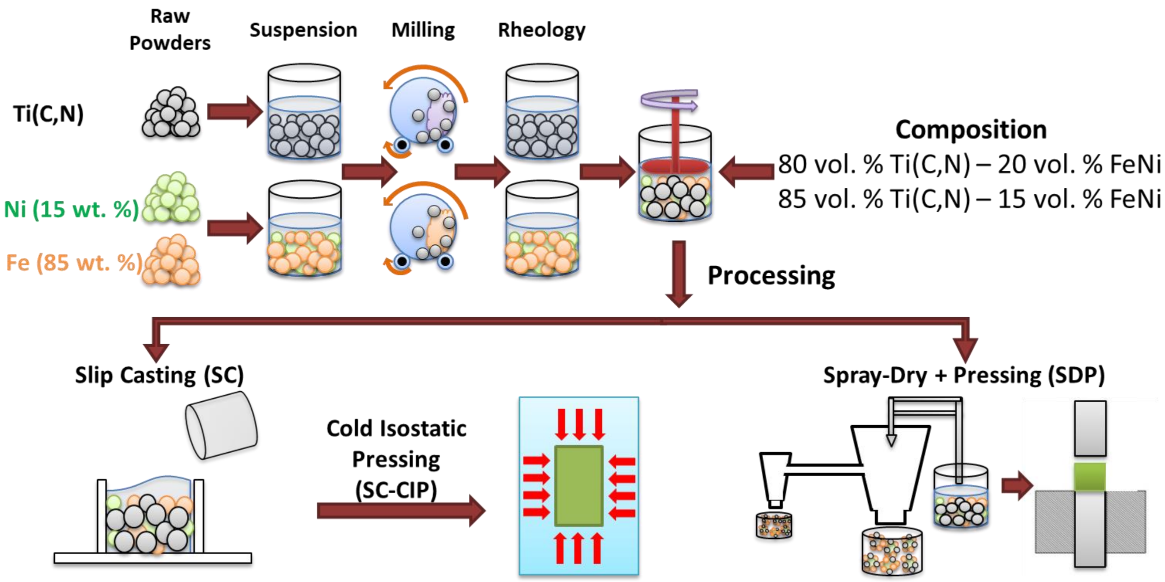

Figure 4. Schematic of the different processing routes including the steps of slurry preparation as well as the employed processes of shaping/compacting.

After an exhaustive characterization of the as-received commercial powders (summarized in Table 2 and Figure 5), the mixture in aqueous media of non-oxide and metal powders in the cermet processing was optimized in terms of rheology.

Table 2. Physical characterization of the as-received powders.

Powder	Size			Density[a] (g/cm^3)	Specific Surface Area[b] (m^2/g)
	D_{v50} (µm)	**D_{BET} (µm)**	**F_{ag}**		
Ti(C,N)	2.1	0.4	5	5.1	3.0
Fe	3.5	1.2	3	7.8	0.6
Ni	1.0	0.2	5	8.9	4.0

[a] ± 0.1 Standard deviation in density measurements.

[b] ± 0.1 Standard deviation in specific surface area measurements.

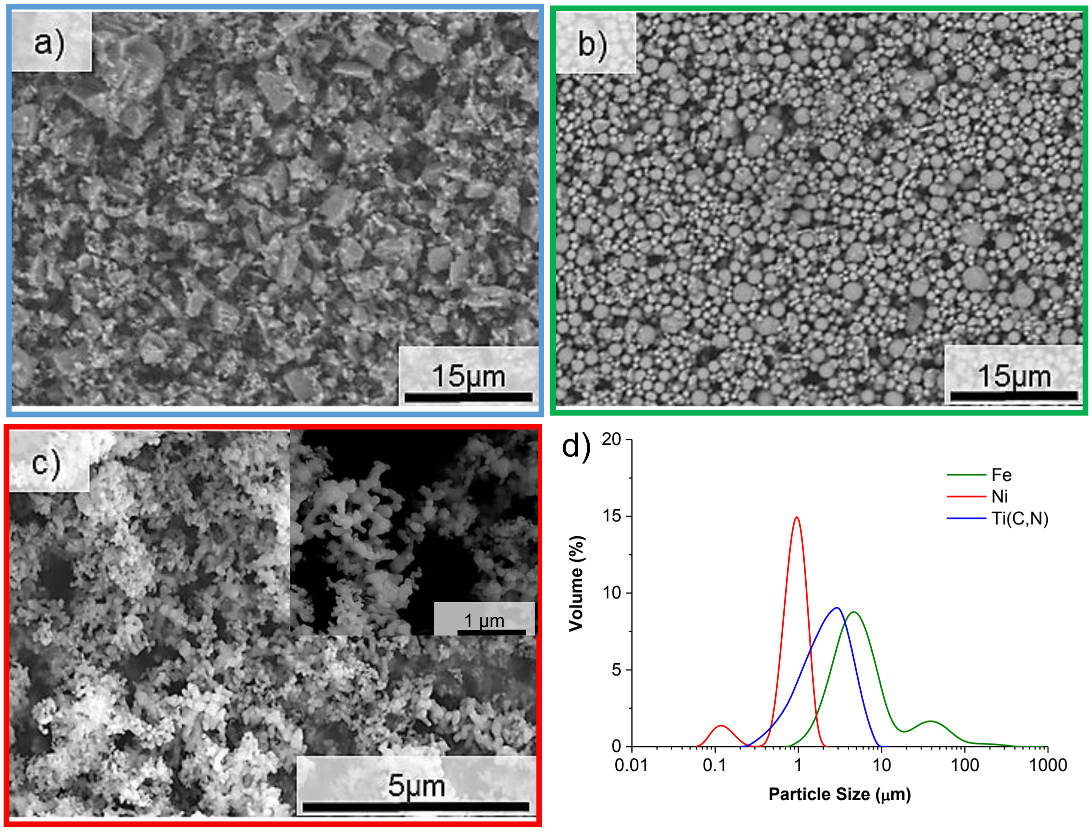

Figure 5. SEM micrographs of (a) Ti(C,N), (b) Fe and (c) Ni as-received commercial powders and (d) particle size distribution of the powders. Inset in Figure 4c shows a detail of Ni powder.

Then dispersion, flux behavior and packing of Ti(C,N), Fe and Fe-15Ni (mixture of Fe and Ni powders in an 85/15 wt./wt. composition) slurries were firstly studied. For that purpose, stable and highly concentrated slurries were optimized in terms of rheology (Figure 6). This is crucial to provide an adequate adjustment of the solid content vs viscosity to the slurries for their subsequent processing by colloidal techniques.

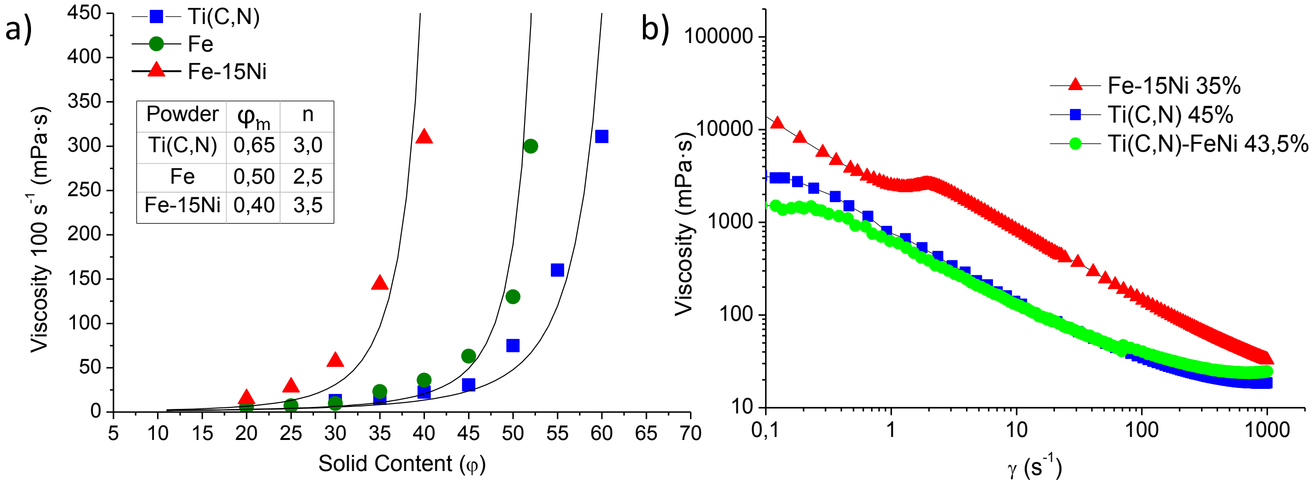

Figure 6. (a) Influence of the solids content on the viscosity for Ti(C,N), Fe and Fe-Ni suspensions. The inset shows the corresponding results obtained for the Krieger-Dougherty adjustment and (b) Flow curves of FeNi 35 vol. %,Ti(C,N) 45 vol. % and resulting Ti(C,N)-FeNi 43.5 vol. %

The results plotted in Figure 6a correspond to a distribution described by the modified Krieger-Dougherty model, which allows predicting the maximum packing fraction (ϕ_m) achieved for dispersed and stabilized slurry of particles.

$$\eta = \left(1-\frac{\varphi}{\varphi_m}\right)^{-[\eta]\varphi_m} \qquad (1)$$

Where η is the relative viscosity at 100 s^{-1} and [η] is the intrinsic viscosity. The exponent is commonly substituted by n which is a value dependent on the shape of the particles. For all systems, the adjusted parameters of the Krieger-Dougherty model are included at the inset in Figure 6a. As it can be observed in the referred figure, the wide particle size distribution of the Ti(C,N) powders, ranging from 0.2 μm to 10 μm allows to reach a higher packing fraction ($\phi_{m,\ Ti(C,N)}$= 0.65) than for the Fe particles and a mixture of Fe/Ni particles ($\phi_{m,\ Fe}$ = 0.50 and $\phi_{m,\ Fe\text{-}15Ni}$= 0.40, respectively). Ti(C,N) and Fe-15Ni slurries with a solid content of 45 vol. % and 35 vol. %, and viscosities for a shear rate of 100 s^{-1} around 30 and 150 mPa·s respectively, are selected in order to compensate the final rheology of the mixture Ti(C,N)/Fe-15Ni.

The flow curves of the Ti(C,N) and Fe-15Ni slurries for the selected solid content was plotted in Figure 6b. Although all slurries exhibit shear thinning behavior, that means, the viscosity decreases under shear strain, the wide particle size distribution of the Ti(C,N) powder provides significantly lower viscosities than the Fe-15Ni mixture for all the shear rates range tested. The flow curve, of the 85 vol. % Ti(C,N) 15 vol. % Fe-15Ni obtained by simple volumetric mixing of the two previous slurries is also plotted in Figure 5b reaching viscosities of mPa·s for a shear rate of 100 s^{-1}, allowing the adequate processing by the colloidal and powder metallurgy techniques described below.

The optimized slurries were prepared for the manufacture of bulk pieces combining colloidal and powder metallurgical techniques (listed in Table 3).

- **Slip Casting (SC).** The conventional colloidal route consisted in the casting of slurries using a porous alumina mold.
- **Slip Casting + Cold Isostatic Pressing (SC-CIP).** Powder metallurgical techniques were implemented in order to evaluate the synergistic effect of the combination of both routes. In this process, the SC green samples were pressed using the cold isostatic pressing process to evaluate the effect of increasing the green density in the final properties of the sintered materials.
- **Spray-Dry + Uniaxial Pressing (SDP).** For the SDP samples, the slurries were spray-dried and the obtained spherical granules (Figure 7) were pressed at 600 MPa in a uniaxial die [107].

Table 3. Identification of samples prepared for each route and composition.

Route	Composition			
	15FeNi	**15FeNiC**	**20FeNi**	**20FeNiC**
SC	*	SC 15FeNiC	---	---
SC-CIP	SC-CIP 15FeNi	SC-CIP 15FeNiC	---	---
SDP	SDP 15FeNi	SDP 15FeNiC	SDP 20FeNi	SDP 20FeNiC

***SC-15FeNi samples break during sintering.**

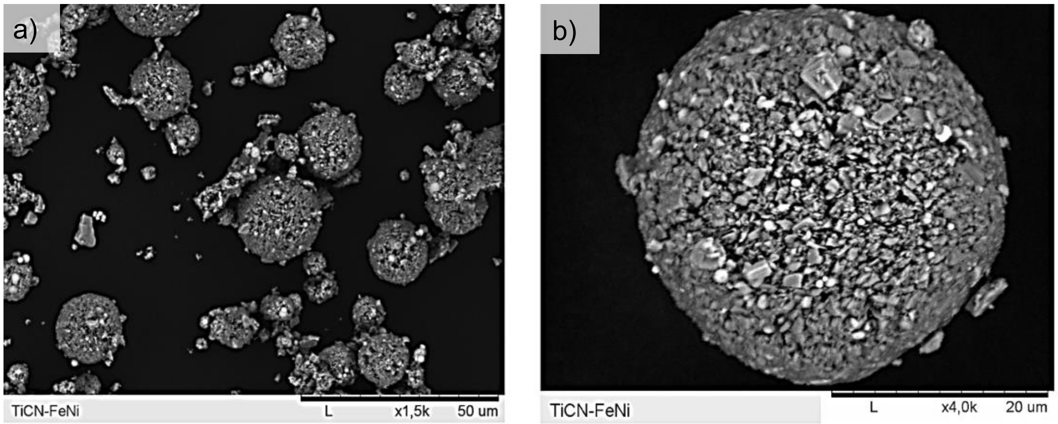

Figure 7. SEM micrographs of the 15FeNi granules obtained by spray-drying

To optimize the cycle of sintering, thermal analysis and characterization of bulk SDP 15FeNi specimens were carried out in terms of Differential Thermal Analyses and Dilatometry using Ar. Through DTA measurements it will be possible to identify the events that occur during the heating (and cooling) of the sample such as phase changes, recrystallization, volatile removal, etc. On the other hand, from the dilatometric measurements, it will be possible to identify the temperature at which the contraction begins (and therefore the sintering) and even determine the speed at which it occurs. Pre-sintered samples at 800 °C in vacuum and reducing atmosphere ($N_2/10\%H_2$) were tested.

As it can be observed in the DTA measurements in Figure 8a, both samples show similar trends. A double tiny endothermic peak between room temperature and approximately 300 °C associated to superficially physisorbed water losses and due to outgassing processes, is present. From 350 °C to 1100 °C a wide endothermic valleys appears which could be associated to the diffusion processes. Finally, both heating curves show endothermic valleys at 1451 °C and 1466 ˚C for the vacuum and reducing sintering atmosphere respectively, which correspond to the beginning of the formation of a liquid phase (Figure 1). The temperature at which liquid phase appears in the reducing atmosphere is shifted 15 °C to the right, until 1466 °C, consequently metal melting takes place at a higher temperature.

Figure 8b and c shows the dilatometry results of the SDP-15FeNi samples pre-sintered in vacuum and under reducing atmosphere respectively. It can be observed that the characteristic shrinkage of the samples is different depending on the atmosphere used for the pre-sintering step. In the case of the samples pre-sintered in vacuum, a slight increase in thermal expansion was observed up to ~775 °C. Beyond this temperature the sample started to shrink, with three different slopes highlighting diverse thermal phenomena. First, the specimen shrinks at a relatively slow rate as the temperature increases, exhibiting a minimum in the thermal expansion curve at ~950 °C. This effect may be ascribed to the allotropic transformation of iron α (BCC) → γ (FCC) boosted by the gamma effect of nickel. Further shrinkage has a sharply rate, exhibiting a minimum in the curve at 1250 °C. This could be associated with solid state reactions during the thermal rearrangement of the metal powder particles [173] and the formation of the FeNi alloy. Finally a later inflexion point can be observed around 1440 °C, which could be related to the early liquid phase diffusion process of the metal phase [106]. The liquid phase formation of FeNi evolves from 1498 °C (melting point) to 1478 °C, probably due to the dissolution of Ti(C,N) and the diffusion of carbon to the matrix that reduces its melting temperature (see Figure 3).

In the case of samples pre-sintered in a (N_2/10%H^2) reducing atmosphere a thermal expansion up to 1250 °C is observed, followed by a continuous shrinkage up to 1450 °C. The absence of a minimum in thermal expansion curve indicates that maximum sintering has not yet been achieved at 1450 °C. This effect could be attributed to the higher oxidation state of the sample pre-sintered under reducing atmosphere, as the event corresponding to the reduction of oxides observed in the former case is not observed.

With the intention of finding out the reason for this displacement, XRD (Figure 8d) and oxygen content analyses were carried out to the green and pre-sintered samples. XRD analysis evidence the presence of rutile (TiO_2) in the sample pre-sintered in reducing atmosphere. Besides, the oxygen content of these samples is higher (1.69 wt. %) than samples pre-sintered in vacuum (0.82 wt. %). Unexpectedly, the reduction of the oxides on the particles surface was more activated in vacuum that under reducing atmosphere. This can be due to the presence of N_2 in the atmosphere during the pre-sintering process of these composites. The more the nitrogen content in the hard phase particles, the higher is the temperature of the CO evolution. It can be understood considering the fact that the richer the hard phase is in carbon, the more readily the powder particles are reduced, – vice versa – the higher the nitrogen content is, the more sluggish the reduction reaction is to form CO [41,174]. Consequently, it can be concluded that the sintering under vacuum atmosphere was activated due to the lower oxygen content in the surface of the particles that leaves a higher free area of interaction between them.

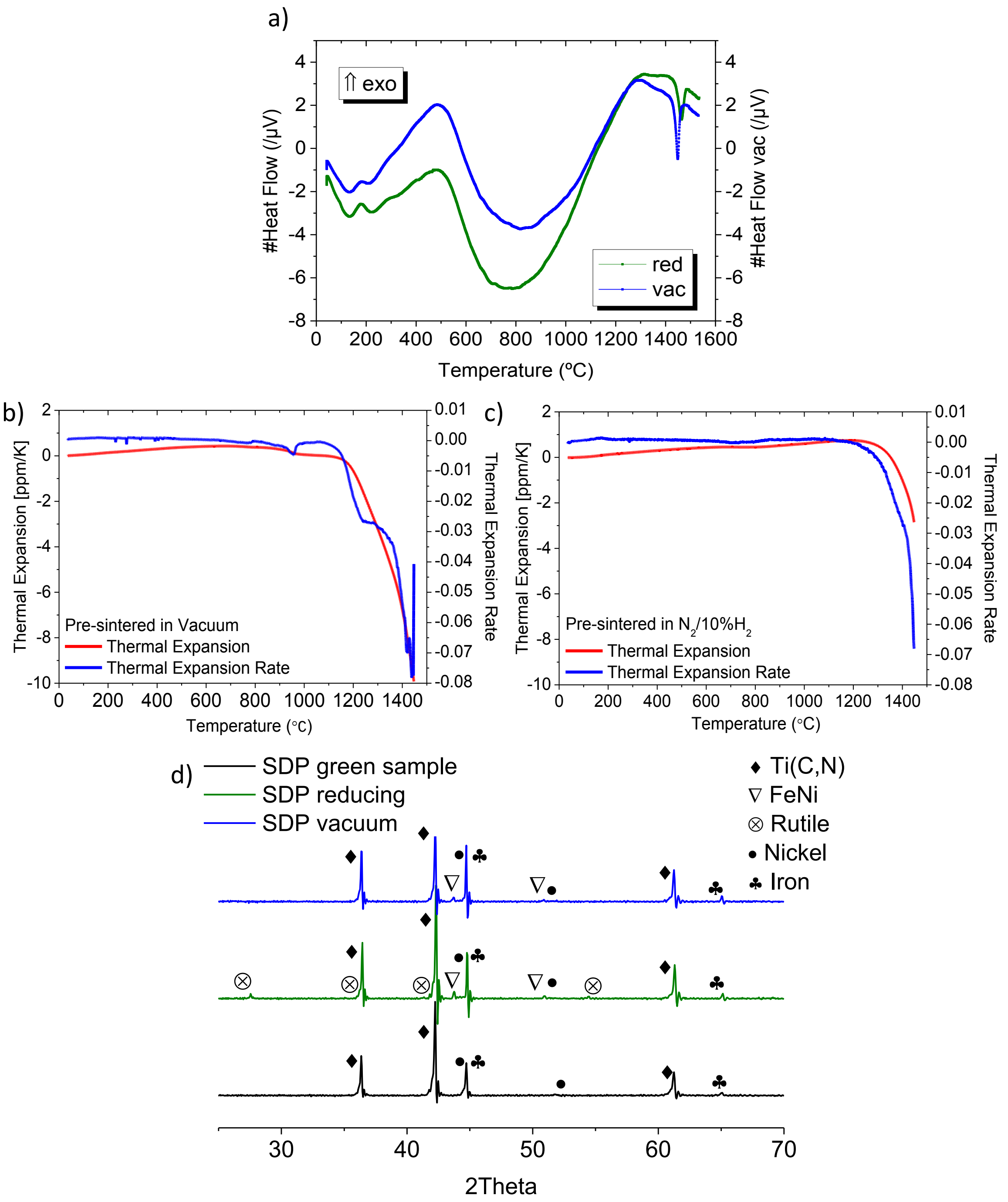

Figure 8. (a) DTA analyses for samples pre-sintered under vacuum and reducing atmosphere. Thermal expansion (Dl/l) and thermal expansion rate (Dl/Dt) versus temperature for samples pre-sintered under (b) vacuum and (c) N_2/10%H_2 atmosphere. (d) X-Ray diffractograms recorded for green and pre-sintered (in vacuum and reducing atmosphere) of SDP 15FeNi samples.

Based upon these findings and in order to study the effect of sintering time on the densification behavior of the materials, sintering of the green samples were performed under vacuum (10^{-5} mbar) at 1450 °C for different times (60, 120 and 300 min) and constant heating/cooling rate of 5°C/min.

Table 4 summarizes a complete physico-chemical characterization of the sintered specimens. Samples sintered during 60 min reached densities of 96.3% of the theoretical. Therefore this sintering time is not enough to get a full dense material. Figure 9 shows a micrograph of a sample, where two phases can be clearly identified in the cermet: the bright contrast phase corresponds to the FeNi matrix, whereas the darker phase corresponds to the ceramic Ti(C,N) phase. During liquid phase sintering the metal phase surrounds the Ti(C,N) particles, but the ceramic phase is not completely sintered. By contrast, sintering times of 120 min lead to almost full density (~99 %), as can also be evidenced in Figure 9. In this case, after sintering, Ti(C,N) particles were perfectly embedded in the metal matrix and only small residual porosity can be observed in triple points. Interestingly, longer sintering times of 300 min do not result in higher densities (94.4 % of the theoretical density), which can be related with an evident deficiency of metal phase in the microstructure, as can be observed in Figure 9. These results evidence a “sintering time threshold”, above which the densification of this complex composite decreases. This phenomenon may be explained by the sublimation of the metal phase (vapour pressure of Ni ten times higher than Co) [175], which increases with increasing temperature and vacuum during sintering, evidenced by the significant mass loss, Δm, of 21.8 %, as reported in Table 4, together with the relatively high dimensional change; the latter cannot be ascribed only to the sintering shrinkage taking into account density values in Table 4 and the microstructure in Figure 9 but also to the sublimation of the metal phase that has occurred.

Based upon such counterbalance effects, a compromise between densification and mass loss must be attained in order to achieve full density materials with the desired composition. This balance was found in samples with 120 min of sintering time, where the highest density with moderate mass loss was measured (see Table 4). The dimensional variation of the samples followed the same trend as the mass variation. It is worth pointing out that the oxygen content of the different sintered samples was kept constant at around 0.2 wt. %.

Finally, in order to verify the results obtained, XRD characterization of the three samples were carried out. Figure 9 shows the XRD patterns of the samples sintered for 60 min, 120 min and 300 min, where the peaks associated with the two main phases are identified: Ti(C,N) phase and the main peak of the cubic crystalline metallic matrix FeNi phase (also magnified at the inset). Although the presence of FeNi is evidenced in all samples, variations in the reinforcement/matrix ratios can be found depending on the sintering time. Taking into account that the crystallization of the Ti(C,N) grains will cause an increase in the intensity of their peaks as the sintering time increases, the peaks of the minority phase, i.e. the metal phase, will be increasingly masked in the pattern. Moreover, the inset in Figure 9 shows a decrease of the intensity of the corresponding FeNi peak with the sintering time, thus reinforcing the hypothesis of the sublimating effect of Ni and Fe discussed above.

Table 4. Characterization of SDP 15FeNi samples for a sintering cycle at 800ºC for 30 min and 1450ºC for different times under vacuum.

Sintering Time [min]	Density [% th]			Porosity* [%]	O_2 wt. %	Dimensional Variation, Δl [%]	Mass Loss, Δm [%]
	ρ^*_{green}	ρ^{**}_{He}	$\rho^{**}_{Arq.}$				
60	68.80	96.3	95.1	P_{close}=3.70 P_{open}= 1.23	0.23 ± 0.04	-11.9 ± 0.6	-3.3 ± 0.2
120		98.9	98.8	P_{close}=1.14 P_{open}=0.01	0.21 ± 0.05	-14.6 ± 0.4	-8.8 ± 0.1
300		94.4	93.7	P_{close}=5.57 P_{open}=0.71	0.27 ± 0.06	-17.3 ± 0.1	-21.8 ± 0.3

* 0.1 % Standard deviation in green density measurements.

** 0.01% Standard deviation in sintered density measurements.

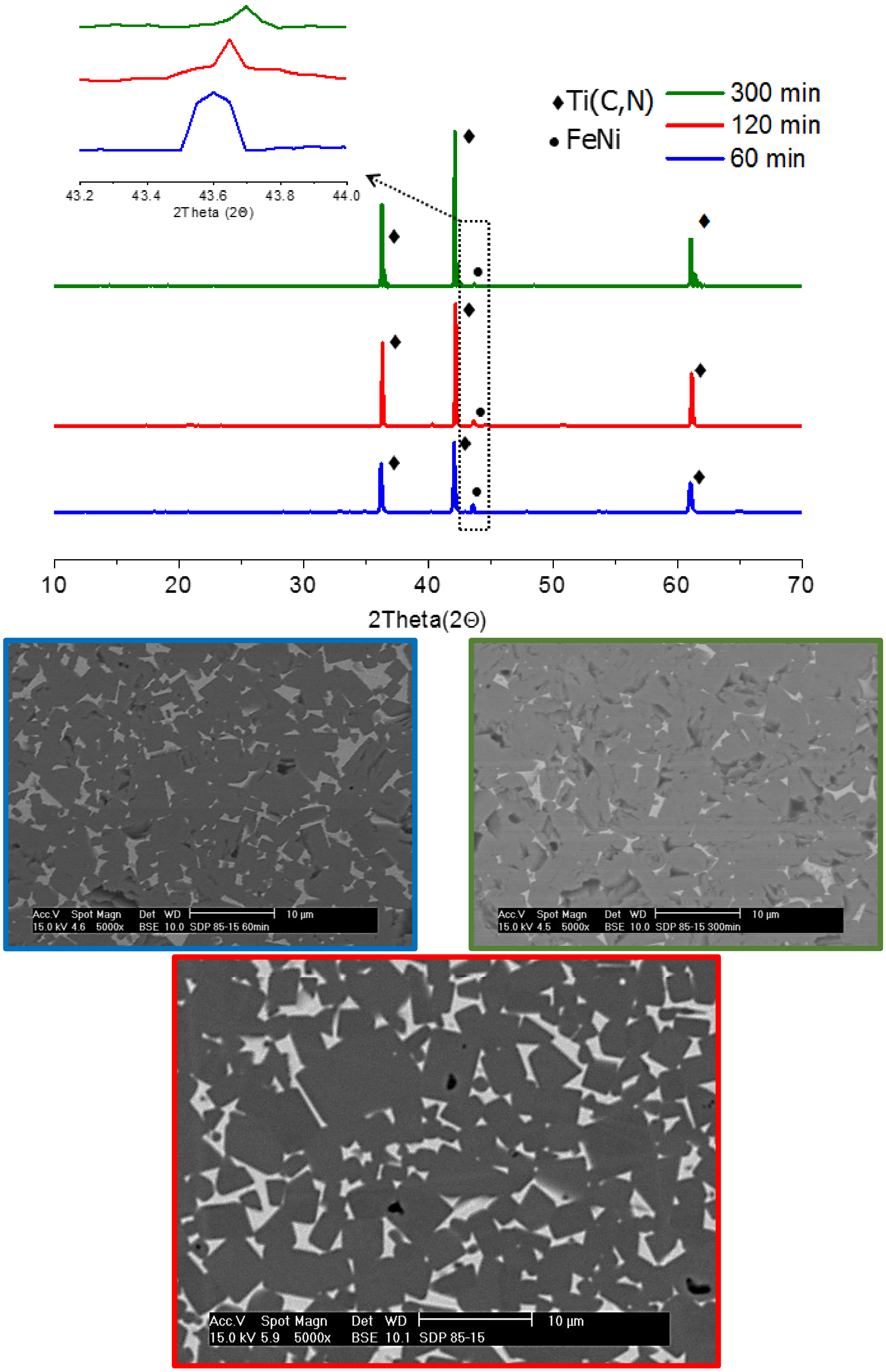

Figure 9. X-Ray diffractograms recorded on the polished surface of SDP 15FeNi samples sintered during different holding times and their corresponding SEM microrgaphs.

Thus, the sintering cycle was optimized to control the cermet composition, reducing the N_2 lability, the final O_2 content (≤ 0.2 to wt. %) and the Ni and Fe sublimation. In this sense, a sintering time as short as 120 min at 1450 ˚C in vacuum with a 30 min dwell at 800 ˚C was adjusted, to provide equilibrium between densification and composition matching the initially designed formulation.

After determining the optimal sintering conditions (temperature, time and atmosphere), all green samples labelled in Table 3 were sintered at 1450 ˚C for 120 min in vacuum with a 30 min dwell at 800 ˚C. A complete physical and microstructural characterization of the green and sintered samples were performed in order to assess the effect of the processing route, the ceramic and metal fractions as well as the C addition on the prospective mechanical behavior of the cermets investigated.

The highest values of green density are obtained for SDP samples, as expected, as they are produced by pressing of high compressibility granules produced by spray-dry. On the other hand, cold isostatic pressing (CIP) increases the green density of SC samples in about 15 %. Regarding the composition effect, increasing the amount of hard phase from 80 vol. % to 85 vol. % decreases the green density due to the higher hardness and stiffness of the ceramic powder during pressing.

Figure 10 shows the SEM images taken in BSE mode, corresponding to the different cermet samples. All micrographs evidence the presence of the same phases defined previously: the brighter phase is the FeNi matrix and the darker one corresponds to the ceramic phase, Ti(C,N). In all cases Ti(C,N) particles are surrounded by the metal matrix phase, which gives to the whole piece a metallic appearance despite the high ceramic content. Although all microstructures exhibit a high dispersion of both phases, samples obtained through SDP show the most homogeneous dispersion of phases and lowest porosity as it can be observed in Table 5. This may be due to the fact that the atomization of the slurry, through which granules are obtained, offers the possibility of pre-designing the final composite in the granules helping to prevent further agglomeration of Ti(C,N) reinforcement particles. This can also avoid metal pools like those observed in SC samples, which may formed during casting in SC and then in SC-CIP samples.

On the other hand, differences in composition between the 15FeNi (Figure 10d and e) and 20FeNi (Figure 10f and g) samples are easily evidenced by observing the higher amount of the ceramic phase at the microstructure of 15FeNi; these data were also confirmed by results of the image analysis (Table 5). Finally, porosity values also evidence that the compositions formulated with C exhibit slightly lower densities in all cases.

Table 5. Density, porosity and ceramic/metal balance of sintered materials.

Sample	Density [% th]				Porosity [%]			Ceramic/metal balance (Porosity) [%]***
	ρ_{th}	ρ^{*}_{green}	ρ^{**}_{He}	ρ^{**}_{geo}	P_{Tot}	P_{Close}	P_{Open}	
SC 15FeNiC	5.53	57.3	93.10	92.20	7.80	6.90	0.80	72.3/21.0 (6.7)
SC-CIP 15FeNi	5.53	66.7	97.66	97.25	2.75	2.44	0.31	81.3/15.9 (2.8)
SC-CIP 15FeNiC	5.53	66.3	97.32	96.44	3.66	2.68	0.98	79.5/16.5 (4.0)
SDP 15FeNi	5.53	68.8	98.86	98.85	1.15	1.14	0.01	83.6/15.8 (0.6)
SDP 15FeNiC	5.53	68.3	98.40	98.19	1.81	1.60	0.21	83.4/15.0 (1.6)
SDP 20FeNi	5.67	69.6	99.72	99.56	0.44	0.28	0.16	81.2/18.6 (0.2)
SDP 20FeNiC	5.67	66.9	99.50	99.01	0.99	0.50	0.49	79.8/19.2 (1.0)

* 0.1 % Standard deviation in green density measurements.
** 0.01% Standard deviation in sintered density measurements
*** Data obtained from image analysis using ImageJ SW

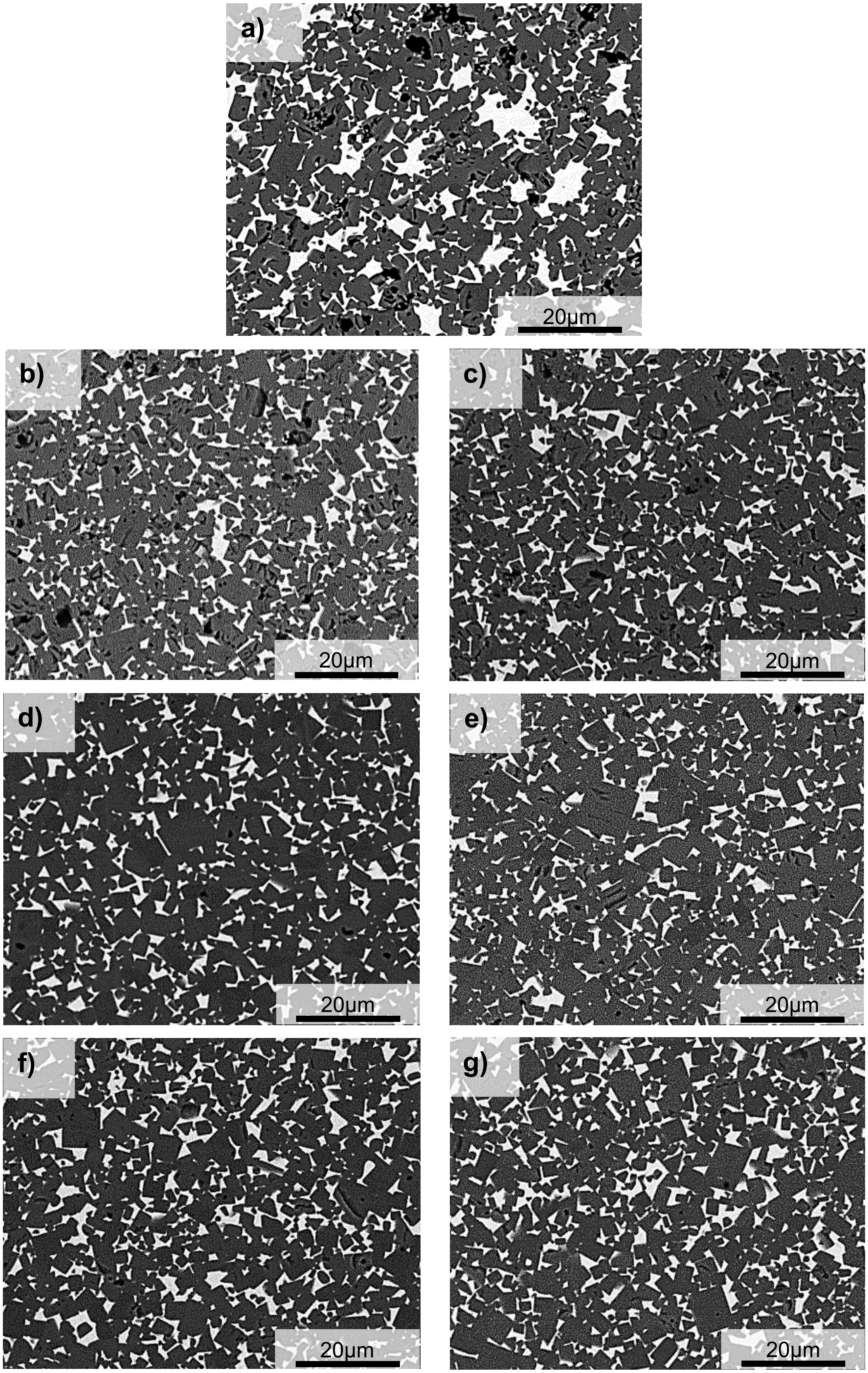

Figure 10. SEM micrograph of Ti(C,N)-based cermets fabricated (a) SC 15FeNiC, (b) SC-CIP 15FeNi, (c) SC-CIP 15FeNiC, (d) SDP 15FeNi, (e) SDP 15FeNiC, (f) SDP 20FeNi and (g) SDP 20FeNiC

Summarizing, among the explored shaping methods, SDP cermets reach densities of 99.9 %. The spray-dry of stable aqueous slurries with a high solid content yield solid and spherical composites granules, where the metal and the ceramic particles are homogeneously distributed. Those granules exhibit a high compressibility enabling their processing by conventional powder metallurgy (uniaxial pressing and vacuum sintering). The high dispersion of phases, in the slurry replicates in the granules, leading to highly dense, homogeneous and fine microstructures after shaping and sintering.

The details of experimental procedure, the complete results and discussion is published in: [Paper 2 and 3]

3.- Evaluation of the mechanical properties

This section contains information about the effect of the processing route, as well as the effect of the metal binder and carbon content on the hardness, the strength and fracture toughness on the Ti(C,N)-based cermets processed. The tests used for determining mechanical properties were: (1) Vickers hardness of sintered samples was measured indenter using different loading conditions. (2) ball-on-three-balls (B3B) method on disc-shaped specimens to measure biaxial strength. (3) four-point-bending (4PB) in Single Edge V-Notched Beam (SEVNB) specimens in order to determine the fracture resistance. Finally, microstructural and fractographic analyses were performed on selected specimens to interpret the experimental results.

Hardness measurements

A Vickers hardness (HV) analysis was carried out for the sintered samples as a function of indentation load (HV5, HV10, HV20 and HV30). Table 6 represents the average hardness along with the standard deviation of at least 5 measurements performed on each sample. The total porosity P_{Tot} of the different cermets is also collected in Table 6 for comparative purposes. Figure 11 shows a series of HV30 representative imprints carried out on all samples.

Table 6. Vickers Hardness measurements with different loads: HV5, HV10, HV20 and HV30. The total porosity (P_{Tot}) is also shown for comparative purposes.

Material	P_{Tot} [%]	HV5	HV10	HV20	HV30
SC 15FeNiC	7.80	1039 ± 100	946 ± 62	958 ± 57	925 ± 37
SC-CIP 15FeNi	2.75	1198 ± 30	1111 ± 57	1127 ± 42	1137 ± 50
SC-CIP 15FeNiC	3.66	1326 ± 47	1227 ± 36	1219 ± 41	1219 ± 22
SDP 15FeNi	1.15	1313 ± 18	1281 ± 14	1258 ± 17	1246 ± 18
SDP 15FeNiC	1.81	1383 ± 59	1330 ± 13	1309 ± 10	1301 ± 7
SDP 20FeNi	0.44	1179 ± 28	1085 ± 69	1144 ± 13	1120 ± 26
SDP 20FeNiC	0.99	1267 ± 27	1207 ± 27	1198 ± 9	1185 ± 7

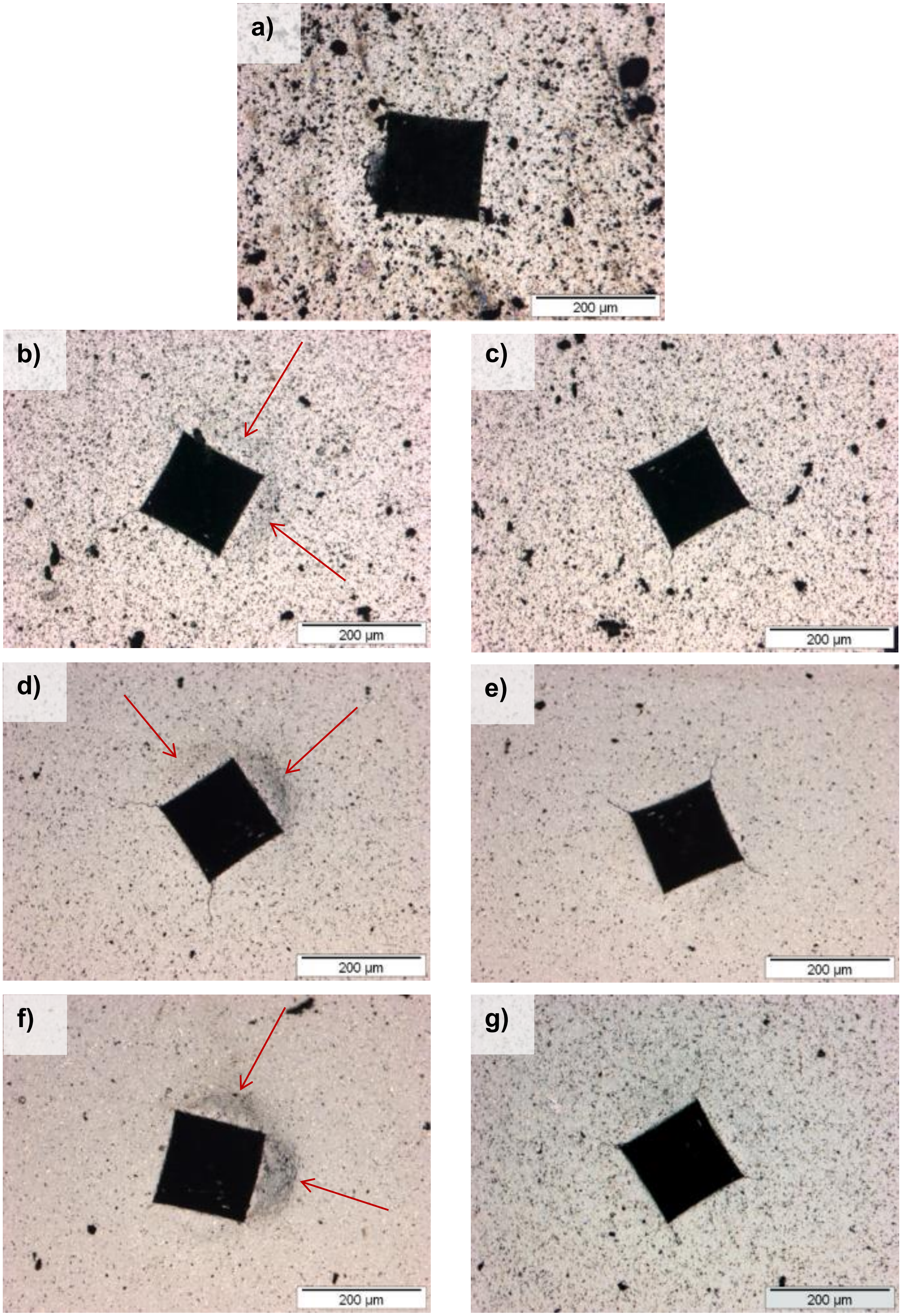

Figure 11. Series of HV30 imprints corresponding to the different Ti(C,N)-based cermets samples (a) SC 15FeNiC, (b) SC-CIP 15FeNi, (c) SC-CIP 15FeNiC, (d) SDP 15FeNi, (e) SDP 15FeNiC, (f) SDP 20FeNi and (g) SDP 20FeNiC

In our analysis, based on the porosity values and the Vickers imprints in the micrographs of Figure 11, a direct correlation between porosity and hardness can be appreciated. For a given composition (e.g. 15FeNiC) bulk pieces processed by SDP show a lower porosity (1.81 %) and higher hardness values (1301 HV30) than samples obtained by the other two processing methods, SC (7.80 %, 925 HV30) and SC-CIP (3.66 %, 1219 HV30). The same trend is observed for the 15FeNi samples (without C addition). The effect of the metal fraction in the composition can be appreciated between 15FeNi and 20FeNi samples processed by the SDP route. Although slightly less porosity was measured in the 20FeNi samples, a significant reduction in hardness was obtained compared to 15FeNi samples (e.g. 1120 vs. 1246 for HV30) due to the higher metal content. In fact, a similar trend can be observed for samples containing C, comparing 15FeNiC with 20FeNiC (e.g. 1301 vs. 1185 for HV30).

Regarding the effect of C addition, the increment of hardness, 15FeNi with 15FeNiC (i.e. 1246 vs. 1301 for HV30) and 20FeNi with 20FeNiC (i.e. 1120 vs. 1185 for HV30), has been also reported in literature for Ti(C,N) with Fe based binders, although the effect may be more relevant when higher amount of metal binder is present [176]. The reason of this increment might be related to different factors that are currently under investigation, which derive from the decrease of the liquidus temperature of the metallic matrix with the C addition: (1) a different rearrangement of Ti(C,N) particles that can induce changes in the carbonitrides contiguity; (2) changes of the sintering activation leading to higher dissolution rates of the Ti(C,N) ceramic structure with the metal matrix; (3) changes in the stoichiometry of carbonitrides; or even (4) variations in the diffusion rate of some Ni from the metal binder.

Measured hardness values are consistent with those found in the literature related to the Ti(C,N) based cermets of a similar composition (reinforcement phase > 80 vol. %) prepared by other techniques and/or using other binders. Some of them are as TIC-Fe materials prepared by SPS [177], TiC-Ni prepared by uniaxial pressing with and without the addition of WC [56,76], Ti(C,N)-Ni mixed with different carbides [42] or (Ti,W)(C,N)-Ni prepared by high energy milling and adding WC [58].

Strength distribution

The tensile strength is associated with the presence of flaws, which are distributed within the specimens or in their surface. The strength of a specimen is determined by the most critical defect (which is, in general, the largest one in the most highly stressed location). Therefore the strength has to be described by a distribution function, which reflects the size distribution of flaws in the specimens. The scatter of strength in each sample can be related to the different size of the critical flaw causing the failure. The Weibull parameters σ_0 (characteristic strength) and m (Weibull modulus) and their corresponding 90 % confidence interval of each sample were calculated according to EN-843-5 standard [178] and are listed in Table 7.

Table 7. Characteristic strength, σ_0, and Weibull modulus, *m*, for the different cermet samples, along with the 90% confidence intervals. The porosity determined for the specimens (in vol. %) is also given for comparison.

Sample	Porosity [%]	Charact. Strength σ_0 [MPa]	Weibull modulus *m*
SC 15FeNiC	7.80	**1088** [1059 – 1118]	**19** [12 – 24]
SC-CIP 15FeNi	2.75	**1374** [1314 – 1437]	**12** [8 – 17]
SC-CIP 15FeNiC	3.66	**1375** [1321 –1432]	**13** [8 – 16]
SDP 15FeNi	1.15	**1529** [1497 – 1562]	**17** [12 – 21]
SDP 15FeNiC	1.81	**1528** [1495 – 1562]	**16** [12– 20]
SDP 20FeNi	0.44	**1529** [1493 – 1566]	**15** [11 – 19]
SDP 20FeNiC	0.99	**1867** [1832 – 1903]	**19** [14 – 23]

Figure 12a shows the results of the B3B tests conducted in the different disc-shaped specimens of Ti(C,N)-based cermets [179–181]. The characteristic biaxial strength has been plotted versus the porosity (in %) for all materials tested in an attempt to analyze the correlation between these two parameters in Figure 12b. The main observation is that the lower the porosity, the higher the strength, as it was expected. As a consequence, the materials processed by SDP show the highest values of strength. It is worth pointing out the significant difference in strength between 20FeNiC and 20FeNi. Nevertheless, such a difference cannot be observed between 15FeNiC and 15FeNi cermets (Tabl 7). Figure 12c shows a Weibull diagram, where the probability of failure, P_f, is plotted versus the failure stress, σ_f, to compare the strength distribution of samples fabricated by different processing routes for a given composition (15FeNiC). Bulk pieces processed by SC showed higher porosity values (7.8

%) and lower strength values (~1090 MPa) than samples obtained by the other processing methods, SC-CIP (3.6 %, ~1380 MPa) and SDP (1.8 %, ~1530 MPa). The same trend was observed for the 15FeNi specimens (without C addition). Figure 12d shows a Weibull diagram of the strength distribution of the two 20FeNi samples, with and without carbon addition. It is interesting pointing out that only in the case of 20FeNi samples a clear difference can be appreciated in the strength, the carbon addition improving the mechanical behavior. For the case of 15FeNi, no difference could be observed (see Table 7).

As it can be seen in the reported bibliography, the values of transverse rupture strength of sintered Ti(C,N) cermets depends strongly of the binder phase used and its volume fraction, the addition of secondary phases as well as the carbon addition. However, the measured σ_0 and m values are comparable to the formulation reported in the literature for the Ti(C,N) based cermets, or a similar composition, processed by other techniques and/or using other binders [63–65,70,105,176].

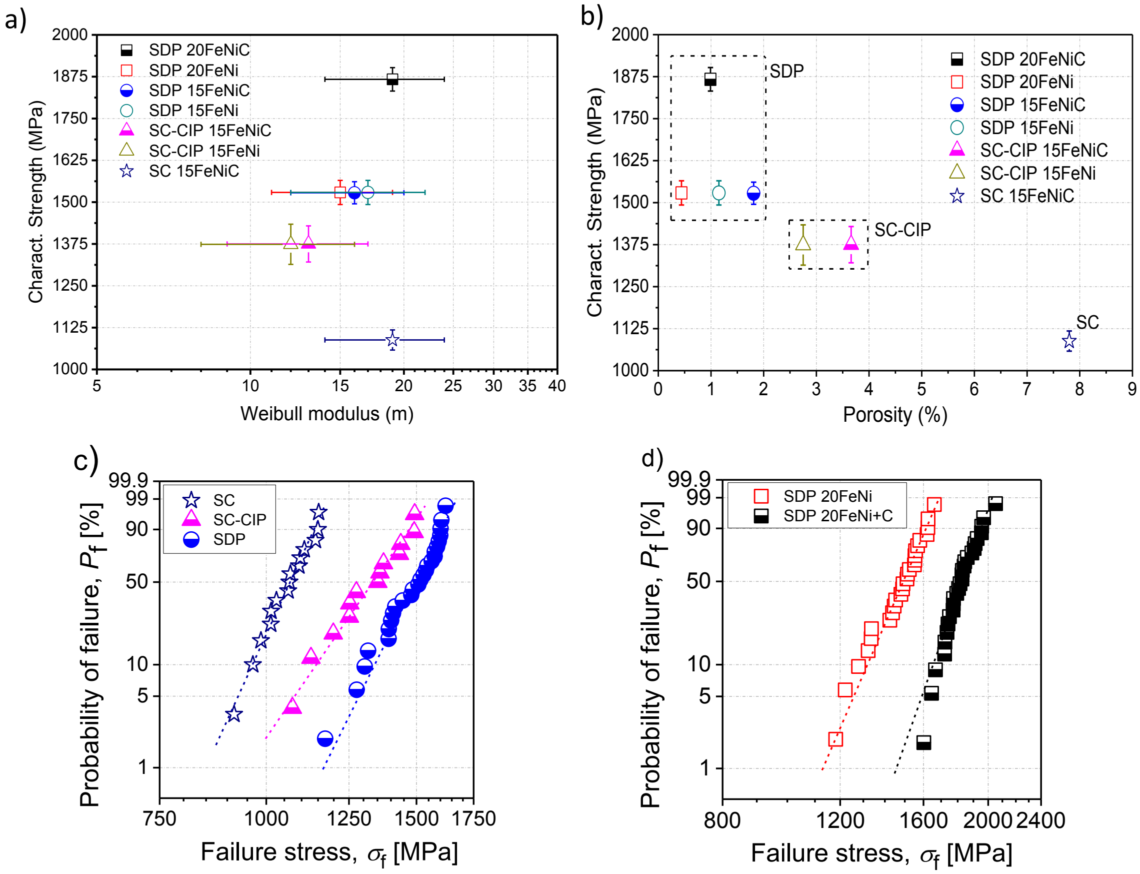

Figure 12. Biaxial characteristic strength versus (a) Weibull modulus (b) porosity. Weibull diagrams representing strength distributions comparing (c) the processing route for the composition 15FeNiC, and (d) the effect of carbon addition for the SDP 20FeNi specimens.

Failure analyses on B3B samples

In order to identify the size, location and type of critical flaw, a fractographic analysis was performed in selected specimens corresponding to each cermet composition. The fracture origin is located in the center of the disc. Typical volume flaws, which may act as fracture origins, are pores, impurity inclusions, lakes of binder, agglomerates, etc. In order to identify the type of critical defect, a fractographic analysis was performed in selected samples. Figures 13 show representative critical flaws corresponding to the different cermet samples tested under B3B. The top side in the figures correspond to the tensile side. An inset of the broken sample is also given to illustrate the macroscopic fracture. The broken lines indicate the fracture direction.

In most of the samples investigated in this work, the fracture origin resulted to be a large pore in the surface and/or subsurface of our materials, which can be modelled by a spherical cavity with a diameter of about 25 µm. Macroscopic brittle fracture was controlled by the extension of small flaws that were dispersed in the material and which behave like cracks. As it was explained in the previous section, there is a strong correlation between the processing route and the appearance of critical flaws (see Figure 12b). As a consequence of that, the biaxial strength of the Ti(C,N)-FeNi composites fabricated through the SDP process showed a relatively high characteristic strength value compared to the characteristic strength of the SC-CIP and SC. However, the effect of carbon was not so evident in the fractography.

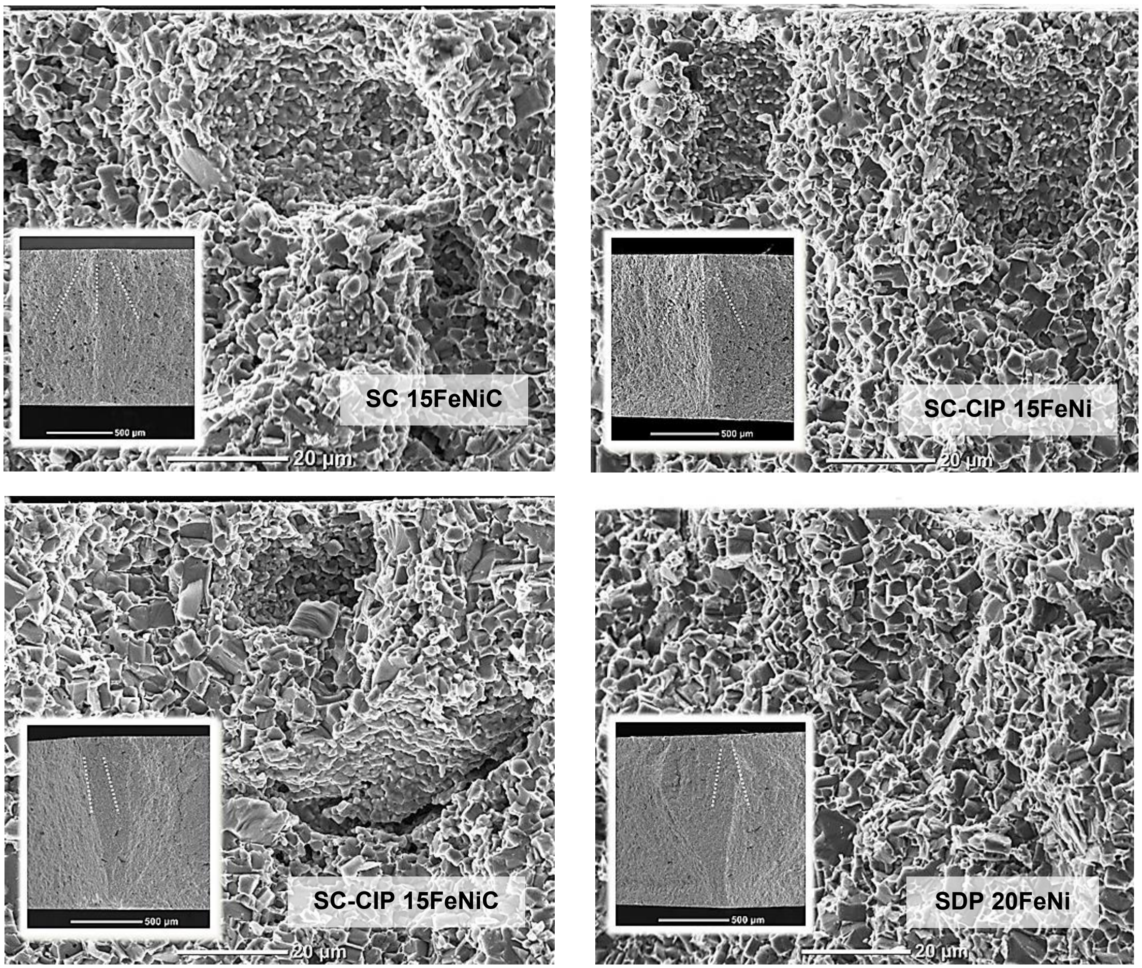

Figure 13. Fracture surfaces of a selection of cermets tested under B3B. The inserts show the macroscopic fracture, with the broken (white) lines pointing toward the fracture origin

Fracture resistance and failure analyses on SDP samples using SEVNB method

The fracture toughness was evaluated following the Versailles Project on Advanced Materials and Standards (VAMAS) procedure on pre-notched specimens [182]:

$$K_{IC} = Y' \cdot \sigma \cdot \sqrt{a} = \frac{F}{B\sqrt{W}} \cdot \frac{S_0 - S_i}{W} \cdot \frac{3\sqrt{\delta}}{2(1-\delta)^{1.5}} \cdot Y \qquad (1)$$

where σ is the failure stress, F the fracture load (in N), S_0 and S_i are the outer and inner spans respectively (in m), B and W are the specimen width and thickness respectively (in m) and Y is a geometric factor defined for an edge crack of length a, defined as:

$$Y = 1.9887 - 1.326 \cdot \delta - \frac{(3.49 - 0.68\delta + 1.35\delta^2)\delta(1-\delta)}{(1-\delta)^2} \qquad (2)$$

with:

$$\delta = \frac{a}{W} \qquad (3)$$

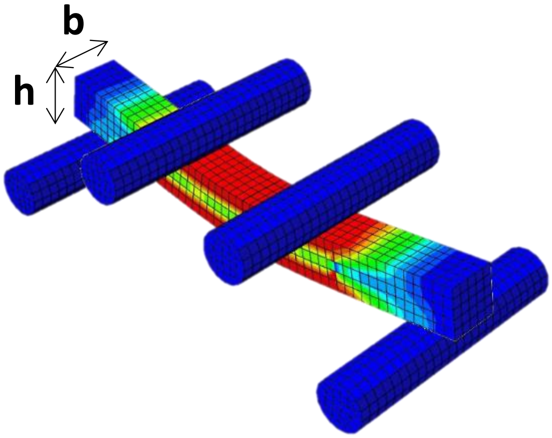

Figure 14. Scheme of Four Point Bending test

Additionally, to account for the contribution of the metallic matrix to the fracture energy of the cermets, the work-of-fracture (γ_{WOF}) was determined from the area under the stable load-displacement curves divided by twice the area of the un-notched part of the cross-section of the samples, according to [183]. As it can be seen in Table 8, there is a positive correlation between γ_{WOF}, K_{IC} and FeNi content. The FeNi content was evaluated in terms of mean free path (λ_{FeNi}) and contiguity $C_{Ti(C,N)}$.

The principal parameters used to characterize the microstructure of hardmetals are the average grain size of the carbide particles ($d_{Ti(C,N)}$) and the volume content binder of which are correlated by the contiguity of the carbide phase ($C_{Ti(C,N)}$) and the binder mean free path (λ_{FeNi}).

Mean grain size is a statistical concept that refers to the average size of the carbide particles that constitute a cermet. Contiguity is known as the fraction of the total internal surface area of a phase that is shared by particles of the same phase. This parameter partially describes the state of aggregation of the carbide phase. It is defined as the measure of the extent of the carbide grain boundary area relative to the total surface area of the carbide grains [184]. Therefore, by definition, the contiguity can vary between 0 and 1, assuming that this value tends to zero when the metal volume fraction tends to one. Roebuck and Bennett studied the contiguity as function of the binder content (V_{binder}) for a series of hardmetals and proposed the following empirical relation:

$$C_{Ceramic}(V_{binder})^{n}=D \qquad (3)$$

Where the best fitting is obtained when n and D constants take values of 0.45 and 0.2 respectively [185].

The contiguity is also simply related to the binder volume fraction (V_{binder}) and to the mean free path in the binder phase (λ_{Binder}) and in ceramic grains ($\lambda^{G}_{Ceramic}$) [186].

$$C = 1 - \frac{V_{Binder}}{\frac{\lambda_{Binder}}{\lambda^{G}_{Ceramic}}(1-V_{Binder})} \qquad (4)$$

The mean free path, also called the mean linear intercept in the binder phase (λ_{Binder}), is used to describe the distribution of the binder phase in metal-ceramic materials. It is the most important parameter to characterize the geometry of the binder phase, due to its inverse relation with the specific surface of the binder phase (carbide/binder interface per unit volume of binder) [187]. The microstructural parameter along with contiguity and volume content of binder, constitute the primary structural parameters of metal-ceramic materials. They are interrelated, as proposed by Lee and Gurland [186], according to (5) even for varying binder phase content and sintering conditions.

$$\lambda_{Binder} = \frac{1}{1-C_{Ceramic}} \frac{V_{Binder}}{V_{Ceramic}} d_{Ceramic} \qquad (5)$$

Where $V_{Ceramic}$ is the volume fraction of ceramic particles.

The binder mean free path increases when rising the carbide mean grain size and/or the volume fraction of binder. An increase in λ_{Binder} results in a higher fracture toughness of the composite, thus, lower hardness [188].

Table 8. Fracture toughness and work of fracture of the SDP samples.

Sample	Grain Size (μm)	Mean Free path (μm)	Contiguity	Fracture toughness K_{Ic} [MPa m$^{1/2}$]	Work of fracture γ_{WOF} [J/m^2]
15FeNi	2.21 ± 0.3	0.74 ± 0.09	0.470	12.2 ± 0.3	1514 ± 241
15FeNiC	2.30 ± 0.2	0.76 ± 0.06	0.470	11.9 ± 0.4	1314 ± 115
20FeNi	2.23 ± 0.3	0.95 ± 0.12	0.413	13.5 ± 0.4	1584 ± 251
20FeNiC	2.19 ± 0.3	0.93 ± 0.13	0.413	13.8 ± 0.2	1720 ± 105

Figure 15 shows the load vs. cross-head displacement curves corresponding to the four SDP specimens. All specimens show a typical brittle behavior (i.e. crack propagates unstable when the stress overcomes the fracture toughness of the material). It should be noticed that in this plot the slope of the 15FeNi specimens is similar to that of the 20FeNi samples. However, the lower the metal matrix content the lower fracture load (for both samples with or without carbon addition) as it can be seen in the work of fracture (Table 8). This behavior indicates that the higher fracture toughness value in 20FeNi samples (~14 MPa·m$^{1/2}$) must be related to higher metal content. In fact, as it can be inferred from the microstructures, for such composites, the Ti(C,N) is better surrounded by FeNi metal phase. The carbon addition did not significantly affect the measured fracture toughness of the materials. However, the strength results revealed a significant improvement in the 20FeNi specimens formulated with carbon. Table 8 also shows the ceramic contiguity and the binder mean free path, which were calculated to compare the proposed formulations and rationalize the effects of their microstructures on its mechanical behavior. The two parameters exhibited an opposite trend, i.e, the contiguity increased and the mean free path decreased with increasing the volume fraction of ceramic phase. As expected, K_{IC} measurements were found to be directly and inversely proportional to the binder mean free path and ceramic contiguity respectively [189].

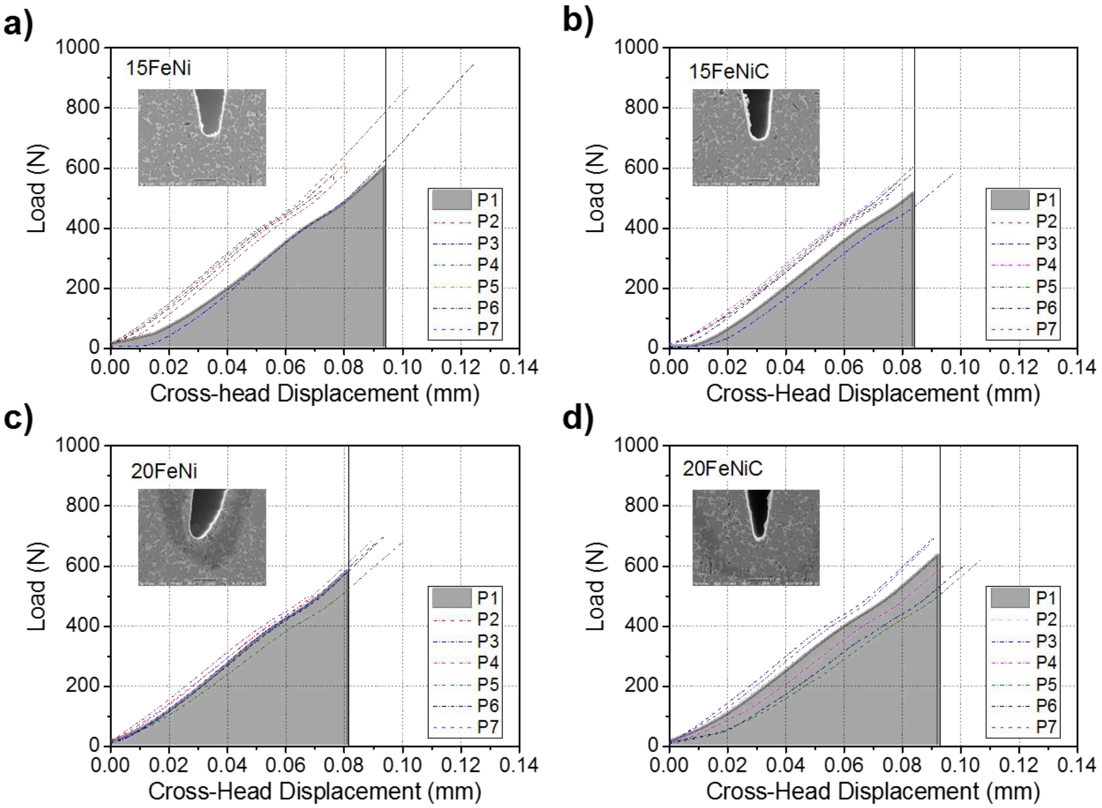

Figure 15. Load (in N) versus cross-head displacement (in mm) of the SEVNB samples corresponding to the a) 15FeNi, b) 15FeNiC, c) 20FeNi and d) 20FeNiC cermets respectively. SEM micrographs of the KIC notches are plotted for illustrative purposes. The shadow area in one of the specimens is used to calculate the work-of-fracture

These results may be explained by observing the fracture surfaces of the SEVNB specimens. Figure 16 shows micro-fracture features from the four SDP specimens. All cermets exhibit brittle fracture behavior on the macroscale, but on the microscale both the brittle fracture of the ceramic phase and the ductile fracture of the binder phase can be distinguished. This brittle fracture of the ceramic phase follows the transgranular mode of fracture characterized by the typical “river-like” pattern. This pattern occurs when the crack direction deviates from the crystallographic lattice plane of the Ti(C,N) phase. The cleavage fracture path through the carbide can either follow the crystallographic plane with relatively smooth surface that increases the deviation from the crack direction or return closer to the crack direction by jumping between the crystallographic planes, yielding the river-like ripples or steps on the surface. On the other hand, the fracture along the carbide-binder interface has remnants of the plastically fractured binder phase with shallow dimples on the smooth surface of the carbide. It is also important to notice the low amount of close porosity found in all cases, which is indicative of the proper sintering process.

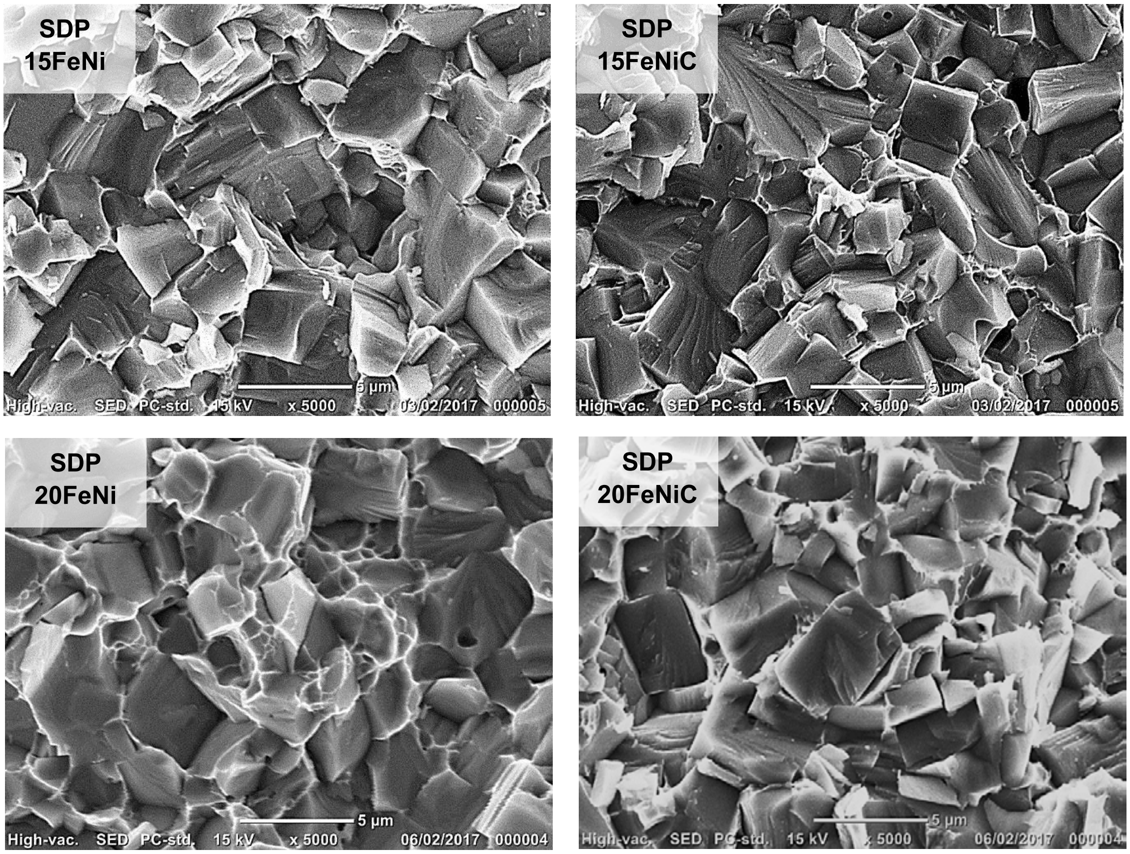

Figure 16. SEM micrographs of the fracture surfaces of SEVNB SDP samples with different composition: a) 15 FeNi, b) 15 FeNiC, c) 20FeNi and d) 20FeNiC.

It is worth mentioning that not all fractures were identical, revealing differences among the different compositions. It is clear how a higher concentration of dimples appears as the metal content increases in the composition of the cermet (from 15 vol. % to 20 vol. %). This phenomenon suggests that the material had broken through the ceramic/metal interface while retaining the hardness. As reported in measurements of biaxial resistance, the addition of carbon causes a slight modification related to the strengthening of the metal-ceramic material, as it happens in the case of the SDP 20FeNi materials (~1530 MPa without carbon and ~1870 MPa with carbon addition). These results are in agreement with that reported by Alvaredo et al. [104] in which a thermodynamic simulation using ThermoCalc® software was done to calculate the effect of carbon additions in the phase diagram of Ti(C,N)-Fe cermets. The results obtained showed a significant influence of the carbon percentage on the solidus temperature, which influences sintering behavior, leading to changes in the Ti(C,N) particles shape and composition, due to changes in the stoichiometry of the Ti(C,N). The experimental results obtained in this work constitute proof evidence that the appropriate carbon addition to cermet compositions is to be reflected in the cermet microstructure and mechanical properties.

Intrinsic hardness of constitutive phases: Nanoindentation testing, statistical analysis and flow stress for the constrained metallic binder

The mechanical behavior of each constitutive phase of Ti(C,N)-FeNi cermets, with different ceramic and binder content, was evaluated combining massive nanoindentation and statistical analysis to extract the intrinsic hardness for each constitutive phase. After that, using the intrinsic hardness for the metallic binder and the Tabor's relation, the flow stress was also determined.

Figure 17 shows micrographs attained by means of field emission scanning electron microscopy for Ti(C,N)-based cermets with different binder compositions. Mean grain size of the carbide particles ($d_{Ti(C,N)}$), carbide contiguity ($C_{Ti(C,N)}$) and binder mean free path (λ_{FeNi}) were measured.

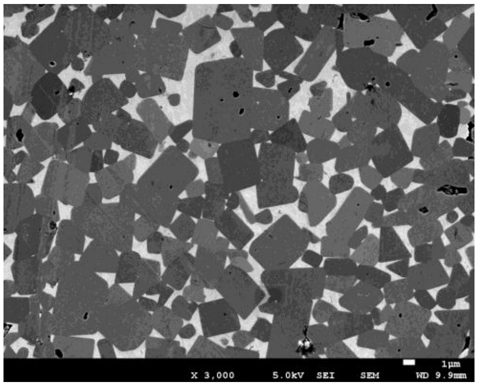

SDP 15FeNi	
$\mathbf{d_{Ti(C,N)}}$	2.30 ± 0.20 μm
$\boldsymbol{\lambda_{FeNi}}$	0.76 ± 0.06 μm
$\mathbf{C_{Ti(C,N)}}$	0.47

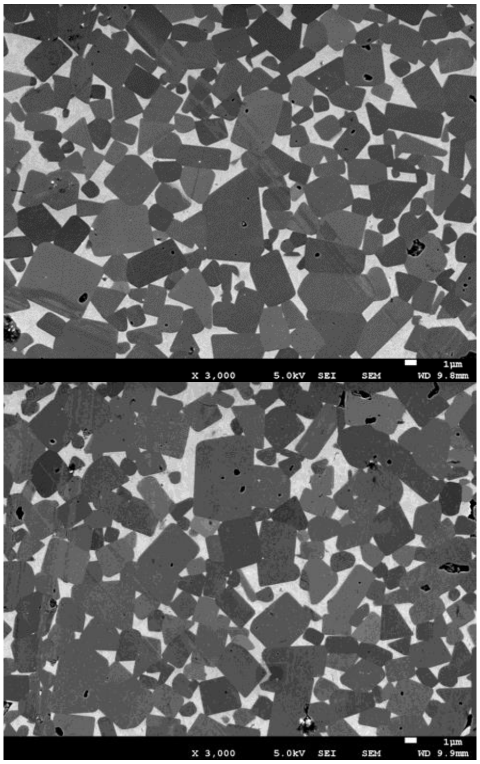

SDP 20FeNi

$d_{Ti(C,N)}$	2.23 ± 0.30 μm
λ_{FeNi}	0.95 ± 0.12 μm
$C_{Ti(C,N)}$	0.41

SDP 15FeNiC

$d_{Ti(C,N)}$	2.22 ± 1.14 μm
λ_{FeNiC}	0.76 ± 0.14 μm
$C_{Ti(C,N)}$	0.47

Figure 17. Microstructure and microstructural parameters for Ti(C,N)-based cermets: a) SDP 15FeNi, b) SDP 20FeNi and c) SDP 15FeNiC

Compared with traditional hardness testing, nanoindentation allows evaluating the mechanical response of individual phases heterogeneously distributed in the bulk. A massive nanoindentation protocol is proposed to statistically determine the intrinsic hardness for each constitutive phase to evaluate the effect of the metal binder fraction as well as the carbon content on the Ti(C,N)-based cermets processed. To do this, three different spaced arrays of 625 imprints were done at 200 nm of maximum penetration depth, according to the Ulm's method. Hardness histogram for SDP 15FeNi, obtained from nanoindentation with a constant bin size of 1 GPa, is shown in Figure 18. As it can be seen in this representation, three main peaks are illustrating the intrinsic hardness values for each constitutive phase. Highest value around 33 GPa corresponds to Ti(C,N) particles, while the lowest peak indicates the hardness for metallic binder, ~14 GPa. Intermediate peak centered ar 24 GPa, may be related to hardness distribution where indentations were implemented on the Ti(C,N) and binder interface. Figure 17b exhibits a small region of indentation array.

Experimental hardness values for the constrained binder obtained by statistical analysis of data from nanoindentation tests are wide scatter. Thus, they cannot be used as reliable data for modelling and/or microstructural design optimization. However, is a base parameter to be used in determination of the flow stress of the constrained metallic binder which have proved to give reliable results [190]. The flow stress (σ_{flow}) for the constrained metallic binder was estimated by using the Tabor's relation and the intrinsic hardness directly determined from the statistical method [191]. The hardness trend for an individual imprint performed in the metallic binder presents a hardness plateau and equals to 14.5 GPa, for maximum penetration depths of 200 nm which was considered as a suitable nanoindentation testing parameter to attain a successful implementation of the statistical method in these systems. Accordingly, flow stress for the metallic binder is found to range between 3.50 – 4.66 GPa (see Table 9).

These results correspond to the partial results of a work in progress. However, they allow us to confirm that they maintain the same trend observed in the previous hardness, biaxial strength and fracture toughness analyses. It would be very interesting to analyze the SDP 20FeNiC composition to draw some significant conclusions according to the results that this material throws after its analysis.

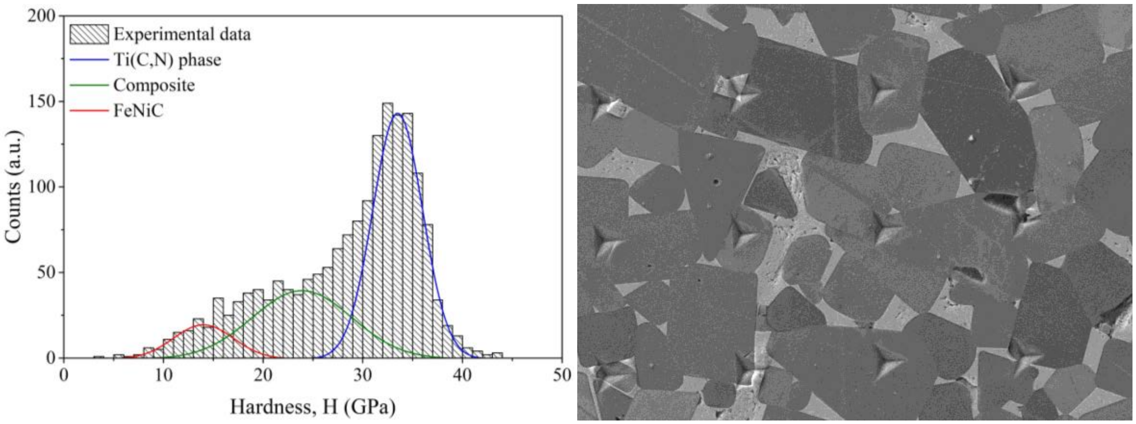

Figure 18. (a) Hardness histogram with 1 GPa of bin size. The simulated hardness using the statistical fitting parameters are overlaps through the statistical method fitting and (b) residual imprints observed at FESEM.

Table 9. Summary of the H values for each constitutive phase and the σ_{flow} of the metallic binder

Sample	H (GPa)			$\sigma_{flow, binder}$ (GPa)
	Ti(C,N)	Composite	Binder	
15FeNi	33 ± 5	24 ± 8	14 ± 6	3.50 – 4.66
20FeNi	32 ± 2	25 ± 5	14 ± 5	
15FeNiC	33 ± 3	24 ± 4	14 ± 5	

Summarizing, the effective combination of both colloidal and powder metallurgy techniques provides uniformity of the phase distribution and consequently step up reactivity during sintering, leading to full density materials with up to ∼1200 HV30 of hardness, ∼1900 MPa of biaxial strength, ∼14 MPa·m$^{1/2}$ of fracture toughness and ∼1700 J/m^2 of work of fracture for the SDP 20FeNiC material, being the best composite candidate to improve the mechanical performance of the proposed Ti(C,N)-based cermets meeting the requirements for tool materials.

The details of experimental procedure, the complete results and discussion is published in: [Paper 2 to 6]

4.- Alternative approach for the synthesis of metal-ceramic materials

Electroless Ni Plating: Chemical vs Ultrasound activation

An environmental-friendly electroless deposition (ELD) process was employed for Ni nanoparticles (NPs) deposition on Ti(C,N) micrometric particles. For it every single Ti(C,N) particle dispersed in aqueous media should be pre-treated prior to plating. In order to understand better the coating process, including the pretreatment, the mechanism of the formation of core-shell nanostructures, Ti(C,N)-Ni, is schematically depicted in Figure 1 and described as follows.

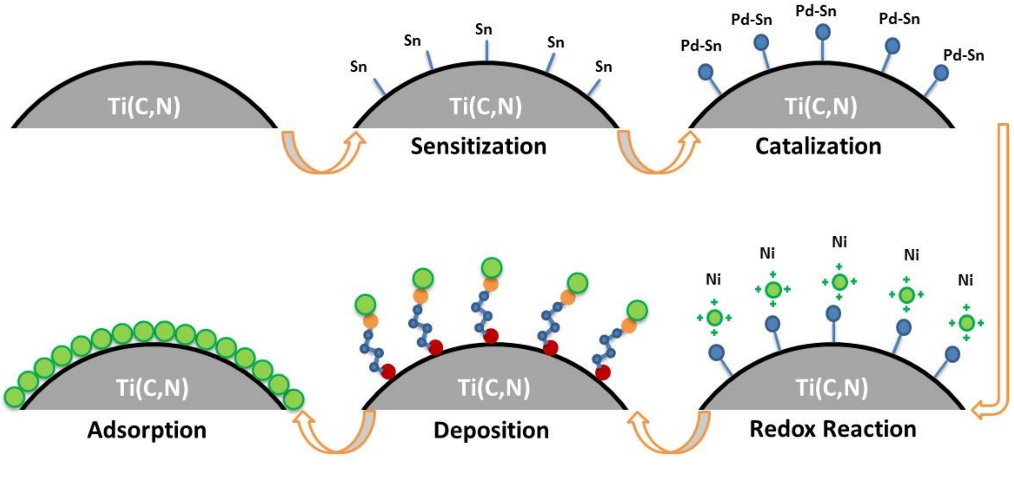

Figure 1. Schematic illustration of deposition process for the Ni-deposited Ti(C,N)

Based on studies described in the introduction for the EN plating of other ceramic particles, the present work pretends the deposition of Ni onto Ti(C,N) particles surfaces by using a $NiSO_4 \cdot 7H_2O$ precursor via the electroless Ni (EN) plating method was investigated using N-dimethyl amine borane (DMAB) as reducing agent. This infrequent commercial amino borane, useful for plating non-catalytic surfaces such as ceramics, is an effective reducing agent over a wider range of pH compared to the habitual reducing agents, such as borohydrides [150], while leaving a low amount of impurities, something of vital importance in future applications. Sodium citrate (CIT) was use as complexing agent and lactic acid (LA) was used as a chemical buffer in the electroless plating bath. Table 1 shows the formulation of precursors for this chemically activated synthesis.

Pre-treatment in the $SnCl_2$ solution enhances the adsorption of Pd^{2+} ions on the surfaces of the Ti(C,N) particles during activation. During sensitization, Sn^{2+} ions were adsorbed on the surfaces of the Ti(C,N) particles and act as seeds for the formation of Pd nuclei during the activation process. Although the stability of Ti(C,N) in acid conditions is limited [54], the pH of the $PdCl_2$ solution was adjusted to 4, since higher values of pH during the activation process could not dissolve $PdCl_2$ properly and would form $Pd(OH)_2$ by a hydrolysis reaction.

In detail, the Sn^{2+} ions react with Pd^{2+} to form uniform Pd catalytic nuclei. The reaction is described as follows in Eq. (1):

$$Pd^{2+} + Sn^{2+} \rightarrow Sn^{4+} + Pd^0 \qquad (1)$$

The Pd activation assured the elimination of passive surfaces, making Ti(C,N) particles suitable for plating. Reduced Pd atoms remain on the surface after the sensitization process. When the charged nickel particles encounter the Ti(C,N), it is possible that the Pd-Sn catalytic nuclei on Ti(C,N) particles react with part of Ni^{2+} leading to Ni nanoparticles, as follow:

$$Pd^0 + Ni^{2+} \rightarrow Ni^0 + Pd^{2+} \qquad (2)$$

But moreover, when the activated Ti(C,N) particles were introduced into electroless Ni plating bath, an autocatalytic redox reaction with DMAB can happen:

$$3Ni^{2+} + (CH_3)_2NH\cdot BH_3 + 3H_2O \rightarrow 3Ni^0 + (CH_3)_2NH_2^+ + H_3BO_3 + 5H^+ \qquad (3)$$

Those reactions indicates that Ni^{2+} is reduced by DMAB, and this reaction is catalysed by the Pd nuclei. Then Ni deposits onto the surface of Ti(C,N) and a Ni-coating layer is formed surronding Ti(C,N) particles.

Several studies were carried out to determine the optimum process parameters. Preliminary Ni electroplating tests without any pretreatment of the Ti(C,N) particles leads to unsuccessful results due to the non-catalytic surface of Ti(C,N) particles. Electroless Ni plating in Ti(C,N) suspensions requires active sites on the particle surfaces to initiate the deposition of metallic Ni species. Consequently, Pd catalyzes the reduction of metal ions (equation 2) and nuclei provide reaction sites where the Ni^{2+} reduction proceeds rapidly (via equation 3).

On the other hand, DMAB was used to avoid undesirable P plating when using sodium hypophosphite ($NaH_2PO_2 \cdot H_2O$), the most regular reduction agent in electroless Ni (EN) plating [127]. Moreover, the suspension of activated Ti(C,N) particles in the EN solution was performed at room temperature and buffering the suspension at pH 4, with the addition of LA, in order to improve mixing of all reactants before the reduction takes place.

The plot in Figure 2 shows the stability of Ti(C,N) particles in terms of evolution of zeta potential with the addition of CIT to the suspension at pH 4 and 10. During the mixing step at pH 4, the stability of Ti(C,N) particles in the EN solution is limited [54] as the low absolute value of zeta potential (-10 mV) reflects, and then EN plating could be conditioned [137]. However, the increase of pH leads to a higher absolute value of zeta potential (-40 mV), which means a considerable increase of the suspension stability for plating.

However, the plot also shows that under acidic conditions, the zeta potential increases with CIT concentration up to stabilize absolute values over 40 mV for a CIT addition higher than 0.2 wt. %, evidencing the adsorption of CIT onto the Ti(C,N) particles. In this sense, CIT, a regular complexing agent in EN solutions with a first pKa of 3.14, enables the stability of the suspension throughout the adsorption of the deprotonated carboxyl groups (Figure 2) to the Ti(C,N) surface, and help to maintain the Ti(C,N) particle dispersion during the precursor mixing. Then the results plotted in Figure 2 show that, during the EN process, the micrometric particles settling was avoided by assuring the Ti(C,N) stabilization with the complexing agent. Similarly, LA with a pK_a of 3.86, can also be adsorbed onto the Ti(C,N) particles under mixing conditions. That mean both additives, could interact with Ni^{2+} as ligands.

Moreover, under basic conditions in Figure 2, a similar addition of CIT determines a further increase of the zeta potential value when higher pK_a values are reached (4.76 and 6.40). The CIT and LA are then anchored by the carboxylic groups to the surface of Ti(C,N) particles and chelated with catalytic metal ions, favoring the electroless metal deposition [123]. The EN process was carried out at pH 9, and consequently an exponentially increasing number of the terminal groups in the –COOH and carboxylate/Ni^{2+} complexes are formed. Once these carboxylate/Ni^{2+} surfaces have been formed, they can be reduced by DMAB. So nucleation during the EN plating can be controlled by the formation of Ni^{2+}/Carboxylate surface complexes.

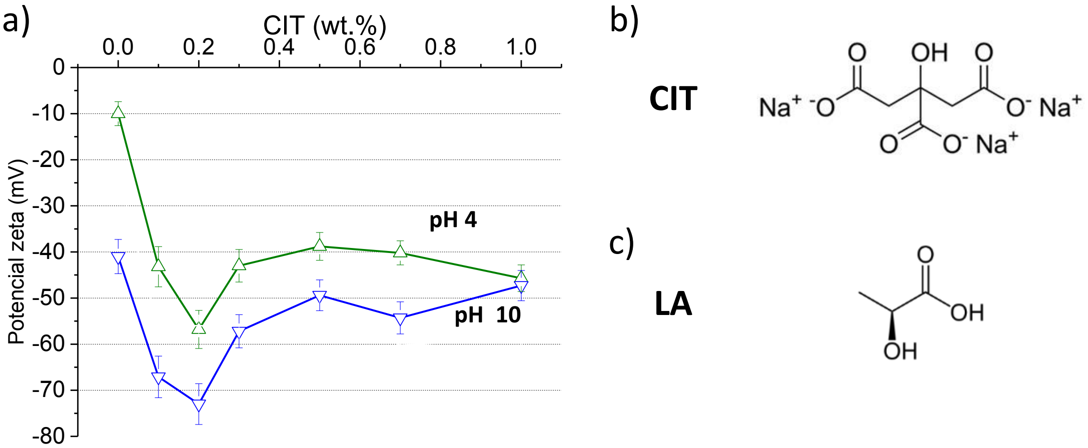

Figure 2. (a) Evolution of Zeta Potential of Ti(C,N) suspesnions with the addition of sodium citrate (CIT) for pH 4 and 10. Molecular structure of CIT (b) and LA (c).

FESEM micrographs of as-received Ti(C,N) as well as the Ti(C,N)-Ni core-shell structures formed are shown in Figure 3a, b and d, respectively. The as-received Ti(C,N) powder shows the surface feature of bare particles (Figure 3a), while the view of the plated surface evidences the presence of a homogeneous coating of Ni NPs which covers uniformly both, the coarse Ti(C,N) particles (Figure 3b) and the fine fraction (Figure 3d). Fine fraction seems to have a denser and smoother Ni NPs coating that fully covers the particle surface. The elemental EDX mapping exhibited in Figure 3c reveals the formation of the hetero-structure after the electroless plating. As seen, pure Ni (blue dots) are deposited on the surface of the Ti(C,N) particles (in green). Any evidence of the presence of residual impurities is not detected by EDX (not shown here). Therefore the absence of residues coming from the pretreatment and plating steps (such as Sn, Pb or B) could indicate the complete plating reaction carried out.

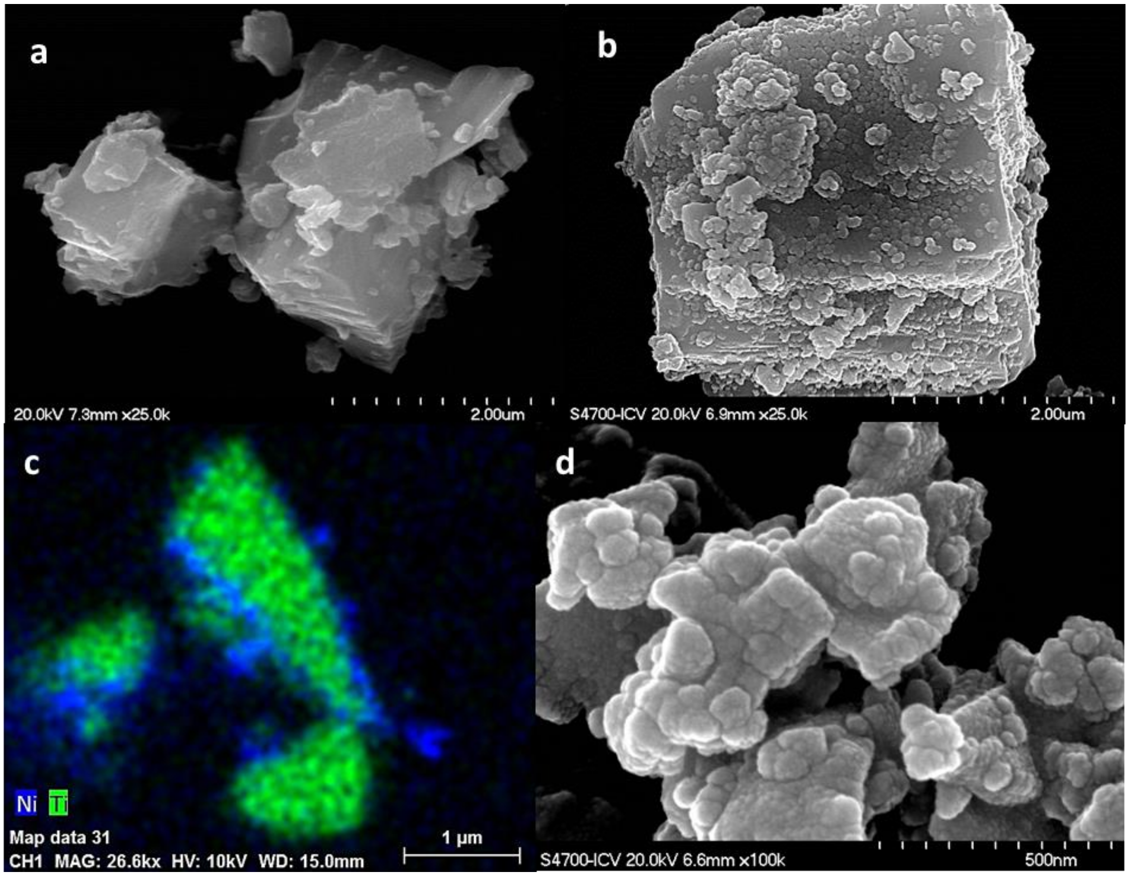

Figure 3. FESEM micrograph of uncoated Ti(C,N) particle (a), FESEM micrograph of Ni-plated Ti(C,N) particles (b) and (d), and EDS analysis of core-shell structure formed after plating (c).

Similar results were obtained by Zou et al. [143] in 2006 and Uysal et al. [141] in 2011 for electroless Ni plating of SiC particles. However, in those works, sodium hypophosphite ($NaH_2PO_2 \cdot H_2O$) was used as reducing agent resulting in a Ni-P particulated corona, and EN plating was performed under higher activation temperatures (45-70 ˚C). These manuscripts suggest that metal nucleates and grows around the catalytic centers on the ceramic surfaces. Then, smaller distance between nuclei in small Ti(C,N) particles could be the cause of the formation of a continuous and smoother Ni NPs layer (Figure 3d), while catalytic center separation in coarse particles could reduce the uniform growth of the Ni coating (Figure 3b) [141]. Consequently, the uniform and high dispersion of catalytic centers provided by pretreatments is a crucial aspect for EN plating of Ti(C,N) particles.

Figure 4a shows the low-magnification TEM image of Ti(C,N)-Ni core-shell structure formed after the EN plating process. High magnification HRTEM images presented in Figure 4b and c shows a large amount of fine dark spots deposited on the surface of the Ti(C,N) particles. As it was evidenced in the prior EDX analysis (Figure 3c) dark spots are Ni NPs of less than 20 nm in size, which confirm the role of complexing agents, CIT and LA, favoring the formation of Ni NPs surrounding the surface of Ti(C,N) particles, and not in the liquid medium. In fact, the homogeneity in size and crystallinity of the deposited Ni NPs is due to the complexing effect of both CIT [192] and LA. Figure 4d displays lateral high-magnification HRTEM micrograph of Ti(C,N) particles in which we can find that the Ni NPs form crystalline domains. By measuring the lattice spacing in the HR-TEM image (Figure 4e and f), the interplanar spacing was found to be 1.95 Å (d-spacing ranging 1.90–2.10 Å), corresponding to the (111) planes of the cubic unit cell which indicates the formation of pure, crystalline Ni.

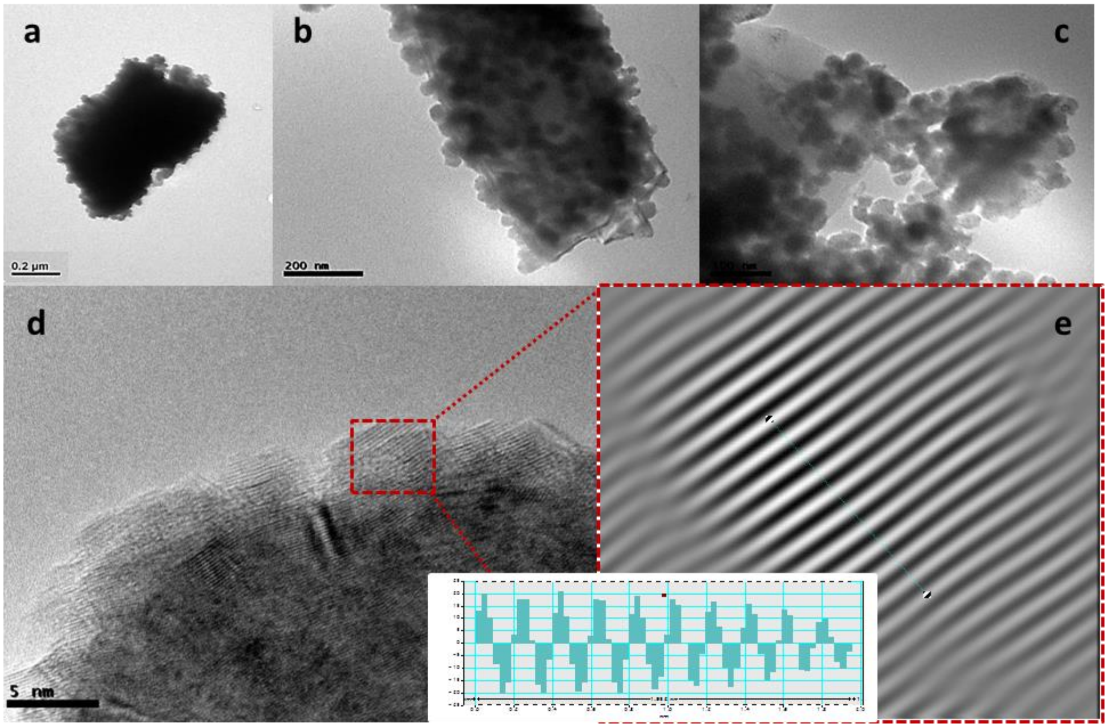

Figure 4. TEM (a) and HRTEM ((b), (c) and (d)) micrographs of the core-shell Ti(C,N)-Ni nanostructure. The crystallographic distances along the (111) plane of Ni can be observed ((e) and inset)

Although we present here successful results of the EN synthesis, this technique has a clear limitation when we apply it to the formation of core-shell Ti(C,N)-Ni nanostructures in concentrated Ti(C,N) suspensions for slip casting or spray drying techniques. The low particle concentration of the ceramic suspensions in which this procedure can be carried out (<< 1 vol. % solid content) limits its final application as a technique for the production of bulk powders or pieces [141,143]. Therefore, two new bottom-up approaches for obtaining Ti(C,N)-Ni and Ti(C,N)-Ni(OH)$_2$ core-shell nanostructures were proposed replacing the chemical by the ultrasonic (US) activation. The substitution of the chemical activation mechanism would avoid activation and cleaning steps, allowing the in situ synthesis of metallic NPs in Ti(C,N) suspensions with a higher solid content (at least > 1 vol. %), for their subsequent processing by the shaping and granulating techniques described above.

For comparative purposes, these sonically activated syntheses were formulated for the Ni precursor concentration used in the EN plating, and fitting optimized conditions achieved in previous works [153]. In Table 1 the variables involved in the synthesis are pointed out and compared. The protocol followed for US activated synthesis will be explained bellow (Figure 6 and Figure 12).

Table 1 Formulation of the chemically and sonically activated syntheses.

	Chemical Activation Route	**Sonically Activation Route**	
	Electroless Plating Ti(C,N)-Ni	**Synthesis by Reduction Ti(C,N)-Ni**	**Synthesis by Precipitation Ti(C,N)-Ni(OH)$_2$**
Ti(C,N)	**54.1 mM**		
Precursor	1M Ni(SO$_4$)·7H$_2$O	1M Ni(NO$_3$)$_2$·6H$_2$O	1M Ni(NO$_3$)$_2$·6H$_2$O
Reductant	1.38M DMAB	60M Hydrazine	---
Stablilizer	10M Lactic Acid	---	---
Complexing agent	6M Sodium Citrate	---	0.85M Ammonium Citrate
pH adjust	NH$_4$OH	10M KOH	5M NH$_4$OH
Volume	20 mL	50 mL	50 mL
Medium	**DI Water**		

Figure 5 shows HRTEM micrographs of the resulting core-shell nanostructures obtained through the proposed approaches and precursor solution formulations. As can be seen in Figure 5b, the results of the in situ synthesis of Ni by reduction are very promising. The Ti(C,N) particles are completely surrounded by Ni nanoflakes (Figure 5b) even smaller in size than Ni NPs obtained by EN plating. However, the absence of ligands in this synthesis leads to the formation of Ni nanoflakes, not only in the surface of Ti(C,N) particles, but also in the liquid medium. Consequently, CIT was also considered as ligand in this route of synthesis in the following studies.

On the other hand, the micrograph of the Ti(C,N) particles resulting from the precipitation route (Figure 5c) does not show any sign of formation of Ni(OH)$_2$ nanoparticles.

Considering these preliminary results, US routes were explored for both homogenous and heterogeneous syntheses, in a Ni precursor solution and in a Ti(C,N) suspension stabilized in the Ni precursor solution, respectively.

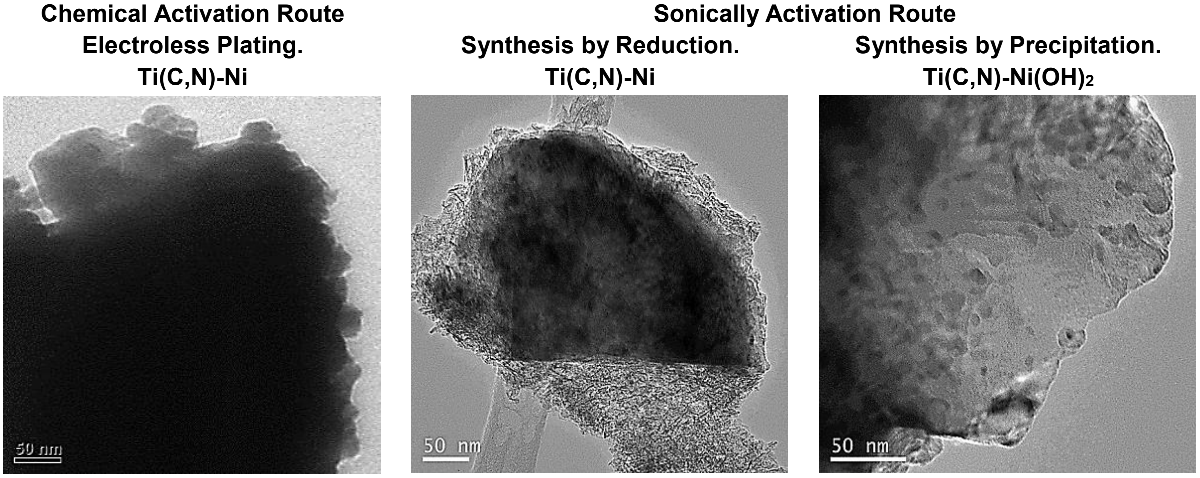

Chemical Activation Route
Electroless Plating.
Ti(C,N)-Ni

Sonically Activation Route
Synthesis by Reduction.
Ti(C,N)-Ni

Synthesis by Precipitation.
Ti(C,N)-Ni(OH)₂

Figure 5. HRTEM images of the Ti(C,N)-Ni/ $Ni(OH)_2$ core-shell nanostructures synthesized according to the three routes described in Table 1

Ultrasonically activated synthesis of Ni species

In this section, ultrasound energy was used as the activation force for the precipitation of Ni species. According to the mechanisms of synthesis described in the introduction, applied US provokes the ammonium evaporation, forcing Ni and $Ni(OH)_2$ precipitation, but also improves the dispersion of Ni nuclei. The shock waves created by the US in the suspension facilitate the formation and dispersion of a larger number of dispersed Ni nuclei, promoting the precipitation and leading to smaller and narrower particle sizes distributions [193].

Two US activated routes were considered, the reduction of Ni and the precipitation of $Ni(OH)_2$ nanostructures. The evaluation of the influence of different variables, such as $[Ni^{2+}]$, reducing agent or ligand addition, temperature, time and US power, was carry on for the homogeneous reduction of Ni. Based on this study, the heterogeneous routes of the in situ synthesis of both species, Ni and $Ni(OH)_2$, in the Ti(C,N) suspensions were designed with the final objective of shaping Ti(C,N)-Ni materials by slip casting and vacuum sintering.

Ni NPs homogeneous/heterogeneous chemical reduction activated by US

Ni NPs were synthesized by the chemical reduction of Ni^{2+} with monohydrate hydrazine using a high intensity ultrasonic horn, following the simplified equation:

$$2Ni^{2+} + 4OH^{-} + N_2H_4 \rightarrow 2Ni + N_2 + 4H_2O \qquad (4)$$

The synthesis procedure can be described as follow (Figure 6): Ni precursor was dissolved into deionized water (solution A). Separately, one mixture was prepared by dissolving KOH and N_2H_4 in water (mixture B). Then, mixture B was poured into solution A while US was applied up to achieve final total solution volume of 50mL. The temperature was controlled through the recirculation from a cryothermal bath. The products of the synthesis were washed thoroughly for several times with deionized water at pH≈9 (adjusting with tetramethyl ammonium hydroxide, TMAH) to residues removal. CIT was also considered as synthesis modifier to produce and maintain dispersed nanoparticles in aqueous media with a molar ratio of 1:0.0083 [Ni^{2+}]:[CIT]. The addition of CIT was carried out by dissolving it previously in the solution A prior to the pouring of mixture B.

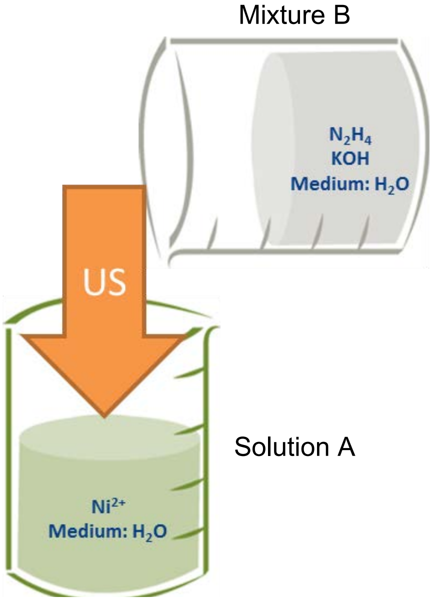

Figure 6 Scheme of the homogeneous synthesis procedure

Considering the oxidation-reduction potentials of these species, Ni NPs cannot be synthesized under pH 9.5 according to the Nernst equation [171]. Noting that our synthesis took place in presence of

US, and as a consequence of the sonocrystallization the formation of numerous nuclei, homogeneously dispersed in the aqueous solvent, was expected [151]. It is known that and excess of US can lead to the formation of clusters of nanoparticles. However, in this work the ultrasound is mainly used to effectively disturb the precursor's solution and disperse the nuclei. Taking account these aspects, the influence of variables such as ion nickel concentration [Ni^{2+}], US time and power, were evaluated in terms of the called "S parameter" [W/(mol/L)·s], which is equivalent to the number of watts per second that a mol/L of Ni^{2+} experiences in each synthesis. This parameter was defined to quantify the efficiency of each factor on the resulting size of the NPs [151,194].

All synthesis conditions are collected in Table 2 and related to the process yield and the mean particle size of the NPs population, in number and volume. It is relevant to note that most of the NPs populations in volume exhibit bimodal distributions, where distributions of a fine fraction of particles are centred between 70 and 345 nm and coarse agglomerates are in the range of 450 and 715 nm. The mean particle size of the fine fraction in volume fits the mean particle size in number. Consequently, those distributions evidence the NPs agglomeration during the synthesis, where firstly the synthesis was driven by the formation of small primary particles, followed by the formation of large secondary aggregates. The partial agglomeration of Ni NPs can be due to their slight oxidation in the basic pH aqueous medium after the precipitation by reduction, and the later surface hydration, which promotes the formation of soft links such as hydrogen bridges among nanoparticles.

Table 2 Conditions of Ni reduction and results

Variable	Molar ratio (Ni^{2+}:KOH:N_2H_4)	T (°C)	[Ni^{2+}] (M)	Time (min)	P_n (W)	S (W/(mol/L)·s)	Yield (%)	D_{n50} (nm)	D_{v50} (nm)		Labeled
S	1:10:60	50	0.1	5	63	2.1	84	104	120	461	Ni-2.1.S
				5	31.5	1.1	78	140	164	615	Ni-1.1S
				60	63	0.2	83	300	342	615	Ni-0.2S
[Ni^{2+}]	1:10:60	40	0.1	60	63	0.2	78	105	122	615	Ni0.1M
	1:10:60		0.075			0.2	84	90	91	531	Ni-0.075M
	1:10:60		0.05			0.3	80	75	77	408	Ni-0.05M
	1:10:60		0.02			0.9	-	-	-	-	Ni-0.02M
[N_2H_4]	1:10:20	40	0.05	60	63	0.3	76	115	164	712	Ni-20
	1:10:6						-	-	-	-	Ni-6
[CIT]	1:10:60	50	0.1	5	63	2.1	85	64	67	323	Ni-CIT

All obtained X-Ray diffraction (XRD) patterns of the synthesized NPs determined by three characteristic peaks of the face-centered cubic (FCC) structure of Ni (45°, 52.4° and 76.9°), corresponding to Miller indices (111), (200) and (222) respectively according to the index card JCPDS no. 04-0850 (Figure 7a). Besides, the pattern indicates the absence of impurities and secondary phases. The crystallite size of Ni NPs is 14.6 nm and the cell parameter is 3.48 Å. The unit cell dimension calculated from the Scherrer equation is higher than values reported in literature for Ni NPs (2.01 Å) [195–197], while the crystallite size denotes that primary particles of 70 – 345 nm determined by DLS are made on nanocrystalline domains.

Although similar Ni nanocrystals were then the product of all the syntheses, in order to obtain the smallest population of Ni NPs, more relevant differences among particles in terms of DLS size were inspected. In Table 2, when the "S parameter" decreases, either decreasing by half of the US power or increasing reaction time up to 60 min, the mean particle size of the NPs fine fraction increases from 90 to 300 nm. All these syntheses started turning the solution's colour to black, indicating that the reduction process was completely finished after the first 5 min. Thus, the rest of the time was employed in increasing the size of the agglomerates (not desired).

Also, the results for the second variable, [Ni^{2+}], in Table 2 indicate a decrease of the mean NPs size fine fraction from 105 to 80 nm due to the decrease of the [Ni^{2+}] (keeping constant the temperature, US power and time). A reduction of Ni precursor leads to a higher effect of the US on the existing material and thus promotes the formation of smaller nuclei during the reduction process. Note that a threshold value (synthesis Ni 0.02M) exists for the [Ni^{2+}] in which below 0.02M there is no reduction reaction, even after 60 min.

On the other hand, the decrease of N_2H_4 concentration (expressed as ratio between synthesis precursors) from 60, 20 to 6 (second and third variables studied in Table 2), shows a slightly size growth of the NPs from 80 to 115 nm (keeping constant temperature, US power, reaction time and even [Ni^{2+}]). In presence of a lower amount of reducing agent, only a few Ni nuclei were formed in the early stage of the reduction reaction. Later, in successive steps, the growth of NPs is carried out through the Oswald Ripening [198] producing an increase of the agglomerates size. There is no formation of new nuclei. The reduction rate of the Ni^{2+} slowed by diminishing the amount of hydrazine, and a new threshold value for this synthesis was observed. The reaction did not occur below of a

N_2H_4 ratio of 6. Although the reducing agent was used in a supra-stoichiometric concentration, the selected values for all these experiments have always been lower than the values described previously by some authors in other works [171].

The plot in Figure 7b shows the particle size distributions of NPs with D_{v50} in the nanometric range (< 100 nm), labelled in Table 2 as Ni-CIT, Ni-0.05M and Ni-2.1S. These distributions verified that NPs form clusters in water with particle sizes ranging from ten to several hundred nanometers. Note that in the Ni-CIT powder (considering the modifier addition) particle sizes ranged from 60 to 400 nm and 70 vol. % of the particles were smaller than 80 nm. By contrast, in the Ni-2.1S and Ni-0.05M powders (US time of 5 min and 0.05 M [Ni^{2+}], respectively) particle sizes ranged from 60 nm to 0.9-1.2 μm, and a lower volume of particles were smaller than 100 nm. These results, confirms that the addition of CIT maintains the NPs dispersed before the synthesis lowering the degree of agglomeration. The FESEM images in Figure 7c and d shows the Ni clusters and the dispersed NPs obtained from the synthesis with and without CIT, evidencing the nanometric size of the Ni NPs in both cases.

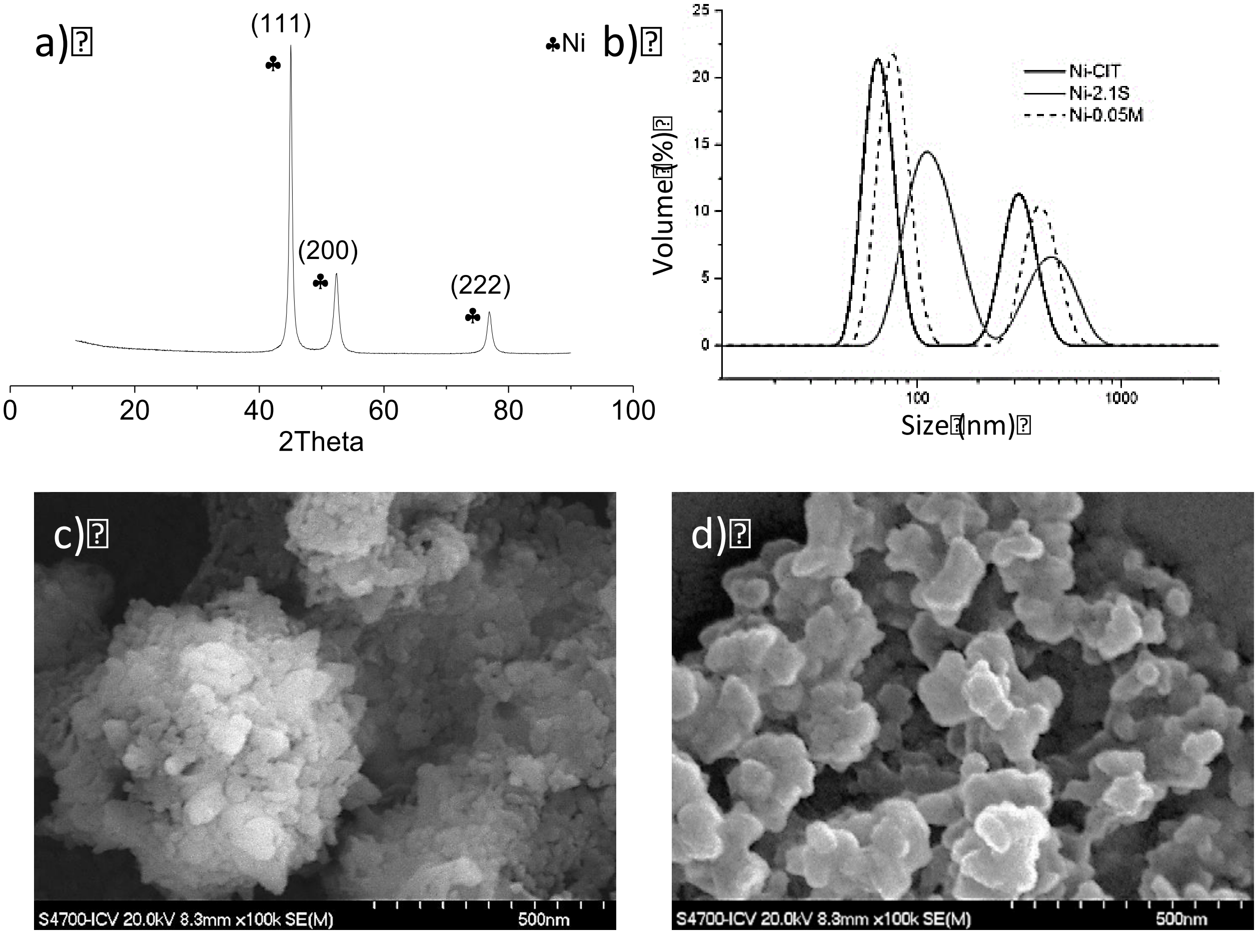

Figure 7. (a) XRD of Ni NPs synthesized (b) Particle size distribution of the syntheses Ni-CIT, Ni-2.1S and Ni-0.05M. And FESEM image of the clusters of Ni NPs synthesized without (c) and with (d) CIT

The results extracted from this study verify the conclusion of the EN plating: the CIT plays a double role as synthesis modifier, extremely relevant to produce and maintain dispersed nanoparticles in aqueous media. The particle size of as-synthesized Ni decreases with the S parameter [W/(mol/L)s], while the concentration of Ni^{2+} and the related amount of N_2H_4 has on each thresholds in order to produce Ni NPs under described US conditions. Moreover, the supra-stoichiometric concentration of N_2H_4 was optimized in the reducing process of NP's, this point being extremely relevant for the design of the reactants solution in Ti(C,N) suspension.

In this sense, the heterogeneous synthesis of core-shell Ti(C,N)-Ni through the reductant route was carried out according to the optimal conditions stablished for the homogeneous synthesis. The optimum conditions of the Ni NPs synthesis include a minimum ratio $Ni(NO_3)_2 \cdot 6H_2O/N_2H_4$ (~1/60) to provide a homogeneous distribution of the metal phase in the microstructure. But also there is a limit for the dissolution of the precursor ($Ni(NO_3)_2·6H_2O$) and reactants (KOH, N_2H_4 and CIT) in the liquid medium of the Ti(C,N) suspension, which also limits the solid content of the suspension. In our synthesis, the limit of the Ti(C,N) suspension concentration is 3 vol. %, in which the minimum volume necessary for the dissolution of reactants are assured, that leads to the processing of a Ti(C,N)-Ni composite with a final composition of 96/4 v/v, if a 100% yield of Ni chemical reduction is considered.

In accordance with the above, a Ti(C,N) suspension with a 3 vol. % solid content was prepared using DI water as dispersion media. The procedure to synthesize the Ni nanoparticles was similar to that used for the homogeneous precipitation described previously. The Ni precursor, was dissolved in the suspension vehicle (DI water) before the Ti(C,N) particles addition. The precipitation of Ni NPs was activated by the addition of a mixture of N_2H_4 and KOH during the application of US. The [Ni^{2+}] was fixed to 0.38 M for coating 3 vol. % Ti(C,N) particles in suspension. The molar ratios among reactants were 1 [Ni^{2+}]: 10 KOH: 60 N_2H_4, labeled this formulation as Ni60Hz. Core-Shell structures were obtained by the chemical precipitation of Ni NPs onto the surface of micrometric Ti(C,N) particles. These particles were used as seeds. Ni NPs precipitate under US application when the KOH/N_2H_4 mixture was poured into the Ti(C,N) suspension. US were applied with a 100% of the nominal probe power, during 5 min, maintaining the temperature of the suspension below 50 ºC, by external refrigeration with a cryothermal bath. US achieve 2.16 W/mol·s considering the fitted Ni^{2+} concentration. The formulation of the Ti(C,N) suspension and Ni^{2+} solution, was done for a final composition of Ti(C,N)-Ni composites (core-shell particles) of 96/4 v/v Ti(C,N)-Ni (labeled as 4Ni60Hz).

To determine the composition of the core-shell structures, the powder obtained after the synthesis was dried at room conditions and analyzed by XRD. Figure 8a shows the XRD pattern of the as received Ti(C,N) particles corresponds to the main reflections of Ti(C,N) (indexed using JCPDS card 042-1488). The analysis of the Ti(C,N)-Ni powders obtained from the synthesis, results in a similar pattern that the as-received Ti(C,N) powders. Ni is a minor constituent and the estimated amount of Ni in the final composite is close to the detection limit of the equipment, and consequently the overall scan of the composite material only show the Ti(C,N) peaks. However, a more accurate scanning of the composite (between 45 and 60˚) results in the pattern plotted in Figure 8b. In this case, the XRD spectrum shows the characteristic peak of FCC Ni lattice (at 52˚) which corresponds to the Miller index (200) and that roughly evidences the presence of Ni in the product of the synthesis.

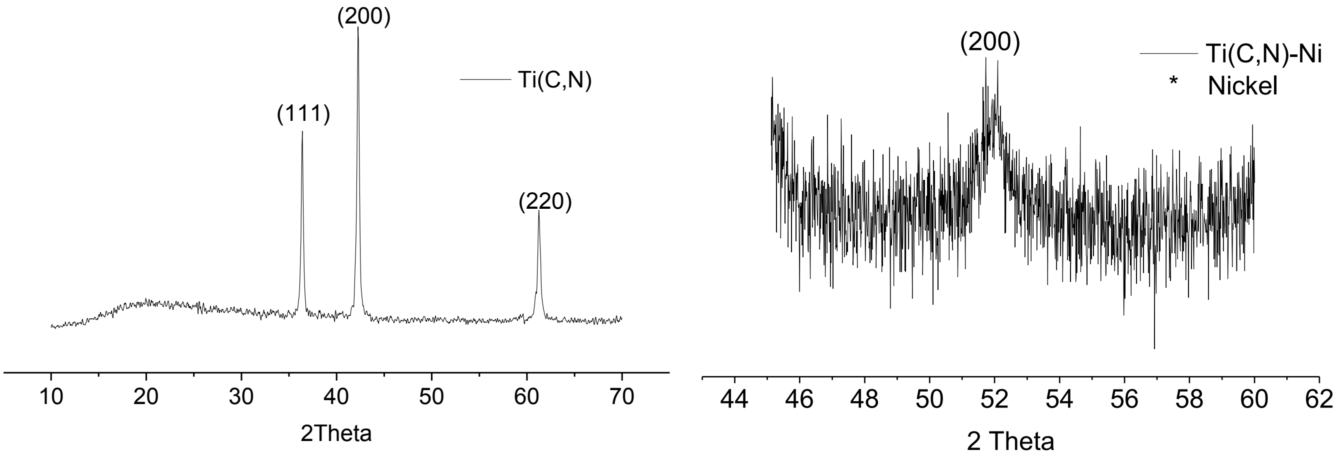

Figure 8. XRD spectrum of (a) as-received Ti(C,N) particles and (b) accurate XRD of Ti(C,N)-Ni tailored particles

The study of the morphology, crystallography and composition of the synthesized core-shell structures HR-TEM, STEM and EDX were carried out. Figure 9 shows a STEM image (a) of the composite and the line analysis of the Ni and Ti elements across the core-shell (b) determined by EDX. The micrograph shows brighter regions around the Ti(C,N) particle corresponding to a continuous layer of Ni which has grown onto the Ti(C,N) surface. As the analysis of the cross-section evidences, a Ni layer with a thickness of around 50 nm surrounds the Ti(C,N) particle leading to a composite fashioned in a core–shell nanostructure.

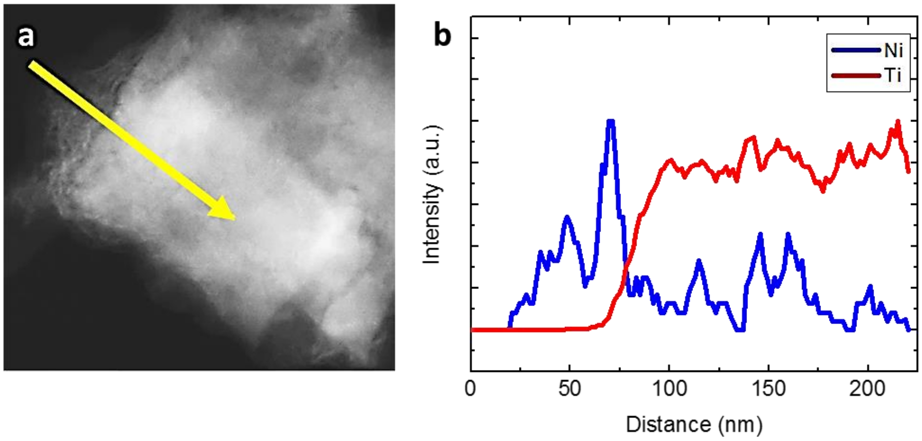

Figure 9. STEM image of the Ti(C,N)-Ni composite (4Ni60Hz) and line profile of the Ni and Ti analysis

In a general inspection, we can assume that the amount of precipitated Ni decreases with Ti(C,N) coarsening. This could be the consequence of the higher specific surface area of the fine fraction of the Ti(C,N) population. 3D growth of the flower-like NPs evidenced in the STEM images in Figure 10 a and b fits with the morphology intuited by SEM for the Ni precipitates (Figure 7c). STEM images of the composite shows in Figure 10 a and b corroborate the massive precipitation of Ni onto the smaller Ti(C,N) particles, either flower-shaped or as a layer, wrapping the particle or core-ceramic structure (Figure 9). Consequently, the feature of the Ni precipitates changes depending on the suspension formulation, basically on the [Ni^{2+}] as well as on Ti(C,N) concentration and on the size of the synthesis holder or surface. The wide size distribution of the micrometric ceramic particles lacks the metal matrix uniformity, because of the fine fraction of powders provides preferential sites for Ni nucleation.

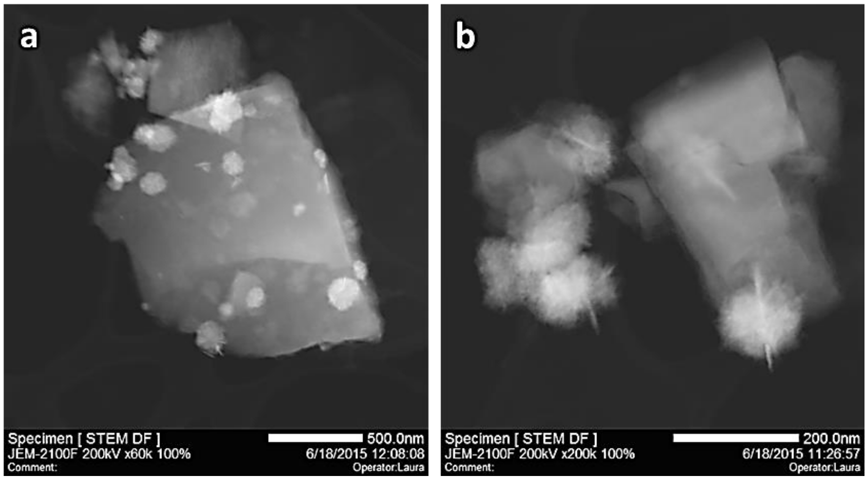

Figure 10. STEM micrographs of Ti(C,N)-Ni particles of 4Ni60Hz

$Ni(OH)_2$ NPs homogeneous/heterogeneous precipitation activated by US.

A second bottom-up approach to build the cermet microstructure through the synthesis of $Ni(OH)_2$ NPs on the surface of Ti(C,N) micrometric particles, that is synthesizing Ti(C,N)-$Ni(OH)_2$ core-shell structures, is proposed in this section.

Based on a previous works [151,153], the homogeneous synthesis of $Ni(OH)_2$ NPs by the application of US to an aqueous solution of the Ni ammonia complexes, was used. In contrast to the previous synthesis, ammonia is not used as a direct precipitating agent or as a liquid medium but as an intermediate complexing agent for Ni^{2+} ions prior to the precipitation of $Ni(OH)_2$ [152,155], as follows:

$$Ni^{2} + X\ NH_3 \rightarrow [Ni(NH_3)_x^{2+}] \quad (5)$$

$$[Ni(NH_3)_x^{2+}] + 2OH^{-} \overset{)))^{*}}{\longleftrightarrow} Ni(OH)_2 + X\ NH_3\uparrow \quad (6)$$

*))) = Ultrasound

The experimental procedure is depicted in Figure 11. The Ni precursor was dissolved into deionized water (solution A). Another mixture was obtained by dissolving ammonium citrate tribasic (CIT) in an NH_4OH solution (mixture B). Then, mixture B, was poured into solution A (up to achieve a total solution volume of 50 ml) while applying US and controlling the temperature through a cryothermal bath. The overall reaction times were 90 minutes.

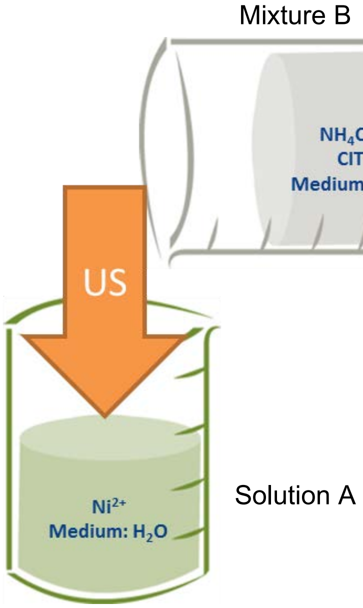

Figure 11. Scheme of the homogeneous synthesis procedure

The XRD pattern of the $Ni(OH)_2$ synthesized is shown in Figure 12 where the pattern corresponds to the α-$Ni(OH)_2$ polymorph (indexed using JCPDS card 22-0444). This abrupt diffractogram is characteristic of a metastable turbostratic phase. The lack of hydroxyl groups within its structure force foreign anions (NO_3^-) to be trapped within the nickel-hydroxyl layers to maintain its electroneutrality forcing the crystallographic disorder. Pure α-$Ni(OH)_2$ was obtained since there are no peaks of any impurity or mixture of products.

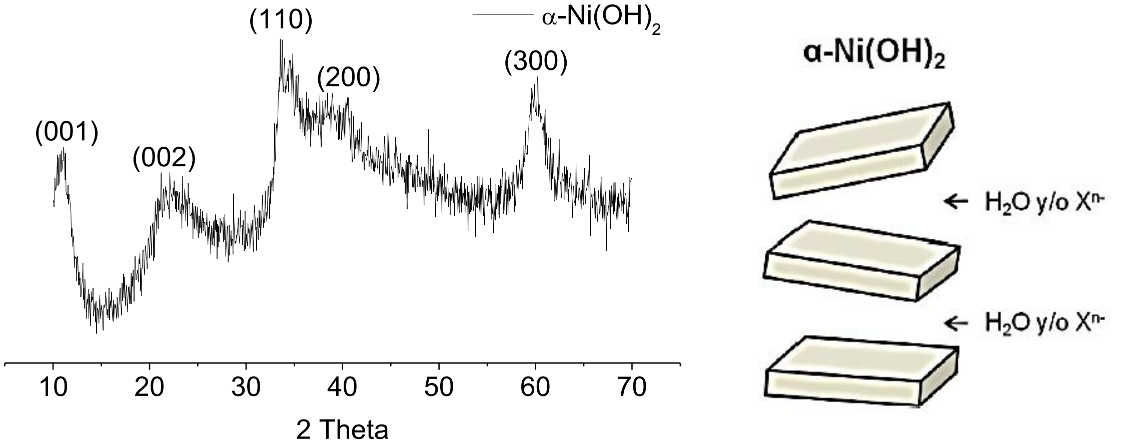

Figure 12. (a) X-Ray Diffraction and (b) Schematic of the distorted structure of the synthesized α-Ni(OH)$_2$ powder.

In Figure 13 (a and b) shows the FESEM micrographs of the resulting powder synthesized. It can be seen that the reaction product consists of an agglomerate (15-20 microns) of small irregular particles, without a clearly defined morphology of between 100 and 200 nm. The low crystallinity observed in the XRD analyses is verified in the HRTEM (Figure 13 c and d) where only the presence of a few stacks of the particles is observed.

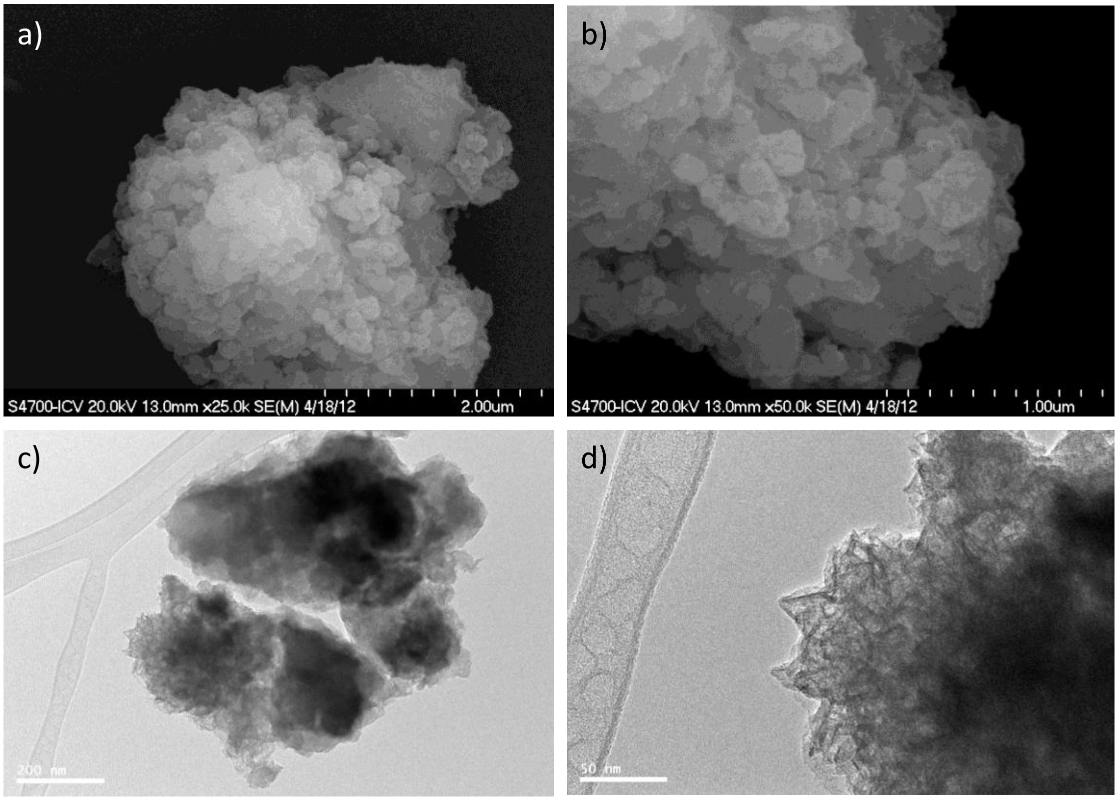

Figure 13. FESEM and HRTEM images of the α-Ni(OH)$_2$ powder synthesized.

The heterogeneous synthesis of core-shell Ti(C,N)-$Ni(OH)_2$ was carried out according to the conditions determined above for the successful homogeneous synthesis. The [Ni^{2+}] was fixed to 4.48M for coating TI(C,N) particles in a 20 vol. % suspension. Optimal conditions include a minimum ratio precursor/precipitant agent 1/5 (1 [Ni^{2+}]: 5 NH_4OH), so the solid content of Ti(C,N) suspension should be limited to 20 vol. %, which assure the minimum volume of liquid necessary for the dissolution of the reactants, in order to process a final 95/5 v/v Ti(C,N)-Ni final composite.

The procedure to synthesize the α-$Ni(OH)_2$ nanoparticles was similar to that used for the homogeneous precipitation described previously. The Ni precursor, was dissolved in the suspension vehicle (DI water) before the Ti(C,N) particles addition. The precipitation of α-$Ni(OH)_2$ NPs were activated by the addition of a mixture of NH_4OH and CIT during the application of US. US were applied with a 100% of the nominal probe power, during 90 min, maintaining the temperature of the suspension below 50 ºC, by external refrigeration with a cryothermal bath.

The microscopy inspection of as-synthesized Ti(C,N)-$Ni(OH)_2$ powders hardly suggests the presence of $Ni(OH)_2$ NPs (Figure 14). Consequently a more accurate study was carried out.

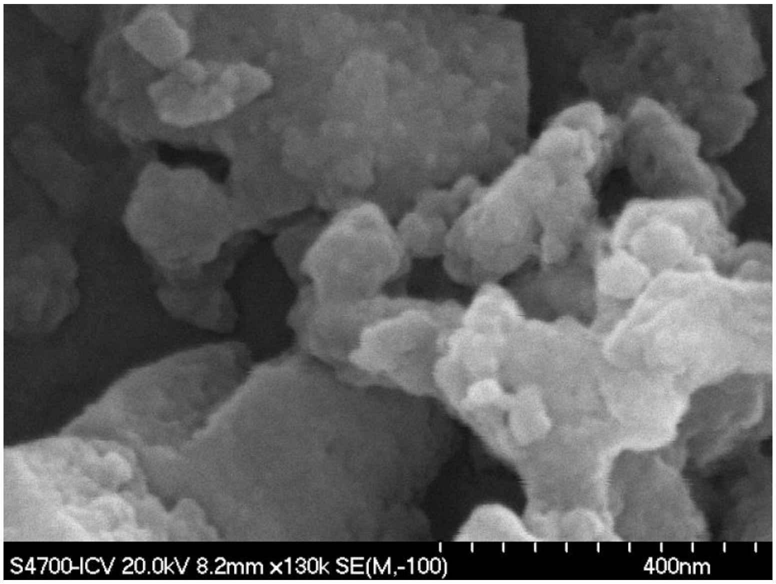

Figure 14. FESEM image of the Ti(C,N)-$Ni(OH)_2$ core-shell structures

Figure 15 shows HRTEM micrographs of resulting Ti(C,N)-$Ni(OH)_2$ core-shell. The micrograph in Figure 15a evidences the presence of a corona of $Ni(OH)_2$ surrounding a Ti(C,N) micrometric particle.

A detailed inspection (Figures 15b, 15c and 15d) reveals small sphere-like α-$Ni(OH)_2$ NPs or nanocrystals of 5 nm in diameter forming a colony onto the TI(C,N) surfaces. Against the preliminar results of this heterogeneous synthesis showed in Figure 5b, these last results evidence the precipitation of $Ni(OH)_2$ onto the Ti(C,N) microparticles, probably as a consequence of the at least an increment of three orders of magnitude the Ni precursor concentration (Table 1). Moreover, the size of the synthesized NPs confirms the role of CIT as complexing agent, which allows maintaining the particle size within the nanometric range with a low polydispersion and high crystallinity (all $Ni(OH)_2$ NPs are similar in size), while linking the NPs to the Ti(C,N) surface (Figure 15d), as reported for the EN plating.

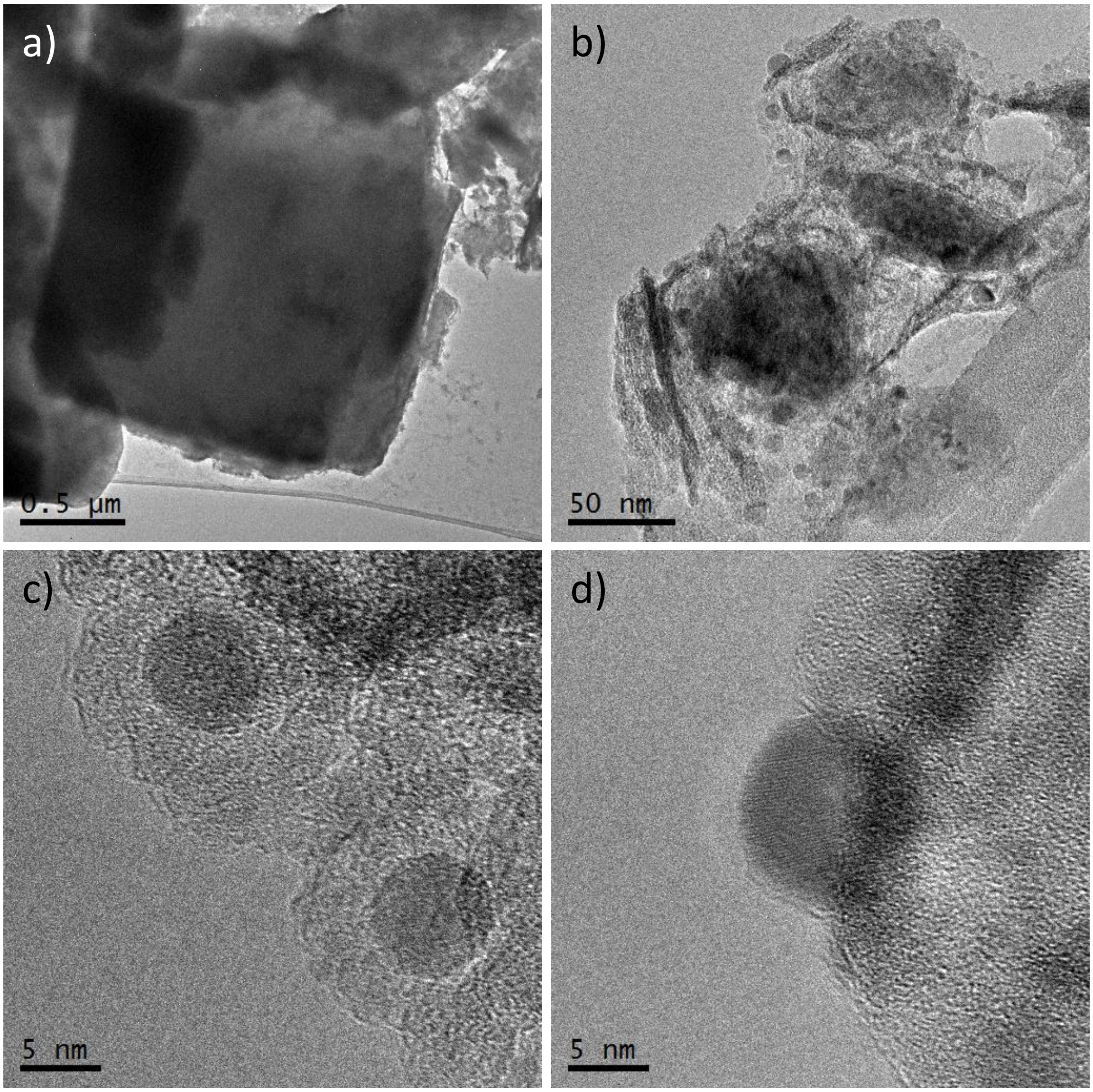

Figure 15. HRTEM images of the Ti(C,N)-Ni(OH)$_2$ core-shell structures

The annealing in reducing atmosphere of the Ti(C,N)-Ni(OH)$_2$ core-shell is mandatory in order to obtain the metallic Ni phase. For that reason, simultaneous Differential Thermal Analysis and Thermogravimetry (DTA-TG) analysis of the as-synthesized powder was carried out in Ar atmosphere to design the calcination cycle and approach the temperature of transformation of Ni(OH)$_2$.

The plot in Figure 16 shows a first wide asymmetric peak (endothermic) between room temperature and 200 ºC, which corresponds to the loss superficially physisorbed and interlamellar water. The mass loss achieved a 4% of the total weight. The second peak (exothermic) in the DTA curve, centered at 275 ºC, is due to the NH_4NO_3 decomposition [151], while a third peak (endothermic), centered at 290 ºC, corresponds to the transformation of α-$Ni(OH)_2$ into NiO. This last process presents a mass loss of nearly 21%, quite close to the theoretical value of 19%. Finally, a small endothermic peak centered at 390ºC, with an associated mass loss of 6% is observed, due to the liberation of NO^{3-} ions occluded within the $Ni(OH)_2$ structure during synthesis [151]. The total mass lost in the thermal annealing of the core-shell nanostructures was about the 30%.

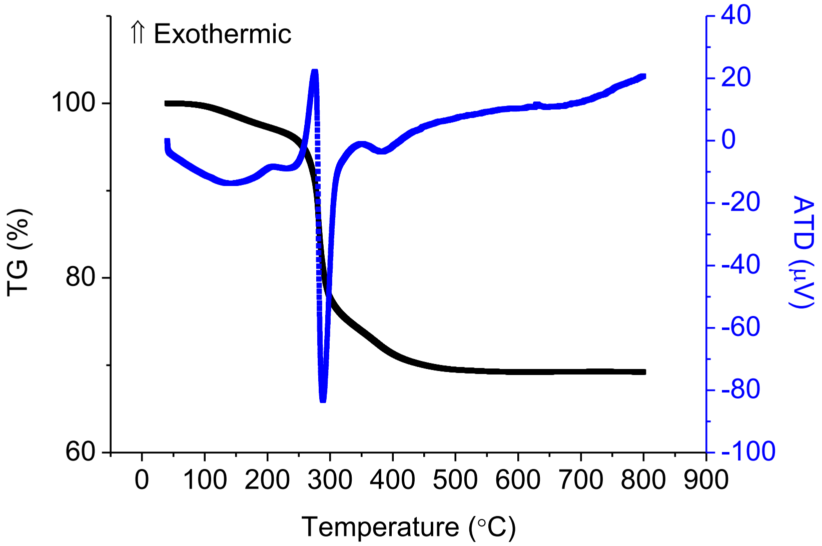

Figure 16. DSC-TGA curve of the homogeneous α-$Ni(OH)_2$ powder synthesized

Based on these findings, we assume a calcination step with a dwell of 30 minutes at 600 ºC in order to ensure the complete elimination of water and the reduction of the $Ni(OH)_2$ to Ni in reducing atmosphere. Figure 17 shows FESEM micrographs of the resulting Ti(C,N)-Ni powder obtained after their annealing in reducing atmosphere (N_2/10%H_2). The micrograph evidence the Ni NPs coarsening, since some of them are now evident on the Ti(C,N) surface of the micrometric particles. Ni NPs have grown up to overpass 100 nm in diameter in some cases. The elemental analysis through EDX corroborate the Ni-based nature of these NPs which achieve after sintering a balance of about 5%, fitting the final cermet composition of 95/5 v/v of Ti(C,N)-Ni.

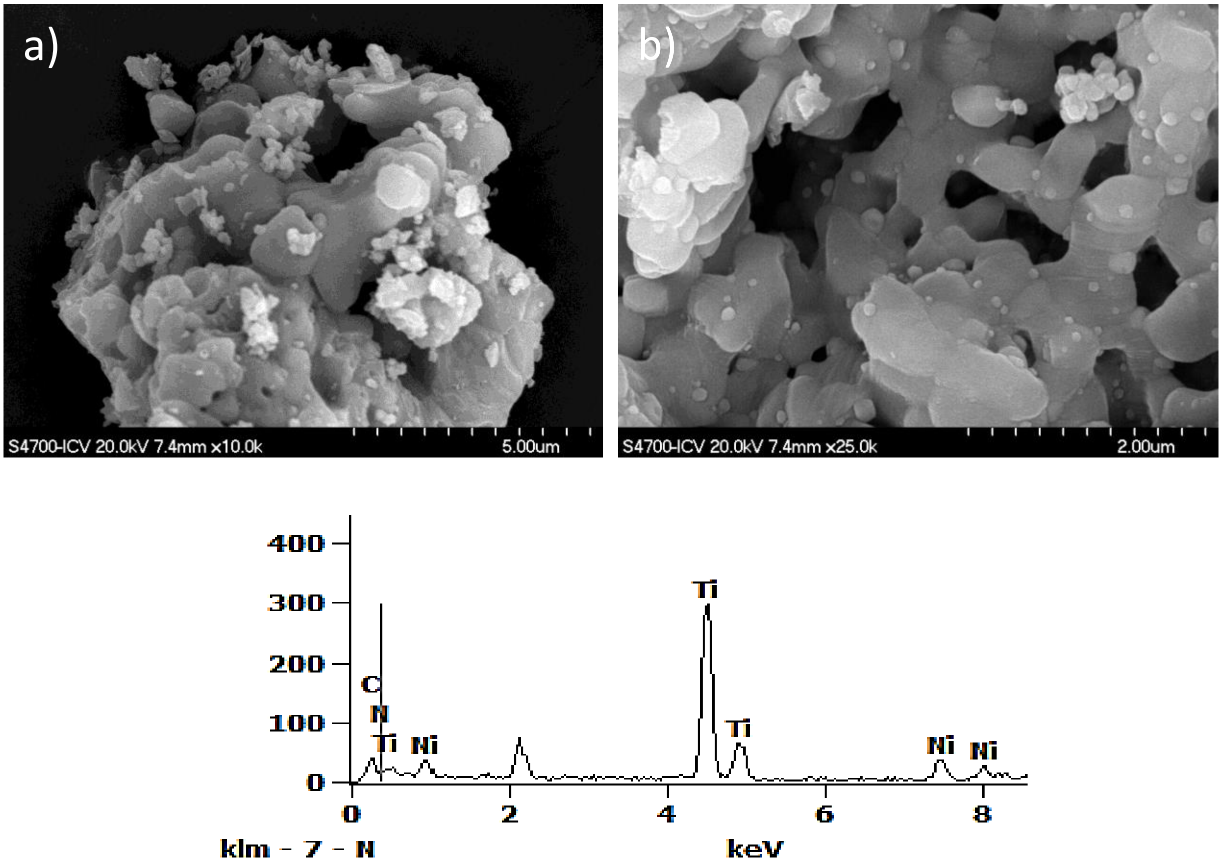

Figure 17. FESEM and EDX analysis of synthesized Ti(C,N)-$Ni(OH)_2$ powder after the calcination cycle

Design of nanostructured Ti(C,N)-Ni bulk materials

In order to shape Ti(C,N)-Ni cermets after the in-situ synthesis of Ni-based species, Ti(C,N)-Ni and Ti(C,N)-$Ni(OH)_2$ suspensions were directly casted in Plaster-of-Paris molds. The formulation of the suspensions and the related cermet compositions for both syntheses are summarized in Table 3. After drying, green casted specimens were sintered at 1450 ºC for 60 min in vacuum (10^{-5} mbar). All thermal treatments included a dwell at 600 °C for 30 min. The green density of the initial samples was 67 % of the theoretical density determined by the rule of mixtures in both cases.

Table 3. Summary of the formulation of the sonically activated syntheses

	Sonically Activation Route	
	Synthesis by Reduction Ti(C,N)-Ni	**Synthesis by Precipitation Ti(C,N)-$Ni(OH)_2$**
Ti(C,N)/Ni	96/4 v/v	95/5 v/v
Ti(C,N)	3 vol. %	20 vol. %
Precursor	0.38 M $Ni(NO_3)_2{\cdot}6H_2O$	4.48 M $Ni(NO_3)_2{\cdot}6H_2O$
Reductant	22.80 M Hydrazine	---
Complexing agent	---	0.11 mM Ammonium Citrate
pH adjust	3.80 M KOH	65 mM NH_4OH
Volume	50 mL	50 mL

Figure 18 shows the SEM micrographs of the prepared materials. EDX analyses were also used to characterize the final composition of Ti(C,N)-Ni pieces. Both micrographs show the presence of two phases. The white phase corresponds to the metallic phase, Ni, and the grey phase corresponds to the ceramic phase, Ti(C,N). The inspection of the microstructure evidences the porosity of the bulk piece due to the low solid content of the initial suspension (~ 3 vol. % and ~ 20 vol. % in the reductant and precipitant routes respectively). In colloidal processing, solid concentrations lower than 30 vol. % does not use to be considered to process dense part by slip casting [93]. Results are quite diverse depending on the area of the analysis and even on the synthesis procedure (N_2H_4 or NH_4OH).

Results from a wide exploration of each microstructure assign the composition 96.5/3.5 v/v to the composite synthesized by reduction and 95/5 v/v to the composite synthesized by precipitation.

The composition of the samples obtained by the precipitation of $Ni(OH)_2$ approaches better the ceramic/metal balance formulated as the starting composition of the composite, which is 96/4 v/v for the Ti(C,N)-Ni and 95/5 v/v for the Ti(C,N)-$Ni(OH)_2$.

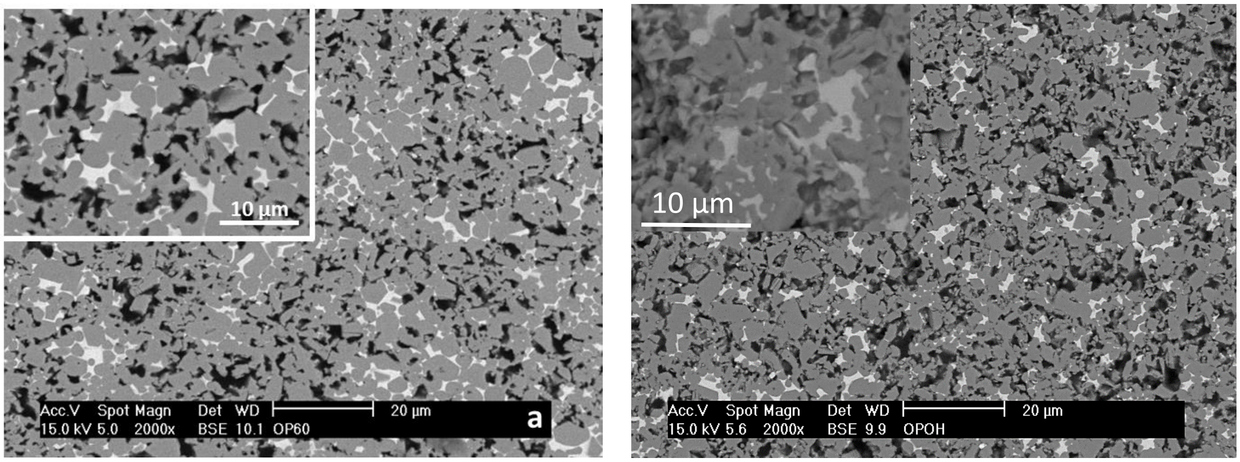

Reductant Route Precipitant Route

Figure 18. SEM micrographs of the Ti(C,N)-Ni bulk materials processed through Slip Casting from (a) reductant and (b) precipitant routes.

Figure 19 shows a detail of the microstructure of the 4Ni60Hz composite and the Raman spectra collected at the bulk grain (A) and at the grain boundary (B), as well as that corresponding to a 100% Ti(C,N) sample processed under similar conditions that the composites (C), and used as reference. For sake of comparison, the Raman spectra were collected using the same laser power (10mW) and surface Raman images of 50 x 30 μm. In order to evaluate the effect of Ni content in different areas of our material, we have focused the Raman spectra in a specific region where the vibrational modes of Ti(C,N) appear (from 215 to 300 cm^{-1}). The spectrum corresponding to the as-received Ti(C,N) powder is characterized by a monomodal spectrum centered in 270 cm^{-1}, which can be attributed to a Ti(C,N) ternary compound with a high content of C [199]. This peak shifts to lower frequencies in the composite, and a new feature (shoulder) appears in both spectra, at 255 cm^{-1} in that collected at the bulk grain (A) of the microstructure and at 250 cm^{-1} for the spectrum collected at the boundary grain (B). The observed slight position shift of this phonon mode can be attributed to a minor decrease of carbon content in the FCC Ti(C,N) phase in the composite. However, the new shoulder in both spectra evidences different local arrangements due to the presence of Ni in the Ti(C,N) lattice. The effect intensifies at the grain boundary, where the presence of Ni increases. Consequently, local Raman analyses suggest the solution of the Ni NPs in the Ti(C,N) lattice.

So, despite the density of the final composite, the obtained results allows to argue that the sintering process was activated by reducing down to the nanometric size the binder, achieving the Ni solution in the Ti(C,N) lattice. The increment of the surface of reaction with the nanosized metal phase, not only improves the liquid phase distribution among Ti(C,N) particles, but also promote the chemical anchoring with the Ti(C,N) reinforcement phase. Consequently, although the presence of heterogeneities, both microstructures appears well consolidated contrasting with the low amount of Ni (≤ 5 vol. %) in the composite. Moreover the distribution of the nanometric metal phase leads to a finer microstructure, if compare with materials shaped by slip casting of high concentrated suspensions of a micrometric commercial powders.

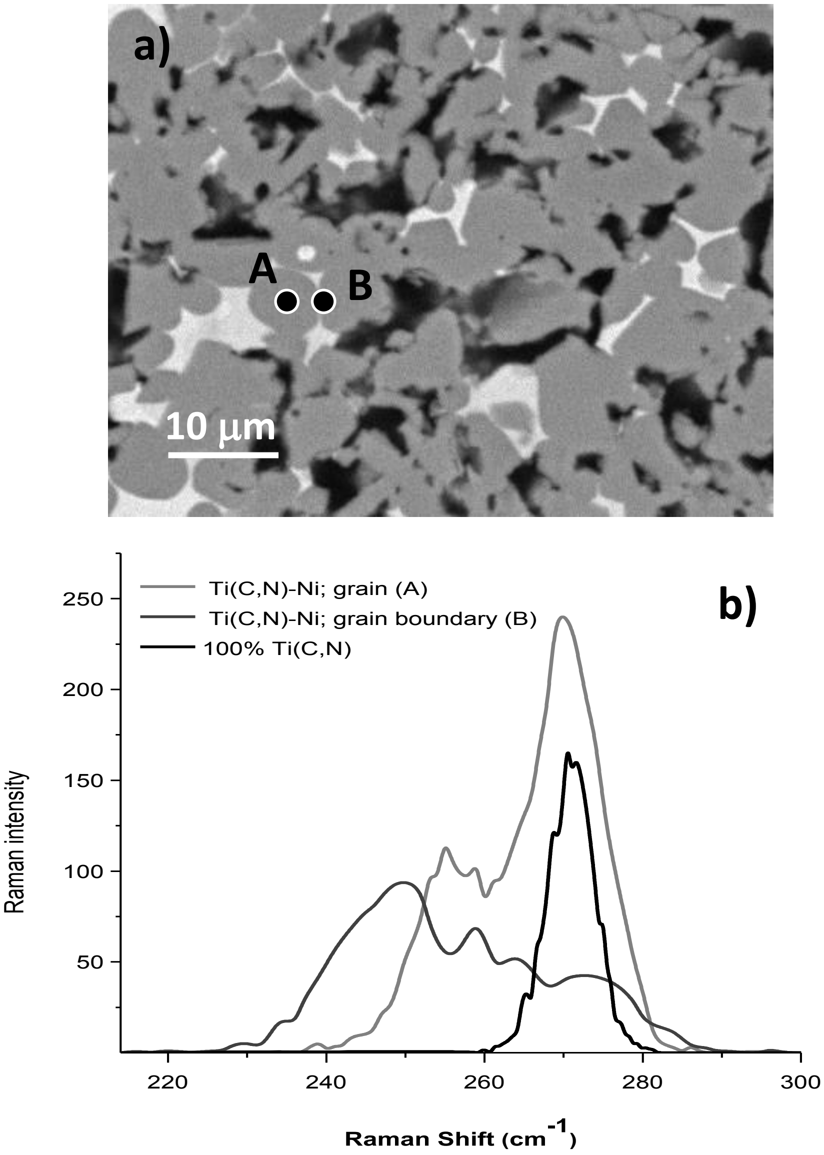

Figure 19. (a) SEM micrograph of 4Ni60Hz Ti(C,N)-Ni particles and (b) Raman spectra of (A) bulk grain, (B) boundary grain and (C) as-received Ti(C,N) particles (not shown).

The details of experimental procedure, the complete results and discussion is published in: [Paper 7 to 11]

Chapter 4

Concluding Remarks

The inspection of the wetting behavior of Fe, Ni and Fe-15Ni on Ti(C,N) sintered substrates supports the potential use of the Fe-15Ni alloy (FeNi) as metal binder in Ti(C,N)-based cermets. From the analysis of the interfaces at high temperature we can conclude that:

- The high wettability of Ni on Ti(C,N) (θ = 10°) is mainly due to the solubility of Ti(C,N) in liquid Ni. Ni melts and dissolves Ti(C,N) soaking the Ti(C,N) grains and improving joining.
- Fe wettability slightly improves (θ = 64º) for residence time of 550 s when the solubility of Ti(C,N) in melted Fe increases.
- FeNi (with a 15 wt. % of Ni) largely increases the solubility of Ti(C,N), if compare with the 100% Fe binder, and then the contact angle between the two phases.

Considering these evidences, two colloidal approaches were successfully explored to evaluate processability and final performance of Ti(C,N)-FeNi cermets: (i) the implementation of the colloidal mixture of raw powders (Ti(C,N), Fe and Ni) in the powder metallurgy process of shaping, and (ii) the incorporation of metallic nanophases, concluding that:

The use of colloidal mixtures of monophasic powders combined with powder metallurgy provides a new route for the processing of Ti(C,N)-based cermets that allows obtaining homogeneous microstructures, and near full dense materials with high fractions of ceramic phase (up to 85 vol. %) properly distributed in the metallic matrix. The proposed route provides reliable results expanding the range of possibilities of processing bulk pieces from slurries of metal and nonoxides particle mixtures.

Among the explored shaping methods, SDP cermets reach densities of 99.9%. The spray-dry of stable aqueous slurries with a high solid content yield solid and spherical composites granules, where the metal and the ceramic particles are homogeneously distributed. Those granules exhibit a high compressibility enabling their processing by conventional powder metallurgy (uniaxial pressing and vacuum sintering). Monophasic slurries of micrometric Fe, Ni and Ti(C,N) powders were dispersed under similar chemical and colloidal conditions to assure their stability and the mixture compatibility. Through rheological studies, stable aqueous high solid content suspensions of Ti(C,N) (45 vol. %) and Fe/Ni (35 vol. %) were formulated. Then, those suspensions were mixed in order to obtain the desired final composition of the cermet (85/15 vol. % Ti(C,N)-FeNi). The rheological behavior of this final suspension fits the conditions to be processed by SC as well as by SDP (region from 150 to 100 s-1).The high dispersion of phases in the slurry replicates in the granules, leading to highly dense, homogeneous and fine microstructures after shaping and sintering.

The sintering cycle was optimized to control the cermet composition, reducing the N_2 lability, the final O_2 content (<0.2 to wt. %) and the Ni sublimation. In this sense, a sintering time as short as 120 min at 1450 ˚C in vacuum was adjusted, to provide equilibrium between densification and composition matching the initially designed formulation.

Hardness values determined for 80-85 wt. % Ti(C,N) materials processed by the proposed low energetic route are in the range of those reported in the literature for Ti(C,N)-based materials prepared by SPS or high energetic milling using carbides and 100% Ni matrix. Moreover, the addition of C to the cermet formulation promotes the microstructure hardening evidencing the key role of wettability and solubility of the well distributed phases in the microstructure features.

The structural characterization of processed Ti(C,N)-FeNi cermets leads to major conclusions such as follows:

+ Considerably improved biaxial strength was observed in the samples obtained through SDP when compared to other techniques such as SC and SC-CIP, due to the increase of density of sintered specimens (from 92.2% to 99.0%). Comparing the biaxial strength of the different cermets investigated, it was found that the difference in strength is determined by the remnant porosity obtained depending on the processing method.

+ The addition of a higher amount of metal binder (from 15 vol. % to 20 vol. %) improved the biaxial strength (from ~1530 to ~1870 MPa with carbon addition).

+ The addition of 0.5 wt. % of carbon with respect to the weight of matrix enhances the rearrangement of Ti(C,N) particles during liquid-phase sintering and then their densification after the thermal process. The designed cermet processing and formulation generates a homogeneous distribution of Ti(C,N) within the microstructure, which promotes the trans-granular fracture of the specimens. The addition of carbon increases the fracture toughness, being this effect more evident in the cermets processed with a higher proportion of metal binder (20FeNiC).

+ The SDP 20FeNiC cermet exhibits enhanced mechanical properties with a biaxial strength of 1867 [1832 – 1903] MPa, a fracture toughness of 13.8 ± 0.2 $\text{MPa}\cdot\text{m}^{1/2}$ and a work-of-fracture of 1720 ± 105 J/m^2, being the best composite candidates to improve the mechanical performance of the proposed Ti(C,N)-based cermets meeting the requirements for tool materials. It may be presumed that the ceramic contiguity is deleterious for biaxial strength and fracture toughness of Ti(C,N)-based cermets.

+ Preliminary results of the micro- and nanomechanical study leads to a maximum penetration depth of 200 nm as suitable testing parameter to attain a successful implementation of the statistical method in Ti(C,N)-FeNi systems.

+ Under these conditions, massive nanoindentation and statistical analysis reveals the isotropic behavior regarding hardness of the Ti(C,N) phase, while the estimated flow stress for the metallic FeNi binder ranges between 3.50-4.66 GPa. Moreover nanomechanics verifies that hardness and elastic modulus of Ti(C,N)-FeNi composite decrease when the volume fraction of the metallic binder increases.

For the incorporation of metallic nanophases in the Ti(C,N)-FeNi composite, chemical and ultrasound activation of Ni NPs syntheses have been optimized, concluding that:

The proposed electroless Ni (EN) platting procedure to coat Ti(C,N) leads to the formation of crystalline Ni NPs of 20 nm in a continuous corona surrounding Ti(C,N) particles, where the use of DMAB as reducing agent avoids impurities on the Ni layer. Citrate (CIT) is used as complexing agent to prevent the aggregation of the NPs, but also results in an effective stabilizer of the Ti(C,N) micrometric particles in the EN solution during mixing and plating procedures. Lactic acid (LA) is used as a chemical buffer which allows the homogenization of the electroless plating bath and, with CIT, they act as ligands between the Ti(C,N) particles and the synthesized Ni NPs, thanks to the carboxylic groups grafted on the ceramic surface. Also according to this work, pre-treatments of micrometric particles are key steps of the process, since it determines the density of the Ni NPs layer on Ti(C,N) surface. However, the pre-treatments limits the Ti(C,N) concentration of the suspension, compromising the application of this route to the massive preparation of Ti(C,N)-reinforced composites.

Both, the heterogeneous Ni reduction and $Ni(OH)_2$ precipitation onto surface of Ti(C,N) particles, designed for the one pot processing of Ti(C,N)/Ni composites, were successfully achieved. A low concentration of metal binder (<5 vol. %) wraps up the ceramic structure leading to a promising microstructure with homogenous and finer distribution of phases, as well as smaller amount of metallic phase.

The optimum conditions of the Ni NPs reductive synthesis include amonimum ratio precursor/hydrazine (~1/60) to provide a homogenous distribution of the metal phase in the microstructure. However, the wide size distribution of the micrometric ceramic particles lacks the metal matrix uniformity, because of the fine fraction of powders provides preferential sites for Ni nucleation. Ni NPs precipitate onto Ti(C,N) surfaces taking in flower and flakes-like morphologies depending on the solid content of the suspension (amount of Ti(C,N) particles) and the precursor concentration (amount of Ni^{2+}). Ni nanopetals have a diameter of 20 nm and a thickness of 2–4 nm, while flower-like particles have 100 nm of diameter. In all cases Ni surrounds Ti(C,N) particles forming a core-shell structure. The particle size of as-synthesized Ni decreases with the S parameter [W/(mol/L)s], while the concentration of Ni^{2+} and the related amount of hydrazine has on each thresholds in order to produce Ni NPs under described US conditions.

The optimal conditions for the heterogeneous precipitation of α-$Ni(OH)_2$ NPs surrounding Ti(C,N) in aqueous suspension have been also successfully stablished. In this synthesis, CIT also plays a double role as synthesis modifier, extremely relevant to produce spherical and well dispersed $Ni(OH)_2$ NPs, disrupting the regular flakes-like growth of this compound in aqueous media.

In the sonically activated syntheses, the solubility of precursors and reactants could limit the yield production of Ni NPs, but it permits to locally introduce a Ni nanophase in Ti(C,N) surface, and provides a new bottom-up approach to process Ti(C,N)-FeNi cermets with improved properties.

References

[1] X.. Li, Ceramic cutting tools: an introduction, Key Eng Mater. 96 (1994) 1–18.

[2] Mitsubishi materials. Cutting tools materials. [Consulta 02/10/2017] Disponible en: http://www.mitsubishicarbide.net/contents/mmus/enus/html/product/technical_information/information/sessaku.html, (2017).

[3] A. Senthil Kumar, A. Raja Durai, T. Sornakumar, The effect of tool wear on tool life of alumina-based ceramic cutting tools while machining hardened martensitic stainless steel, J. Mater. Process. Technol. 173 (2006) 151–156. doi:10.1016/j.jmatprotec.2005.11.012.

[4] Y. Cheng, Y. Zhang, T. Wan, Z. Yin, J. Wang, Mechanical properties and toughening mechanisms of graphene platelets reinforced Al 2 O 3 /TiC composite ceramic tool materials by microwave sintering, Mater. Sci. Eng. A. 680 (2017) 190–196. doi:10.1016/j.msea.2016.10.100.

[5] Y.M.Z. Ahmed, Z.I. Zaki, D.H.A. Besisa, A.M.M. Amin, R.K. Bordia, Effect of zirconia and iron on the mechanical properties of Al2O3/TiC composites processed using combined self-propagating synthesis and direct consolidation technique, Mater. Sci. Eng. A. 696 (2017) 182–189. doi:10.1016/j.msea.2017.04.059.

[6] Z. Yin, C. Huang, J. Yuan, B. Zou, H. Liu, H. Zhu, Cutting performance and life prediction of an Al2O3/TiC micro–nano-composite ceramic tool when machining austenitic stainless steel, Ceram. Int. 41 (2015) 7059–7065. doi:10.1016/j.ceramint.2015.02.012.

[7] S. Grigoriev, P. Peretyagin, A. Smirnov, W. Solís, L.A. Díaz, A. Fernández, R. Torrecillas, Effect of graphene addition on the mechanical and electrical properties of Al 2 O 3 -SiCw ceramics, J. Eur. Ceram. Soc. 37 (2017) 2473–2479. doi:10.1016/j.jeurceramsoc.2017.01.027.

[8] R.M. Bock, B.J. McEntire, B.S. Bal, M.N. Rahaman, M. Boffelli, G. Pezzotti, Surface modulation of silicon nitride ceramics for orthopaedic applications, Acta Biomater. 26 (2015) 318–330. doi:10.1016/j.actbio.2015.08.014.

[9] G. Ling, H. Yang, Pressureless sintering of silicon nitride with Magnesia and Yttria, Mater. Chem. Phys. 90 (2005) 31–34. doi:10.1016/j.matchemphys.2004.08.041.

[10] M.M. Opeka, I.G. Talmy, E.J. Wuchina, J.A. Zaykoski, S.J. Causey, Mechanical,

Thermal, and Oxidation Properties of Refractory Hafnium and zirconium Compounds, J. Eur. Ceram. Soc. 19 (1999) 2405–2414. doi:10.1016/S0955-2219(99)00129-6.

[11] W.G. Fahrenholtz, G.E. Hilmas, I.G. Talmy, J.A. Zaykoski, Refractory diborides of zirconium and hafnium, J. Am. Ceram. Soc. 90 (2007) 1347–1364.

[12] W.-W. Wu, G.-J. Zhang, Y.-M. Kan, P.-L. Wang, Reactive Hot Pressing of ZrB2-SiC-ZrC Composites at 1600°C, J. Am. Ceram. Soc. 91 (2008) 2501–2508. doi:10.1111/j.1551-2916.2008.02507.x.

[13] W.-W. Wu, G.-J. Zhang, Y.-M. Kan, P.-L. Wang, K. Vanmeensel, J. Vleugels, O. Van der Biest, Synthesis and microstructural features of ZrB2–SiC-based composites by reactive spark plasma sintering and reactive hot pressing, Scr. Mater. 57 (2007) 317–320. doi:10.1016/j.scriptamat.2007.04.025.

[14] X.-J. Zhou, G.-J. Zhang, Y.-G. Li, Y.-M. Kan, P.-L. Wang, Hot pressed ZrB2–SiC–C ultra high temperature ceramics with polycarbosilane as a precursor, Mater. Lett. 61 (2007) 960–963. doi:10.1016/j.matlet.2006.06.024.

[15] S.M. Sicker, V.N. Antonov, V.P. Antropov, Comparative study of the electronic structure, phonon spectra, and electron-phonon interaction of ZrB2 and TiB2, Phys. Rev. B. 87 (2013). doi:10.1103/PhysRevB.87.064305.

[16] R. Savino, M. De Stefano Fumo, L. Silvestroni, D. Sciti, Arc-jet testing on HfB2 and HfC-based ultra-high temperature ceramic materials, J. Eur. Ceram. Soc. 28 (2008) 1899–1907. doi:10.1016/j.jeurceramsoc.2007.11.021.

[17] Y. Yuan, J.-X. Liu, G.-J. Zhang, Effect of HfC and SiC on microstructure and mechanical properties of HfB2-based ceramics, Ceram. Int. 42 (2016) 7861–7867. doi:10.1016/j.ceramint.2016.01.067.

[18] K. Schröter, DRP 420.689: sintered hard metal alloy and procedure for its fabrication, US1549615, 1923.

[19] K. Brookes, There's more to hard materials than tungsten carbide alone, Met. Powder Rep. 66 (2011) 36–45. doi:10.1016/S0026-0657(11)70062-5.

[20] C.M. Fernandes, A.M.R. Senos, Cemented carbide phase diagrams: A review, Int. J. Refract. Met. Hard Mater. 29 (2011) 405–418. doi:10.1016/j.ijrmhm.2011.02.004.

[21] S.I. Cha, S.H. Hong, G.H. Ha, B.K. Kim, Mechanical properties of WC–10Co cemented carbides sintered from nanocrystalline spray conversion processed powders, Int. J. Refract. Met. Hard Mater. 19 (2001) 397–403. doi:10.1016/S0263-4368(01)00057-9.

[22] K.J.A. Brookes, Powdermet 2016 conference: Pride of place for sintered carbides, Met. Powder Rep. 71 (2016) 416–425. doi:10.1016/J.MPRP.2016.06.065.

[23] W. SU, Y. SUN, H. YANG, X. ZHANG, J. RUAN, Effects of TaC on microstructure and mechanical properties of coarse grained WC–9Co cemented carbides, Trans. Nonferrous Met. Soc. China. 25 (2015) 1194–1199. doi:10.1016/S1003-6326(15)63715-3.

[24] S.-H. Chang, P.-Y. Chang, Investigation into the sintered behavior and properties of nanostructured WC–Co–Ni–Fe hard metal alloys, Mater. Sci. Eng. A. 606 (2014) 150–156. doi:10.1016/j.msea.2014.03.096.

[25] S.-H. Chang, S.-L. Chen, Characterization and properties of sintered WC–Co and WC–Ni–Fe hard metal alloys, J. Alloys Compd. 585 (2014) 407–413. doi:10.1016/j.jallcom.2013.09.188.

[26] W. Su, Y. Sun, J. Liu, J. Feng, J. Ruan, Effects of Ni on the microstructures and properties of WC–6Co cemented carbides fabricated by WC–6(Co, Ni) composite powders, Ceram. Int. 41 (2015) 3169–3177. doi:10.1016/j.ceramint.2014.10.165.

[27] X. Zhang, J. Zhou, N. Lin, K. Li, K. Fu, B. Huang, Y. He, Effects of Ni addition and cyclic sintering on microstructure and mechanical properties of coarse grained WC–10Co cemented carbides, Int. J. Refract. Met. Hard Mater. 57 (2016) 64–69. doi:10.1016/j.ijrmhm.2016.02.008.

[28] J.M. Tarragó, J.J. Roa, V. Valle, J.M. Marshall, L. Llanes, Fracture and fatigue behavior of WC–Co and WC–CoNi cemented carbides, Int. J. Refract. Met. Hard Mater. 49 (2015) 184–191. doi:10.1016/j.ijrmhm.2014.07.027.

[29] T.W. Penrice, Some characteristics of the binder phase in cemented carbides, Int. J. Refract. Met. Hard Mater. 15 (1997) 113–121. doi:10.1016/S0263-4368(97)81232-2.

[30] M. Mahmoodan, H. Aliakbarzadeh, R. Gholamipour, Microstructural and mechanical characterization of high energy ball milled and sintered WC–10wt%Co–xTaC nano

powders, Int. J. Refract. Met. Hard Mater. 27 (2009) 801–805. doi:10.1016/j.ijrmhm.2009.02.001.

[31] N. Lin, Y. He, J. Zou, Enhanced mechanical properties and oxidation resistance of tungsten carbide-cobalt cemented carbides with aluminum nitride additions, Ceram. Int. 43 (2017) 6603–6606. doi:10.1016/j.ceramint.2017.01.145.

[32] W. Qiu, Y. Liu, J. Ye, H. Fan, Y. Qiu, Effects of (Ti,Ta,Nb,W)(C,N) on the microstructure, mechanical properties and corrosion behaviors of WC-Co cemented carbides, Ceram. Int. 43 (2017) 2918–2926. doi:10.1016/j.ceramint.2016.09.124.

[33] T.A. Fabijanić, Ž. Alar, D. Ćorić, Influence of consolidation process and sintering temperature on microstructure and mechanical properties of near nano- and nano-structured WC-Co cemented carbides, Int. J. Refract. Met. Hard Mater. 54 (2016) 82–89. doi:10.1016/j.ijrmhm.2015.07.017.

[34] P. SIWAK, D. GARBIEC, Microstructure and mechanical properties of WC–Co, WC–Co–Cr3C2 and WC–Co–TaC cermets fabricated by spark plasma sintering, Trans. Nonferrous Met. Soc. China. 26 (2016) 2641–2646. doi:10.1016/S1003-6326(16)64390-X.

[35] D. Lison, R. Lauwerys, The interaction of cobalt metal with different carbides and other mineral particles on mouse peritoneal macrophages, Toxicol. Vitr. 9 (1995) 341–347. doi:10.1016/0887-2333(94)00211-C.

[36] National Toxicology Program. Department of health and human services., (2012). https://ntp.niehs.nih.gov/pubhealth/roc/index-1.html.

[37] S. Norgren, J. García, A. Blomqvist, L. Yin, Trends in the P/M hard metal industry, Int. J. Refract. Met. Hard Mater. 48 (2015) 31–45. doi:10.1016/J.IJRMHM.2014.07.007.

[38] G. Gille, J. Bredthauer, B. Gries, B. Mende, W. Heinrich, Advanced and new grades of WC and binder powder – their properties and application, Int. J. Refract. Met. Hard Mater. 18 (2000) 87–102. doi:10.1016/S0263-4368(00)00002-0.

[39] W.D. Schubert, M. Fugger, B. Wittmann, R. Useldinger, Aspects of sintering of cemented carbides with Fe-based binders, Int. J. Refract. Met. Hard Mater. 49 (2015) 110–123. doi:10.1016/J.IJRMHM.2014.07.028.

[40] P. Ettmayer, H. Kolaska, W. Lengauer, K. Dreyer, Ti(C,N) cermets - Metallurgy and properties, Int. J. Refract. Met. Hard Mater. (1995). doi:10.1016/0263-4368(95)00027-G.

[41] L. Chen, W. Lengauer, K. Dreyer, Advances in modern nitrogen-containing hardmetals and cermets, Int. J. Refract. Met. Hard Mater. 18 (2000) 153–161. doi:10.1016/S0263-4368(00)00016-0.

[42] Y. Peng, H. Miao, Z. Peng, Development of TiCN-based cermets: Mechanical properties and wear mechanism, Int. J. Refract. Met. Hard Mater. 39 (2013) 78–89. doi:10.1016/j.ijrmhm.2012.07.001.

[43] G. Levi, W.D. Kaplan, M. Bamberger, Structure refinement of titanium carbonitride (TiCN), Mater. Lett. 35 (1998) 344–350. doi:10.1016/S0167-577X(97)00276-0.

[44] Fried Krupp AG, French Patent 715148, 1931.

[45] R. Kieffer, P. Ettmayer, M. Freudhofmeier, About Nitrides and Carbonitrides and Nitride-Based Cemented Hard Alloys, in: H.H. Hausner (Ed.), Mod. Dev. Powder Metall. Vol. 5 Mater. Prop. Proc. 1970 Int. Powder Metall. Conf. Spons. by Met. Power Ind. Fed. Am. Powder Metall. Inst., Springer US, Boston, MA, 1971: pp. 201–214. doi:10.1007/978-1-4615-8963-1_15.

[46] J. Russias, S. Cardinal, Y. Aguni, G. Fantozzi, K. Bienvenu, J. Fontaine, Influence of titanium nitride addition on the microstructure and mechanical properties of TiC-based cermets, Int. J. Refract. Met. Hard Mater. 23 (2005) 358–362. doi:10.1016/j.ijrmhm.2005.05.008.

[47] J.H. Xiao, W.H. Xiong, S.J. Lin, J. Qu, M. Zhou, Review on the preparation and application of Ti(C,N)-based cermet composite, Mater Rev. (2010) 21–27.

[48] X.T. Kang, S.Y. Liu, J.L. Jiang, Manufacture and application of Ti(C,N) matrix cermet, Cem. Carbide. (1999) 51–55.

[49] Y.D. Xu, N. Liu, Q. Zeng, H. Li, M. Shi, Wear properties of nano TiN modified cermets cutters, Cem. Carbide. (2001) 142–145.

[50] Q. Xu, X.H. Zhang, W. Qu, J.C. Han, Progress in research on cermets, Cem. Carbide. (2002) 221–225.

[51] Y.D. Xu, N. Liu, M. Shi, S. Chao, Research progress of TiCN cermets with nano modification, Cem. Carbide. (2005) 112–116.

[52] W. Li, D. Gu, X. Shu, H. Zhang, Z. Li, Corrosion resistance of Ti(C,N)-based cermet for surgical cutting tools, Powder Met. Technol. (2002) 82–85.

[53] F. Velasco, R. Isabel, N. Antón, M.A. Martínez, J.M. Torralba, TiCN—high speed steel composites: sinterability and properties, Compos. Part A Appl. Sci. Manuf. 33 (2002) 819–827. doi:10.1016/S1359-835X(02)00024-6.

[54] J.A. Escribano, J.L. García, P. Alvaredo, B. Ferrari, E. Gordo, A.J. Sanchez-Herencia, FGM stainless steel-Ti(C,N) cermets through colloidal processing, Int. J. Refract. Met. Hard Mater. 49 (2014) 143–152. doi:10.1016/j.ijrmhm.2014.05.008.

[55] H. Yang, S. Roberts, Gas pressure sintering of Al2O3/TiCN composite, Ceram. Int. 31 (2005) 1073–1076. doi:10.1016/j.ceramint.2004.11.007.

[56] E.T. Jeon, J. Joardar, S. Kang, Microstructure and tribo-mechanical properties of ultrafine Ti(CN) cermets, Int. J. Refract. Met. Hard Mater. 20 (2002) 207–211. doi:10.1016/S0263-4368(02)00004-5.

[57] J. Joardar, S.W. Kim, S. Kang, Effect of nanocrystalline binder on the microstructure and mechanical properties of ultrafine Ti(CN) cermets, Mater. Sci. Eng. A. 360 (2003) 385–389. doi:10.1016/S0921-5093(03)00506-9.

[58] S. Park, S. Kang, Toughened ultra-fine (Ti,W)(CN)–Ni cermets, Scr. Mater. 52 (2005) 129–133. doi:10.1016/j.scriptamat.2004.09.017.

[59] S. Cardinal, a. Malchère, V. Garnier, G. Fantozzi, Microstructure and mechanical properties of TiC-TiN based cermets for tools application, Int. J. Refract. Met. Hard Mater. 27 (2009) 521–527. doi:10.1016/j.ijrmhm.2008.10.006.

[60] M. Naidoo, O. Johnson, I. Sigalas, M. Herrmann, Influence of tantalum on the microstructure and properties of Ti(C,N)-Ni cermets, Int. J. Refract. Met. Hard Mater. 42 (2014) 97–102. doi:10.1016/j.ijrmhm.2013.08.008.

[61] Q. Yang, W. Xiong, M. Zhang, B. Huang, S. Chen, Microstructure and mechanical properties of Mo-free Ti(C,N)-based cermets with Ni–xCr binders, J. Alloys Compd. 636 (2015) 270–274. doi:10.1016/j.jallcom.2014.11.236.

[62] J.M. Córdoba, E. Chicardi, R. Poyato, F.J. Gotor, V. Medri, S. Guicciardi, C. Melandri, Spark plasma sintering of TixTa1−xC0.5N0.5-based cermets: Effects of processing conditions on chemistry, microstructure and mechanical properties, Chem. Eng. J. 230 (2013) 558–566. doi:10.1016/j.cej.2013.06.104.

[63] E. Chicardi, F.J. Gotor, V. Medri, S. Guicciardi, S. Lascano, J.M. Córdoba, Hot-pressing of (Ti, Mt)(C, N)–Co–Mo 2 C (Mt = Ta, Nb) powdered cermets synthesized by a mechanically induced self-sustaining reaction, Chem. Eng. J. 292 (2016) 51–61. doi:10.1016/j.cej.2016.02.007.

[64] Q. Xu, X. Ai, J. Zhao, F. Gong, J. Pang, Y. Wang, Effects of metal binder on the microstructure and mechanical properties of Ti(C,N)-based cermets, J. Alloys Compd. 644 (2015) 663–672. doi:10.1016/j.jallcom.2015.05.059.

[65] Q. Xu, X. Ai, J. Zhao, W. Qin, Y. Wang, F. Gong, Comparison of Ti(C,N)-based cermets processed by hot-pressing sintering and conventional pressureless sintering, J. Alloys Compd. 619 (2015) 538–543. doi:10.1016/j.jallcom.2014.08.261.

[66] K. Aigner, W. Lengauer, P. Ettmayer, Interactions in iron-based cermet systems, J. Alloys Compd. 262–263 (1997) 486–491. doi:10.1016/S0925-8388(97)00360-5.

[67] E. Gordo, B. Gómez, E.M. Ruiz-Navas, J.M. Torralba, Influence of milling parameters on the manufacturing of Fe-TiCN composite powders, J. Mater. Process. Technol. 162–163 (2005) 59–64. doi:10.1016/j.jmatprotec.2005.02.154.

[68] B. Gómez, E. Gordo, J.M. Torralba, Influence of milling time on the processing of Fe-TiCN composites, Mater. Sci. Eng. A. 430 (2006) 59–63. doi:10.1016/j.msea.2006.05.051.

[69] M. Chen, Q. Zhuang, N. Lin, Y. He, Improvement in microstructure and mechanical properties of Ti(C,N)-Fe cermets with the carbon additions, J. Alloys Compd. 701 (2017) 408–415. doi:10.1016/j.jallcom.2017.01.119.

[70] Z. Guo, J. Xiong, M. Yang, J. Wang, L. Sun, Y. Wu, J. Chen, S. Xiong, Microstructure and properties of Ti(C,N)–Mo2C–Fe cermets, Int. J. Refract. Met. Hard Mater. 27 (2009) 781–783. doi:10.1016/j.ijrmhm.2009.01.003.

[71] J. Xiong, Z. Guo, B. Shen, D. Cao, The effect of WC, Mo2C, TaC content on the microstructure and properties of ultra-fine TiC0.7N0.3 cermet, 2007.

doi:10.1016/j.matdes.2006.03.005.

[72] J. Wang, Y. Liu, P. Zhang, J. Ye, M. Tu, Effect of VC and nano-TiC addition on the microstructure and properties of micrometer grade Ti(CN)-based cermets, Mater. Des. 30 (2009) 2222–2226. doi:10.1016/j.matdes.2008.08.017.

[73] H. Yu, Y. Liu, Y. Jin, J. Ye, Effect of secondary carbides addition on the microstructure and mechanical properties of (Ti, W, Mo, V)(C, N)-based cermets, Int. J. Refract. Met. Hard Mater. 29 (2011) 586–590. doi:10.1016/j.ijrmhm.2011.03.013.

[74] E. Chicardi, Y. Torres, M.J. Sayagués, V. Medri, C. Melandri, J.M. Córdoba, F.J. Gotor, Toughening of complete solid solution cermets by graphite addition, Chem. Eng. J. 267 (2015) 297–305. doi:10.1016/j.cej.2015.01.022.

[75] P. Alvaredo, J.J. Roa, E. Jiménez-Pique, L. Llanes, E. Gordo, Characterization of interfaces between TiCN and iron-base binders, Int. J. Refract. Met. Hard Mater. 63 (2017) 32–37. doi:10.1016/j.ijrmhm.2016.08.010.

[76] S. Acharya, M. Debata, T.S. Acharya, P.P. Acharya, S.K. Singh, Influence of nickel boride addition on sintering behaviour and mechanical properties of TiC–Ni based cermets, J. Alloys Compd. 685 (2016) 905–912. doi:10.1016/j.jallcom.2016.06.122.

[77] P. Li, J. Ye, Y. Liu, D. Yang, H. Yu, Study on the formation of core–rim structure in Ti(CN)-based cermets, Int. J. Refract. Met. Hard Mater. 35 (2012) 27–31. doi:10.1016/j.ijrmhm.2012.03.012.

[78] D.-S. Park, Y.-D. Lee, S. Kang, Effect of Carbides on the Microstructure and Properties of Ti(C,N)-Based Ceramics, J. Am. Ceram. Soc. 82 (2004) 3150–3154. doi:10.1111/j.1151-2916.1999.tb02216.x.

[79] P. Feng, W.. Xiong, L.. Yu, Metallurgy reaction foundation and microstructural characterization of TiCN-based cermets Part II: mechanism of formation of core-rim structure and gas evolution during sintering, Mater Rev. 18 (2004) 6–8.

[80] C. Zhang, H. Yin, R. Zhang, X. Jiang, G. Liu, Y. Du, Experimental and thermodynamic investigation of gradient zone formation for Ti(C,N)-based cermets sintered in nitrogen atmosphere, Ceram. Int. 43 (2017) 12089–12094. doi:10.1016/j.ceramint.2017.06.064.

[81] A. Rajabi, M.J. Ghazali, A.R. Daud, Chemical composition, microstructure and

sintering temperature modifications on mechanical properties of TiC-based cermet – A review, Mater. Des. 67 (2015) 95–106. doi:10.1016/j.matdes.2014.10.081.

[82] Q. Xu, X. Ai, J. Zhao, F. Gong, X. Tian, H. Zhang, Application of different dispersants in fabricating Ti(C,N)-based cermet tool materials., Key Eng. Mater. 693 (2016) 353–540. doi:10.4028/www.scientific.net/KEM.693.535.

[83] G. Liu, J. Li, K. Chen, Combustion synthesis of refractory and hard materials: A review, Int. J. Refract. Met. Hard Mater. 39 (2013) 90–102. doi:10.1016/j.ijrmhm.2012.09.002.

[84] G. Liu, J. Li, K. Chen, One-step preparation of dense TiC1−xNx–Ni3Ti cermet by combustion synthesis, Mater. Des. 87 (2015) 6–9. doi:10.1016/j.matdes.2015.07.179.

[85] E.A. Levashov, A.S. Mukasyan, A.S. Rogachev, D. V Shtansky, Self-propagating high-temperature synthesis of advanced materials and coatings, Int. Mater. Rev. 62 (2017) 203–239. doi:10.1080/09506608.2016.1243291.

[86] K. Das, T.K. Bandyopadhyay, S. Das, A review on the various synthesis routes of TiC reinforced ferrous based composites, J. Mater. Sci. 37 (2002) 3881–3892. doi:10.1023/A:1019699205003.

[87] J. Xiong, Z. Guo, M. Yang, B. Shen, Preparation of ultra-fine TiC0.7N0.3-based cermet, Int. J. Refract. Met. Hard Mater. 26 (2008) 212–219. doi:10.1016/j.ijrmhm.2007.05.001.

[88] A. Levy, A. Miriyev, A. Elliott, S.S. Babu, N. Frage, Additive manufacturing of complex-shaped graded TiC/steel composites, Mater. Des. 118 (2017) 198–203. doi:10.1016/j.matdes.2017.01.024.

[89] Z. Guo, J. Xiong, M. Yang, S. Xiong, J. Chen, Y. Wu, H. Fan, L. Sun, J. Wang, H. Wang, Dispersion of nano-TiN powder in aqueous media, J. Alloys Compd. 493 (2010) 362–367. doi:10.1016/j.jallcom.2009.12.103.

[90] R.G. Neves, B. Ferrari, A.J. Sanchez-herencia, C. Pagnoux, E. Gordo, Role of stabilisers in the design of Ti aqueous suspensions for pressure slip casting, Powder Technol. 263 (2014) 81–88. doi:10.1016/j.powtec.2014.04.093.

[91] N. Hernández, R. Moreno, A.J. Sánchez-Herencia, J.L.G. Fierro, Surface behavior of nickel powders in aqueous suspensions, J. Phys. Chem. B. 109 (2005).

doi:10.1021/jp0448954.

[92] S. Cabanas-Polo, R. Bermejo, B. Ferrari, A.J. Sanchez-Herencia, Ni–NiO composites obtained by controlled oxidation of green compacts, Corros. Sci. 55 (2012) 172–179. doi:10.1016/j.corsci.2011.10.016.

[93] N. Hernández, A.J. Sánchez-Herencia, R. Moreno, Forming of nickel compacts by a colloidal filtration route, Acta Mater. 53 (2005) 919–925. doi:10.1016/j.actamat.2004.10.038.

[94] R.J. Hunter, Foundations of Colloid Science, Clarendon Press, Oxford, 1987. doi:10.1080/01932698808944001.

[95] B.V. Derjaguin, L. Landau, Theory of the stability of strongly charged lyophobic sols and of the adhesion of strongly charged particles in solutions of electrolytes, Acta Physicochem. 14 (1941) 633–652.

[96] E.J.W. Verwey, Theory of the Stability of Lyophobic Colloids., J. Phys. Colloid Chem. 51 (1947) 631–636. doi:10.1021/j150453a001.

[97] R. Moreno, Colloidal processing of ceramics and composites, Adv. Appl. Ceram. 111 (2012) 246–253. doi:10.1179/1743676111Y.0000000075.

[98] R.J. Flatt, P. Bowen, Yodel: A Yield Stress Model for Suspensions, J. Am. Ceram. Soc. 89 (2006) 1244–1256. doi:10.1111/j.1551-2916.2005.00888.x.

[99] P. Sarkar, P.S. Nicholson, Electrophoretic Deposition (EPD): Mechanisms, Kinetics, and Application to Ceramics, J. Am. Ceram. Soc. 79 (1996) 1987–2002. doi:10.1111/j.1151-2916.1996.tb08929.x.

[100] L. Bergstrom, C.H. Schilling, I.A. Aksay, Consolidation Behavior of Flocculated Alumina Suspensions, J. Am. Ceram. Soc. 75 (1992) 3305–3314. doi:10.1111/j.1151-2916.1992.tb04426.x.

[101] J.A. Lewis, Colloidal Processing of Ceramics, J. Am. Ceram. Soc. 83 (2004) 2341–2359. doi:10.1111/j.1151-2916.2000.tb01560.x.

[102] R. Moreno Botella, Reología de suspensiones cerámicas, Madrid, 2005.

[103] F.M. Tiller, C.. Tsai, Theory of Filtration of Ceramics: I, Slip Casting, J. Am. Ceram. Soc. 69 (1986) 882–887. doi:10.1111/j.1151-2916.1986.tb07388.x.

[104] P. Alvaredo, S.A. Tsipas, E. Gordo, Influence of carbon content on the sinterability of an FeCr matrix cermet reinforced with TiCN, Int. J. Refract. Met. Hard Mater. 36 (2013) 283–288. doi:10.1016/j.ijrmhm.2012.10.007.

[105] J. Xiong, Z. Guo, B. Shen, D. Cao, The effect of WC, Mo2C, TaC content on the microstructure and properties of ultra-fine TiC0.7N0.3 cermet, Mater. Des. 28 (2007) 1689–1694. doi:10.1016/j.matdes.2006.03.005.

[106] P. Alvaredo, M. Dios, B. Ferrari, E. Gordo, Interface study for the design of alternative matrixes in cermets, in: EURO PM2015. Proceeding EURO PM2015, 2015.

[107] R.G. Neves, B. Ferrari, A.J. Sanchez-Herencia, E. Gordo, Colloidal approach for the design of Ti powders sinterable at low temperature, 2013. doi:10.1016/j.matlet.2013.05.015.

[108] R.G. Neves, E. Gordo, Procesamiento de polvos de Ti mediante asociación de técnicas coloidales y pulvimetalúrgicas, 2014.

[109] Z. Gonzalez, M.J. Perez, L.E. Lecue, L. San Miguel, B. Ferrari, Y. Castro, A.J. Sánchez-Herencia, C. Mendoza, ES 2 546 891 B2. Procedimiento de preparación de películas cerámicas sinterizadas fotoactivas, película obtenida y sus usos, 2016.

[110] R.G. Chaudhuri, S. Paria, Core/Shell Nanoparticles: Classes, Properties, Synthesis Mechanisms, Characterization, and Applications, Chem. Rev. 112 (4) (2012) 2373–2433. doi:10.1021/cr100449n.

[111] Y.J. Chen, M.S. Cao, Q. Tian, T.H. Wang, J. Zhu, A novel preparation and surface decorated approach for α-Fe nanoparticles by chemical vapor–liquid reaction at low temperature, Mater. Lett. 58 (2004) 1481–1484. doi:10.1016/j.matlet.2003.10.036.

[112] J.D. Ferguson, K.J. Buechler, A.W. Weimer, S.M. George, SnO2 atomic layer deposition on ZrO2 and Al nanoparticles: Pathway to enhanced thermite materials, Powder Technol. 156 (2005) 154–163. doi:10.1016/j.powtec.2005.04.009.

[113] J.. Ferguson, A.. Weimer, S.. George, Atomic layer deposition of ultrathin and conformal Al2O3 films on BN particles, Thin Solid Films. 371 (2000) 95–104. doi:10.1016/S0040-6090(00)00973-1.

[114] S. Liu, W. Tao, J. Li, Z. Yang, F. Liu, Study on the formation process of Al2O3–TiO2 composite powders, Powder Technol. 155 (2005) 187–192.

doi:10.1016/j.powtec.2005.05.048.

[115] A.-L. Morel, S.I. Nikitenko, K. Gionnet, A. Wattiaux, J. Lai-Kee-Him, C. Labrugere, B. Chevalier, G. Deleris, C. Petibois, A. Brisson, M. Simonoff, Sonochemical Approach to the Synthesis of Fe3O4-SiO2 Core−Shell Nanoparticles with Tunable Properties, ACS Nano. 2 (2008) 847–856. doi:10.1021/nn800091q.

[116] C.-C. Yang, S.-Y. Chen, S.-Y. Cheng, Synthesis and physical characteristics of ZnAl2O4 nanocrystalline and ZnAl2O4/Eu core-shell structure via hydrothermal route, Powder Technol. 148 (2004) 3–6. doi:10.1016/j.powtec.2004.09.011.

[117] Z. Jiang, C. Liu, Seed-Mediated Growth Technique for the Preparation of a Silver Nanoshell on a Silica Sphere, J. Phys. Chem. B. 107 (2003) 12411–12415. doi:10.1021/jp035060g.

[118] C.-H. Kim, K.-J. Park, Y.-J. Yoon, D.-S. Sinn, Y.-T. Kim, K.-H. Hur, Effects of milling condition on the formation of core–shell structure in BaTiO3 grains, J. Eur. Ceram. Soc. 28 (2008) 2589–2596. doi:10.1016/j.jeurceramsoc.2008.03.030.

[119] Y. Kobayashi, Y. Tadaki, D. Nagao, M. Konno, Deposition of Gold Nanoparticles on Polystyrene Spheres by Electroless Metal Plating Technique, J. Phys. 61 (2007) 582–586. doi:10.1088/1742-6596/61/1/117.

[120] Y. Kobayashi, Y. Tadaki, D. Nagao, M. Konno, Deposition of gold nanoparticles on silica spheres by electroless metal plating technique, J. Colloid Interface Sci. 283 (2005) 601–604. doi:10.1016/j.jcis.2004.09.002.

[121] Y. Boontongkong, R.E. Cohen, M.F. Rubner, Selective Electroless Copper Deposition within Block Copolymer Microdomains, Chem. Mater. 12 (2000) 1628–1633. doi:10.1021/cm990804h.

[122] J. Li, M. Moskovits, T.L. Haslett, Nanoscale Electroless Metal Deposition in Aligned Carbon Nanotubes, Chem. Mater. 10 (1998) 1963–1967. doi:10.1021/cm980122e.

[123] H. Zhao, Q. Liang, Y. Lu, Microstructure and Properties of Copper Plating on Citric Acid Modified Cotton Fabric, Fibers Polym. 16 (2015) 593–598. doi:10.1007/s12221-015-0593-9.

[124] J. Amer, S. Al-Khawaja, Nickel coated on beech wood by electroless nickel coating: effects of complexing agent concentrations on nickel film properties, Compos.

Interfaces. 21 (2014) 659–669. doi:10.1080/15685543.2014.914390.

[125] Q. Zhang, M. Wu, W. Zhao, Electroless nickel plating on hollow glass microspheres, Surf. Coatings Technol. (2004). doi:10.1016/j.surfcoat.2004.06.013.

[126] S. Fujii, H. Hamasaki, H. Takeoka, T. Tsuruoka, K. Akamatsu, Y. Nakamura, Electroless nickel plating on polymer particles, J. Colloid Interface Sci. 430 (2014) 47–55. doi:10.1016/j.jcis.2014.05.041.

[127] W. Wang, S. Ji, I. Lee, A facile method of nickel electroless deposition on various neutral hydrophobic polymer surfaces, Appl. Surf. Sci. 283 (2013) 309–320. doi:10.1016/j.apsusc.2013.06.108.

[128] M. Kimura, H. Yamagiwa, D. Asakawa, M. Noguchi, T. Kurashina, T. Fukawa, H. Shirai, Site-Selective Electroless Nickel Plating on Patterned Thin Films of Macromolecular Metal Complexes, Appl. Mater. Interfaces. 2 (2010) 3714–3717. doi:10.1021/am100853t.

[129] T.-Y. Chan, S.-T. Lin, Enhanced Sintering of an Fe-Ni-P Coated Composite Powder Prepared by Electroless Nickel Plating, JMEPEG. 6 (1997) 628–632. doi:10.1007/s11665-997-0056-6.

[130] C.A. Loto, Electroless Nickel Plating of Iron Powders, J. Met. 39 (1987) 36–38. doi:10.1007/BF03258607.

[131] K.Y. Lin, T.J. Yang, W.T. Tsai, Synthesis of Invar alloy powders by electroless plating, Mater. Sci. Eng. A. (2006) 226–231. doi:10.1016/j.msea.2005.10.028.

[132] M. Amirjan, K. Zangeneh-Madar, N. Parvin, Preparation of tungsten base composite powder by electroless nickel plating, Powder Metall. 53 (2010). doi:10.1179/003258908X347650.

[133] A. Ahmadi Ashtiani, S. Faraji, S. Amjad Iranagh, A. Hossein Faraji, The study of electroless Ni-P alloys with different complexing agents on Ck45 Steel substrate, Arab. J. Chem. (2013). doi:10.1016/j.arabjc.2013.05.015.

[134] R.L. Deuis, C. Subramanian, J.M. Yellup, K.N. Strafford, P. Arora, Study of electroless nickel plating of ceramic particles, Scr. Metall. Mater. (1995). doi:10.1016/0956-716X(95)00353-W.

[135] M. Uysal, R. Karslio, A. Alp, H. Akbulut, The preparation of core–shell Al2O3/Ni composite powders by electroless plating, Ceram. Int. 39 (2013) 5485–5493. doi:10.1016/j.ceramint.2012.12.060.

[136] C.A. Leon, R.A.L. Drew, Preparation of nickel-coated powders as precursors to reinforce MMCs, J. Mater. Sci. 35 (2000) 4763–4768.

[137] B.S. Necula, I. Apachitei, L.E. Fratila-Apachitei, C. Teodosiu, J. Duszczyk, Stability of nano-/microsized particles in deionized water and electroless nickel solutions, J. Colloid Interface Sci. (2007) 514–522. doi:10.1016/j.jcis.2007.05.073.

[138] G. Wen, Z.X. Guo, C.K.L. Davies, Microstructural characterization of electroless-nickel coatings on Zirconia powder, Scr. Mater. 43 (2000) 307–311. doi:10.1016/S1359-6462(00)00409-7.

[139] Y. Chen, M. Cao, Q. Xu, J. Zhu, Electroless nickel plating on silicon carbide nanoparticles, Surf. Coatings Technol. 172 (2003) 90–94. doi:10.1016/S0257-8972(03)00320-7.

[140] H. Ming, Z. Yunlong, G. Jing, S. Lin, T. Lili, The effect of electroless plating time on the coating performance of SiC powders, Adv. Mater. Res. 971–973 (2014) 204–207. doi:10.4028/www.scientific.net/AMR.971-973.204.

[141] M. Uysal, R. Karsliolu, A. Alp, H. Akbulut, Nanostructured core-shell Ni deposition on SiC particles by alkaline electroless coating, Appl. Surf. Sci. (2011). doi:10.1016/j.apsusc.2011.07.057.

[142] G.Z. Zou, M.S. Cao, L. Zhang, J. Gang Li, H. Xu, Y.J. Chen, A nanoscale core-shell of beta-SiCp-Ni prepared by electroless plating at lower temperature, Surf. Coatings Technol. (2006) 108–112. doi:10.1016/j.surfcoat.2005.11.026.

[143] G. Zou, M. Cao, H. Lin, H. Jin, Y. Kang, Y. Chen, Nickel layer deposition on SiC nanoparticles by simple electroless plating and its dielectric behaviors, Powder Technol. (2006). doi:10.1016/j.powtec.2006.07.002.

[144] X. Hui, K. Yu-Qing, Z. Lu, J. Hai-Bo, W. Bo, W. Bao-Li, Y. Jie, C. Mao-Sheng, Deposition Behavior and Mechanism of Ni Nanoparticles on Surface of SiC Particles in Solution Systems, CHIN. PHYS. LETT. 27 (2010). doi:10.1088/0256-307X/27/5/058103.

[145] Y.Q. Kang, M.S. Cao, X.L. Shi, Z.L. Hou, The enhanced dielectric from basalt fibers/nickel core-shell structures synthesized by electroless plating, Surf. Coatings Technol. 201 (2007) 7201–7206. doi:10.1016/j.surfcoat.2007.01.037.

[146] F.Z. Kong, X.B. Zhang, W.Q. Xiong, F. Liu, W.Z. Huang, Y.L. Sun, J.P. Tu, X.W. Chen, Continuous Ni-layer on multiwall carbon nanotubes by an electroless plating method, Surf. Coatings Technol. 155 (2002) 33–36. doi:10.1016/S0257-8972(02)00032-4.

[147] L.-M. Ang, T.S.A. Hor, G.-Q. Xu, C.-H. Tung, S. Zhao, J.L.S. Wang, Electroless Plating of Metals onto Carbon Nanotubes Activated by a Single-Step Activation Method, Chem. Mater. 11 (1999) 2115–2118. doi:10.1021/cm990078i.

[148] M. Palaniappa, G. Veera Babu, K. Balasubramanian, Electroless nickel–phosphorus plating on graphite powder, Mater. Sci. Eng. A. (2007) 165–168. doi:10.1016/j.msea.2007.03.004.

[149] J.N. Balaraju, V. Ezhil Selvi, K.S. Rajam, Electrochemical behavior of low phosphorus electroless Ni–P–Si3N4 composite coatings, Mater. Chem. Phys. 120 (2010) 546–551. doi:10.1016/j.matchemphys.2009.11.047.

[150] R.C. Agarwala, V. Agarwala, Electroless alloy/composite coatings: A review, Sadhana. 28 (2003) 475–493. doi:10.1007/BF02706445.

[151] S. Cabanas-Polo, Z. Gonzalez, A.J. Sanchez-Herencia, B. Ferrari, Influence of ultrasound on the instantaneous synthesis of tridimensional alpha-Ni(OH)2 nanostructures and derived NiO nanoparticles, CrystEngComm. 17 (2015) 6193–6206. doi:10.1039/C5CE00876J.

[152] S. Cabanas-Polo, K.S. Suslick, A.J. Sanchez-Herencia, Effect of reaction conditions on size and morphology of ultrasonically prepared Ni(OH)2 powders, Ultrason. Sonochem. 18 (2011) 901–906. doi:10.1016/j.ultsonch.2010.11.017.

[153] S. Cabañas-Polo, Síntesis asistida por ultrasonidos de nanoestructuras de compuestos de níquel, Universidad Autónoma de Madrid, 2012.

[154] Q. Song, Z. Tang, H. Guo, S.L.. Chan, Structural characteristics of nickel hydroxide synthesized by a chemical precipitation route under different pH values, J. Power Sources. 112 (2002) 428–434. doi:10.1016/S0378-7753(02)00396-8.

[155] M. Meyer, A. Bée, D. Talbot, V. Cabuil, J.M. Boyer, B. Répetti, R. Garrigos, Synthesis and dispersion of Ni(OH)2 platelet-like nanoparticles in water, J. Colloid Interface Sci. 277 (2004) 309–315. doi:10.1016/j.jcis.2004.04.034.

[156] Z.-H. Liang, Y.-J. Zhu, X.-L. Hu, β-Nickel Hydroxide Nanosheets and Their Thermal Decomposition to Nickel Oxide Nanosheets, J. Phys. Chem. B. 108 (2004) 3488–3491. doi:10.1021/jp037513n.

[157] E. Zhang, Y. Tang, Y. Zhang, C. Guo, L. Yang, Hydrothermal synthesis of β-nickel hydroxide nanocrystalline thin film and growth of oriented carbon nanofibers, Mater. Res. Bull. 44 (2009) 1765–1770. doi:10.1016/j.materresbull.2009.03.005.

[158] P. Jeevanandam, Y. Koltypin, A. Gedanken, Synthesis of Nanosized α-Nickel Hydroxide by a Sonochemical Method, Nano Lett. 1 (2001) 263–266. doi:10.1021/nl010003p.

[159] M. Vidotti, C. van Greco, E.A. Ponzio, S.I. Córdoba de Torresi, Sonochemically synthesized Ni(OH)2 and Co(OH)2 nanoparticles and their application in electrochromic electrodes, Electrochem. Commun. 8 (2006) 554–560. doi:10.1016/j.elecom.2006.01.024.

[160] A. Askarinejad, A. Morsali, Synthesis of cadmium(II) hydroxide, cadmium(II) carbonate and cadmium(II) oxide nanoparticles; investigation of intermediate products, Chem. Eng. J. 150 (2009) 569–571. doi:10.1016/j.cej.2009.03.005.

[161] M.A. Alavi, A. Morsali, Syntheses and characterization of Sr(OH)2 and SrCO3 nanostructures by ultrasonic method, Ultrason. Sonochem. 17 (2010) 132–138. doi:10.1016/j.ultsonch.2009.05.004.

[162] M.A. Alavi, A. Morsali, Syntheses and characterization of Mg(OH)2 and MgO nanostructures by ultrasonic method, Ultrason. Sonochem. 17 (2010) 441–446. doi:10.1016/j.ultsonch.2009.08.013.

[163] S.-H. Wu, D.-H. Chen, Synthesis and characterization of nickel nanoparticles by hydrazine reduction in ethylene glycol, J. Colloid Interface Sci. 259 (2003) 282–286. doi:10.1016/S0021-9797(02)00135-2.

[164] K.H. Kim, Y.B. Lee, E.Y. Choi, H.C. Park, S.S. Park, Synthesis of nickel powders from various aqueous media through chemical reduction method, Mater. Chem. Phys. 86

(2004) 420–424. doi:10.1016/j.matchemphys.2004.04.011.

[165] K.H. Kim, Y.B. Lee, S.G. Lee, H. Park, S.S. Park, Preparation of fine nickel powders in aqueous solution under wet chemical process, Mater. Sci. Eng. A. 381 (2004) 337–342. doi:10.1016/j.msea.2004.04.031.

[166] R.-Y. Chen, K.-G. Zhou, Preparation of ultrafine nickel powder by wet chemical process, Trans. Nonferrous Met. SOC. China. 16 (2006) 1223–1227. doi:doi:10.1016/S1003-6326(06)60405-6.

[167] J.W. Park, E.H. Chae, S.H. Kim, J.H. Lee, J.W. Kim, S.M. Yoon, J.-Y. Choi, Preparation of fine Ni powders from nickel hydrazine complex, Mater. Chem. Phys. 97 (2006) 371–378. doi:10.1016/j.matchemphys.2005.08.028.

[168] G.G. Couto, J.J. Klein, W.H. Schreiner, D.H. Mosca, A.J. de Oliveira, A.J. Zarbin, Nickel nanoparticles obtained by a modified polyol process: Synthesis, characterization, and magnetic properties, J. Colloid Interface Sci. 311 (2007) 461–468. doi:10.1016/j.jcis.2007.03.045.

[169] D.-P. Wang, D.-B. Sun, H.-Y. Yu, H.-M. Meng, Morphology controllable synthesis of nickel nanopowders by chemical reduction process, J. Cryst. Growth. 310 (2008) 1195–1201. doi:10.1016/j.jcrysgro.2007.12.052.

[170] Z.G. Wu, M. Munoz, O. Montero, The synthesis of nickel nanoparticles by hydrazine reduction, Adv. Powder Technol. 21 (n.d.) 165–168. doi:10.1016/j.apt.2009.10.012.

[171] J. Tientong, S. Garcia, C.R. Thurber, T.D. Golden, Synthesis of Nickel and Nickel Hydroxide Nanopowders by Simplified Chemical Reduction, J. Nanotechnol. (2014). doi:10.1155/2014/193162.

[172] J.-O. Andersson, T. Helander, L. Höglund, P. Shi, B. Sundman, Thermo-Calc and DICTRA, computational tools for materials science, Calphad. 26 (2002) 273–312. doi:10.1016/S0364-5916(02)00037-8.

[173] I. Gonzalo_Juan, B. Ferrari, M.T. Colomer, A.J. Sánchez-Herencia, Colloidal processing and sintering of porous percolative Ni-YSZ layers, J. Memb. Sci. 352 (2010) 55–62. doi:10.1016/J.MEMSCI.2010.01.060.

[174] S. Wawrzik, P. Zhou, C. Buchegger, W. Lengauer, Metallurgy and thermochemistry of cermet/hardmetal laminates, Int. J. Refract. Met. Hard Mater. 50 (2015) 282–289.

doi:10.1016/J.IJRMHM.2015.02.007.

[175] V.. Tracey, Nickel in hardmetals, Int. J. Refract. Met. Hard Mater. 11 (1992) 137–149. doi:10.1016/0263-4368(92)90056-8.

[176] M. Chen, Q. Zhuang, N. Lin, Y. He, Improvement in microstructure and mechanical properties of Ti(C,N)-Fe cermets with the carbon additions, J. Alloys Compd. 701 (2017) 408–415. doi:10.1016/j.jallcom.2017.01.119.

[177] A. Jam, L. Nikzad, M. Razavi, TiC-based cermet prepared by high-energy ball-milling and reactive spark plasma sintering, Ceram. Int. 43 (2017) 2448–2455. doi:10.1016/j.ceramint.2016.11.039.

[178] R. Bermejo, R. Danzer, 2.09 – Mechanical Characterization of Ceramics: Designing with Brittle Materials, in: Compr. Hard Mater., 2014: pp. 285–298. doi:10.1016/B978-0-08-096527-7.00028-3.

[179] A. Börger, P. Supancic, R. Danzer, The ball on three balls test for strength testing of brittle discs: Part II: analysis of possible errors in the strength determination, J. Eur. Ceram. Soc. 24 (2004) 2917–2928. doi:10.1016/j.jeurceramsoc.2003.10.035.

[180] A. Börger, P. Supancic, R. Danzer, The ball on three balls test for strength testing of brittle discs: stress distribution in the disc, J. Eur. Ceram. Soc. 22 (2002) 1425–1436. doi:10.1016/S0955-2219(01)00458-7.

[181] R. Danzer, W. Harrer, P. Supancic, T. Lube, Z. Wang, A. Börger, The ball on three balls test—Strength and failure analysis of different materials, J. Eur. Ceram. Soc. 27 (2007) 1481–1485. doi:10.1016/j.jeurceramsoc.2006.05.034.

[182] ISO/DIS 23146 Fine ceramics (advanced ceramics, advanced technical ceramics) – test methods for fracture toughness of monolithic ceramics – single-edge V-notch beam (SEVNB) method. 2007, (n.d.).

[183] H.G. Tattersall, G. Tappin, The work of fracture and its measurement in metals, ceramics and other materials, J. Mater. Sci. 1 (1966) 296–301. doi:10.1007/BF00550177.

[184] J. Gurland, New scientific approaches to development of tool materials, Int. Mater. Rev. 33 (1988) 151–166. doi:10.1179/095066088790324111.

[185] S. Zhou, W. Zhao, W. Xiong, H. Zhongguo, Thermodynamics of the formation of contiguity between ceramic grains and interface structures of Ti(C,N)-based cermets, Int. J. Refract. Met. Hard Mater. 27 (2009) 740–746. doi:10.1016/J.IJRMHM.2008.12.005.

[186] H.C. Lee, J. Gurland, Hardness and deformation of cemented tungsten carbide, Mater. Sci. Eng. 33 (1978) 125–133. doi:10.1016/0025-5416(78)90163-5.

[187] H.E. Exner, Physical and chemical nature of cemented carbides, Int. Met. Rev. 24 (1979) 149–173. doi:10.1179/imtr.1979.24.1.149.

[188] B. Roebuck, E.A. Almond, Deformation and fracture processes and the physical metallurgy of WC–Co hardmetals, Int. Mater. Rev. 33 (1988) 90–112. doi:10.1179/imr.1988.33.1.90.

[189] E. Chicardi, Y. Torres, J.M. Córdoba, M.J. Sayagués, J. a. Rodríguez, F.J. Gotor, Effect of sintering time on the microstructure and mechanical properties of (Ti,Ta)(C,N)-based cermets, Int. J. Refract. Met. Hard Mater. 38 (2013) 73–80. doi:10.1016/j.ijrmhm.2013.01.001.

[190] J.J. Roa, E. Jimenez-Pique, C. Verge, J.M. Tarragó, A. Mateo, J. Fair, L. Llanes, Intrinsic hardness of constitutive phases in WC–Co composites: Nanoindentation testing, statistical analysis, WC crystal orientation effects and flow stress for the constrained metallic binder, J. Eur. Ceram. Soc. 35 (2015) 3419–3425. doi:10.1016/J.Jeurceramsoc.2015.04.021.

[191] Y. Cao, Z. Xue, X. Chen, D. Raabe, Correlation between the flow stress and the nominal indentation hardness of soft metals, Scr. Mater. 59 (2008) 518–521. doi:10.1016/J.SCRIPTAMAT.2008.04.039.

[192] L.Y. Wang, G.Q. Wu, D.G. Evans, Synthesis and characterization of a layered double hydroxide containing an intercalated nickel(II) citrate complex, Mater. Chem. Phys. 104 (2007) 133–140.

[193] S. Cabanas-Polo, B. Ferrari, E. Gordo, A.J. Sánchez-Herencia, C. Argirusis, Nanosized Nickel Powder Synthesized by a Reduction Method Assisted by Ultrasound, in: EURO PM 2012. Proceeding EURO PM 2012, Basel, 2012.

[194] M. Dios, Z. González, E. Gordo, B. Ferrari, Core-shell Ti(C,N)-Ni Structures

Fabricated by Chemical Precipitation of Ni-based Nanoparticles on Ti(C,N) Suspensions, EURO PM 2015. Proceeding EURO PM 2015. (n.d.).

[195] D. Zeng, Y. Chen, Z. Wang, J. Wang, Q. Xie, D.-L. Peng, Synthesis of Ni-Au-ZnO ternary magnetic hybrid nanocrystals with enhanced photocatalytic activity, Nanoscale. 7 (2015) 11371–11378. doi:10.1039/c5nr01124h.

[196] Y. Sahoo, Y. He, M.T. Swihart, S. Wang, H. Luo, E.P. Furlani, P.N. Prasad, An aerosol-mediated magnetic colloid: Study of nickel nanoparticles, J. Appl. Phys. 98 (2005) 54308. doi:10.1063/1.2033145.

[197] Y. He, X. Li, M.T. Swihart, Laser - Driven Aerosol Synthesis of Nickel Nanoparticles, Chem. Mater. 17 (2005) 1017–1026. doi:10.1021/cm048128t.

[198] K.-M. Nam, H.-J. Kim, D.-H. Kang, Y.-S. Kim, S.-W. Song, Ammonia-free coprecipitation synthesis of a Ni-Co-Mn hydroxide precursor for high-performance battery cathode materials, Green Chem. 17 (2015) 1127–1135. doi:10.1039/C4GC01898B.

[199] L. Escobar-Alarcón, E. Camps, S. Romero, S. Muhl, I. Camps, E. Haro-Poniatowski, TiCN thin films grown by reactive crossed beam pulsed laser deposition, Appl. Phys. A. 101 (2010) 771–775. doi:10.1007/s00339-010-5935-2.